High-Resolution Breast Diffusion Weighted Imaging with Improved Nyquist Ghost Correction and Simultaneous Multislice Imaging

A DISSERTATION
SUBMITTED TO THE FACULTY OF THE UNIVERSITY OF MINNESOTA
BY

Jessica Ann McKay

IN PARTIAL FULFILLMENT OF THE REQUIREMENTS FOR THE DEGREE OF DOCTOR OF PHILOSOPHY IN THE DEPARTMENT OF BIOMEDICAL ENGINEERING

Advised by Dr. Patrick J. Bolan

June 2020

Acknowledgments

I would like to sincerely thank my advisor, Dr. Patrick Bolan, for his continued direction and support over the past 6 years. Pat, I am so grateful for the experience I have had learning under you and am lucky to call you a mentor and friend. Thank you for your patience and encouragement, your infallible passion for science, the hours you have spent helping me to brainstorm and think out loud, and your many drumstick demonstrations of MR physics.

This work would not have been possible without the contributions of many researchers, including Sudhir Ramanna, Steen Moeller, Edward Auerbach, Greg Metzger, Ethan Leng, Nathan Rubin, Lei Zhang, Essa Yacoub, Christophe Lenglet, Lance DelaBarre, Jeramy Kulesa, and Kamil Ugurbil. Thank you to Drs. An Church, Tim Emory, Noelle Hoven, Jessica Kuehn-Hajder, and Michael Nelson for sharing your clinical expertise. I would also like to acknowledge the leadership and members of the I-SPY 2 team, especially Dr. Doug Yee at the University of Minnesota's and the Imaging Chair, Dr. Nola Hylton.

Financial support for this work was provided by the National Institute of Health (P41 EB027061, S10 OD017974-01, and R21 CA201834) and the National Institute of Heath's National Center for Advancing Translational Sciences award UL1 TR002494.

Thank you to everyone at the CMRR for the role you have played in my education, for inspiring me with your passion for MRI, and, especially, for your friendship. Thank you to the CMRR administrative team, MR technologists, technical support, and everyone who kept the espresso machine running. Special thanks to Dr. Steen Moeller for his encouragement, ideas, sharing of MATLAB code, and answers to my many "quick" questions. Thank you again to Sudhir Ramanna for your patience and guidance. Finally, I would like to thank my committee members, Dr. Mehmet Akçakaya, Dr. Patrick Bolan, Dr. Michael Garwood, and Dr. Gregory Metzger, for sharing their wealth of MRI knowledge and experience and for their guidance in the development of this thesis project.

Finally, thank you to my supportive friends and family! Thanks to my fiancé, Benj, for his unwavering support and reassurance. I especially thank my parents, Neil and Julie, who have continuously encouraged and supported me over the past 28 years. Thank you for your advice, emotional support, and for making education such a priority in our family. Thank you, Mom, for cultivating my creativity and imagination with countless trips to the library and craft supplies coming out of our ears. Thank you, Dad, for telling me I was good at math and science in elementary school and assuring me so many times since then that I've actually come to believe it myself. How blessed I am to have parents like you.

Table of Contents

List of Tables

List of Figures

Preface

Diffusion-weighted imaging (DWI) is a quantitative MRI method that measures the apparent diffusion coefficient (ADC) of water molecules, which reflects cell density and serves as an indication of malignancy. Unfortunately, however, the clinical value of DWI is severely limited by the undesirable features in images that common clinical methods produce, including large geometric distortions, ghosting and chemical shift artifacts, and insufficient spatial resolution. These problematic artifacts and low resolution have hindered the translation of body DWI to the clinic. Thus, in order to exploit information encoded in diffusion characteristics and fully assess the clinical value of ADC measurements, it is first imperative to achieve technical advancements of DWI.

The purpose of this work is to improve DWI methods for breast imaging at 3 Tesla to robustly provide diffusion-weighted images and ADC maps with anatomical quality and resolution.

Chapters 1 and 2 lay out background information to provide clinical motivation for this work and explain the current standard in breast DWI, as well as some alternatives proposed throughout the literature. The main work of this project has two major parts: Nyquist ghost correction and the use of simultaneous multislice imaging (SMS) to achieve high resolution. Thus, the remainder of the thesis is centered around two corresponding journal articles.

Chapters 3 and 4 focus on Nyquist ghost correction. Chapter 3 explains much of the exploratory work done to characterize the Nyquist ghost in breast DWI. This work led to the development of a novel referenceless ghost correction method, presented in Section 4.1, called Ghost/Object minimization. Section 4.2 then presents a rigorous comparison of Nyquist ghost correction methods, including Ghost/Object minimization, in a standard breast DWI acquisition, which was presented as a paper entitled *Nyquist Ghost Correction of Breast Diffusion Weighted Imaging using Referenceless Methods*. Together, this work suggested the need for referenceless Nyquist ghost correction in further work. Thus, these methods were applied to advanced SMS imaging and assessed an ISMRM abstract, presented in Section 4.3.

This work culminates in Chapter 5, which describes the advanced high-resolution SMS method that employs improved Nyquist ghost correction. Using a reader study, these methods were compared to a popular alternative, RS-EPI, which is provided here and was presented in the paper *A comparison of methods for high spatial resolution diffusion-weighted imaging in breast MRI*. Chapter 6 suggests several promising future directions, including some preliminary work explored throughout this project. Finally, Chapter 7 comments on future clinical translation and further technical developments.

Chapter 1: Breast Cancer and the Role of MRI

In the United States, breast cancer is the 2nd most common cancer for females after skin cancers and affects about 13% of women over the course of their lifetimes. The American Cancer Society predicts that in 2020 about 276,000 women will be diagnosed with invasive breast cancer, which will lead to over 42,000 deaths (1). While the incidence of breast cancer has increased steadily by about 0.3% each year, since 2013 the mortality rates have been decreasing by 1.3% yearly (2). This improvement is likely caused, not only by advances in treatment, but also by increased public awareness and earlier detection thanks to evolving screening practices.

Magnetic resonance imaging (MRI) is commonly used for breast cancer care for screening, disease staging, and monitoring treatment response. Additionally, it is less frequently used for image guided biopsy and diagnosis of mammography occult lesions. A typical MRI protocol consists of a T_1-weighted image prior to and one or more after the intravenous introduction of a contrast agent and a T_2-weighted image. The gadolinium-based contrast agent shortens T_1 relaxation of the blood, which accumulates around the cancer due to angiogenesis and leaky blood vessels, two hallmarks of cancer. Thus, the cancer appears bright on a contrast-enhanced (CE) image.

1.1 Applications of MRI in Breast Cancer

1.1.1 Screening

Breast cancer screening is the systematic surveillance of disease in an asymptomatic patient; its goal is to detect and treat breast cancer before symptoms occur and before metastasis to other organs. Screening is typically preformed using mammography with two nearly perpendicular views of each breast. It is recommended that women of average risk get yearly mammographic screening beginning at age 40. After the inception of mammographic screening many studies have consistently confirmed that annual mammographic screening reduces the mortality rate by at least 30%.

However, mammography often fails to detect some cancers especially in women with dense breasts, young high-risk patients, and those that carry BRCA mutations (3,4). Alternatively, CE-MRI has been shown to have very high sensitivity for the detection of breast cancer. Several studies have measured a sensitivity between 75.2% and 100%, most of which are over 80%, and a specificity between 83% and 98.4% (3). Mammography has been reported with sensitivity of 63% for women with dense breasts to 87% for those with low density and 90-96% specificity (5). Thus, the American Cancer Society recommends annual MRI screening to all women with a lifetime risk of breast cancer of 20% or higher based on family history, genetic predisposition, history of radiation to the chest, and p53 and PTEN mutations (6,7).

Assessment	Management	Likelihood of Cancer
Category 0: Incomplete – Need Additional Imaging Evaluation	Recommend addition imaging: mammogram or targeted US	N/A
Category 1: Negative	Routine breast MRI screening if cumulative lifetime risk ≥ 20%	Essentially 0% likelihood of malignancy
Category 2: Benign	Routine breast MRI screening if cumulative lifetime risk ≥ 20%	Essentially 0% likelihood of malignancy
Category 3: Probably Benign	Short-interval (6-month) follow-up	≥ 0% but ≤ 2% likelihood of malignancy
Category 4: Suspicious	Tissue diagnosis	> 2% but < 95% likelihood of malignancy
Category 5: Highly Suggestive of Malignancy	Tissue diagnosis	≥ 95% likelihood of malignancy
Category 6: Known Biopsy-Proven Malignancy	Surgical excision when clinically appropriate	N/A

Table 1.1 – BI-RADS® Assessment Categories and Management Recommendations
Modified from Morris EA, Comstock CE, Lee CH, et al. ACR BI-RADS® Magnetic Resonance Imaging. In: ACR BI-RADS® Atlas, Breast Imaging Reporting and Data System. Reston, VA, American College of Radiology; 2013.

Historically, mammography reports were ambiguous and contained vague descriptions of the finding, which made communication between physicians very difficult. It was necessary to streamline a reporting system as screening became more widespread. In 1993 the American College of Radiology (ACR) released a lexicon called Breast Imaging Reporting and Data System (BI-RADS) for standardizing mammographic reporting (Table 1.1). The system included structured reports that were organized into categories like breast density and a final assessment of the patient's risk and need for biopsy. Since then, the system has been regularly updated and extended to include ultrasound and MRI findings (8).

1.1.2 Staging

After confirming biopsy-proven cancer, MRI can also be used prior to surgery to characterize the extent of disease, including multifocal disease, chest wall involvement, axillary lymph nodes, and the contralateral breast. The MR images can then be used to help guide treatment and for surgical planning.

1.1.3 Monitoring treatment response

Historically the standard of care for breast cancer included surgery followed by adjuvant systemic therapy and possibly radiation. Recently, however, neoadjuvant systemic therapy has become more common for aggressive cancers and has been shown to downgrade surgeries of both the breast and nodes. Neoadjuvant systemic therapy usually includes cytotoxic chemotherapy or hormonal therapy and is indicated for patients with a tumor $\geq$ 2 cm or with positive lymph nodes, and particularly for triple negative or HER-2 amplified cancers (9).

Additionally, neoadjuvant chemotherapy can be advantageous because it can provide the ability to monitor the treatment response. Throughout therapy, treatment response may inform the course of treatment. Prior to surgery, pathologic complete response (pCR), which refers to the absence of invasive and in situ disease in the breast and lymph nodes as determined by pathology, has been shown to predict overall survival and disease-free survival in some subtypes. For example, the I-SPY 2 TRIAL is one large

study that utilizes pCR as a metric to assess neoadjuvant treatments of aggressive cancers.

1.2 The I-SPY Initiative

The University of Minnesota's Masonic Cancer Center is one of many clinical sites that participates in a breast cancer clinical trial called Investigation of Serial studies to Predict Your Therapeutic Response with Imaging And moLecular analysis 2 (I-SPY 2 TRIAL). The I-SPY initiative was formed in 1998 led by breast surgeon Dr. Laura Esserman and Dr. Nola Hylton, who is an expert in breast MRI, from the University of California San Francisco. Drs. Esserman and Hylton formed a multicenter coalition to provide effective drugs to the right patient as early as possible (10). The group identified and addressed four major flaws in breast cancer research and treatment: 1) drug studies are often set in the metastatic setting when the disease is no longer curable; 2) localized and early-stage cancers were treated with adjuvant therapy, in other words after surgery; 3) most studies failed to include biomarkers beyond the common hormone receptor (HR) and human epidermal growth factor receptor (HER2); and 4) the use of randomized controlled trials, considered the gold standard, is inefficient because the structure does not account for the trial results throughout the study.

1.2.1 I-SPY 2 TRIAL

I-SPY 2, the second stage of the I-SPY initiative, was launched in 2010 to further address the shortcomings described above. I-SPY 2 included neoadjuvant systemic therapy in order to treat the cancer at its earliest stages. Pathologic complete response (pCR), which describes the full disappearance of the tumor, is then used as the clinical endpoint instead of previously used recurrence free survival (RFS) that takes 5 to 7 years to measure. This allows for faster updates to assess the effectiveness of drugs throughout the trial.

In I-SPY 2, cancers are thoroughly classified by hormone receptor status, as well as a 70-gene MammaPrint assay in order to include a diverse patient population and provide more information to predict outcomes to specific drugs. The trial examines up to

12 therapies simultaneously, which allows for the inclusion of nearly all breast cancer patients and accelerates the evaluation of many drugs.

The study was designed in an adaptive way that is informed by statistical analysis. Each patient receives four or more contrast enhanced MRI exams and several studies of tumor pathology during the course of their treatment. These serial MRI measurements, scores of residual cancer burden, and information about tumor subtype, are used to assess each drug for the specific subtype and can even indicate prompt adjustment in treatment for the individual patient. The weighted randomization of treatments for future participants is updated based on these ongoing results. Thus, drugs that are learned to be effective for specific subtypes will be increasingly assigned to patients within those subtypes. Moreover, drugs can be added, dropped, or graduated throughout the trial.

1.2.2 ACRIN 6698 – A sub-study

One additional advantage of I-SPY 2 is the flexibility of the study design, which accommodates sub-studies within the trial. The American College of Radiology Imaging Network (ACRIN) trial 6698 is one sub-study of I-SPY 2 that was conducted between 2012 and 2015. ACRIN 6698 is another multicenter trial that aimed to evaluate the ability of diffusion weighted MRI for monitoring treatment response. The University of Minnesota's Masonic Cancer Center is also a clinical site included in I-SPY 2 and ACRIN 6698. Thus, much of the data included in this project were acquired based on these protocol requirements and submitted to the trial.

In order to join ACRIN 6698, clinical sites were required to qualify their 1.5 or 3 T MR systems based on assessment of DWI studies on phantoms and patients following protocol guidelines set by the trial. The MR protocol included T_2-weighted, DWI, and axial T_1-weighted CE-MRI with at least 6 timepoints. The DWI protocol used the standard axial single shot SE-EPI with b-values of 0, 100, 600, and 800 s/mm^2. The scan was limited to 5 minutes and required to have in plane resolution of 1.7-2.8 mm and 4-5 mm slices.

The main hypothesis to test in ACRIN 6698 was that changes in ADC would be predictive of pCR in breast cancer patients undergoing neoadjuvant chemotherapy. The

study also sought to assess the predicted value of combined MRI-derived metrics, ADC values and the functional tumor volume measured on DCE images (11). To that end, the trial was designed to include CE-MRI and DWI at four timepoints throughout treatment. Each patient received an initial MR exam (T0) followed by 12 weekly cycles of Paclitaxel and a randomized experimental neoadjuvant chemotherapy agent. A second MR exam was conducted midway through (T1, 3 weeks) and after this therapy (T2). Finally, all the patients received four cycles of Anthracycline and a final MR exam (T3). Two recent reports evaluated these MR findings, namely the initial and change of ADC and functional tumor volume (FTV), at all four timepoints.

In one manuscript by Partridge et al. (12) the mean ADC generally increased throughout treatment. While ADC prior to treatment (T0) or early treatment (T1) was not predictive of pCR, increase in ADC value at T3 predicted pCR with AUC = 0.60 ($p = 0.17$), prior to adjustments for multiple comparisons. With adjustments, ΔADC predicted pCR in HR+/HER2- tumors at T2 and triple-negative tumors at T3. Although ΔADC did not reach significance for other subtypes at any time points, the predictive power of ADC increased when combined with tumor subtype (from AUC = 0.57 to AUC = 0.72, $p=0.302$). Interestingly, adding ΔFTV did not seem to improve the predictive value, suggesting that change of ADC may be comparable to that of CE-MRI-derived tumor volume and may be a good candidate for a contrast free alternative.

Li et al. (13) conducted a similar study on I-SPY 2 data, rather than ACRIN 6698. This DWI was acquired with 2 b-values, as opposed to 4, and was not subject to the strict quality control of ACRIN 6698. They found that the initial FTV predicts pCR (AUC = 0.63, $p < 0.0001$), as does the FTV change at all timepoints (AUC = 0.63 to 0.7, $p < 0.0001$). As a single predictor, the initial ADC did not predict pCR, but the change of ADC at the three following timepoints did with AUC increasing with each timepoint from 0.57 (T1, $p<0.03$) and 0.72 (T3) ($p < 0.0001$). Although variable across different subtypes, for the overall cohort, adding ADC to FTV increased the predictive value at T2 (from AUC = 0.76 to AUC = 0.78) and T3 (AUC = 0.76 to AUC = 0.81). ADC at T0 was valuable for one subgroup, HR+/HER2-, increasing the AUC from 0.52 with FTV only to 0.65 with both.

Both of the studies discussed above show promise for the value of DWI in predicting pCR, especially for certain cancer subtypes. However, the quality of the diffusion data was still limited as many advanced DWI methods are not available on clinical scanners. Thus, I-SPY 2 used the standard SE-EPI method, which has seen recent developments, including readout segmentation, multishot improvements, and simultaneous multislice imaging. DWI analysis methods also continue to evolve. Data were acquired across different vendors, field strengths, and sites. Despite strict quality control, image quality varied, especially in DWI which already suffers from poor resolution, low SNR, and geometric distortion. As methods continue to improve across clinical sites, these promising results are expected to further improve.

1.3 Controversy in Breast MRI

After the introduction of mammographic screening, researchers saw clear evidence of an improvement in the breast cancer mortality rate (14). Still, x-ray mammography often misses cancers, especially in patients with dense breasts, younger women, and women with high risk. Because CE-MRI is extremely sensitive to breast cancer, it seemed to be a good candidate for breast cancer clinical care, particularly in the cases where mammography is insufficient. However, the introduction of MR screening and preoperative staging has not led to a clear decrease in mortality as expected. Instead, breast MRI is associated with higher rates of false positives and negative biopsies in the screening setting. As a staging tool, MR images often contribute to decisions for more aggressive surgeries. Thus, the widespread use of MRI for breast cancer screening and preoperative staging remains a controversial subject that needs consensus in order to maintain the best screening practices for patients.

1.3.1 Practical considerations

According to an article by Dr. Cheryl Herman in the Ethics Journal of the American Medical Association, for a screening tool to be “good”, it must be affordable, safe, widely available, and demonstrate improved health outcomes by reliable detection of a high proportion of the disease (15). One major drawback of using MRI as a screening tool for breast cancer is its high cost and low availability. While the cost varies widely, it was

estimated in 2007 that a CE-MRI breast exam cost $1,000 to $2,000, about ten times that of mammography (16). Moreover, many insurance plans do not cover the cost of such advanced imaging. Additionally, due to the large size and cost of MRI scanners, MR exams are significantly less accessible than mammography, especially in rural areas and less developed countries. If the detected cancer requires an image-guided biopsy, MR-guided biopsies are difficult, expensive, and rarely done clinically.

CE-MRI has also been associated with increased false positives that can cause unnecessary stress on the patient as well as costly follow-up tests, including surgical or needle biopsies, alternative imaging with associated radiation dose, or second-opinion consultations (17). Finally, the essential screening sequence (CE-MRI) requires injection of a gadolinium-based contrast agent. The safety of gadolinium is still a very active area of research with contradicting evidence and opinions within the field. Gadolinium injections are contraindicated for patients with compromised kidney function and can additionally cause rare but life-threatening allergic reactions.

1.3.2 The concept of overdiagnosis

Overdiagnosis refers to the detection of disease that would not have clinical effect in the patient's lifetime if it went undiagnosed; overdiagnosis can lead to overtreatment and unnecessary psychological harm on a patient and their family. Breast MRI has been thought to cause overdiagnosis because, according to [Ref (18)], our ability to detect disease with MRI is unequal to our ability to predict its behavior.

The extensive use of breast MRI in screening and preoperative staging is controversial because while it is associated with increased detection and more invasive surgeries, there is still no evidence that overall outcomes have been improved. For example, many women receive preoperative MRI to identify additional foci occult on mammography, which occurs in about 16% of cases due to the high sensitivity of MRI, according to a meta-analysis by Houssami and Hayes (17). These preoperative exams are performed under the assumption that the MRI will find more foci, which may change the surgical plan to remove the previously undetected disease, reducing the re-excision rate and recurrence and/or metastasis, and thereby reduce mortality. While the common use of

preoperative MRI has been shown to often increase surgery from breast conservation to mastectomy, there is a lack of evidence that suggest these more aggressive surgeries improve the outcomes as expected (19). In other words, there has been no sign of a decrease in re-excision rates, positive margins, local recurrence, or mortality despite increased rates of mastectomy.

This lack of improved outcomes has many concerned that the use of MRI is leading to overdiagnosis of breast cancer and that many of these cancers that were undetected on mammography (especially secondary foci) are not actually clinically significant (especially for patient who are undergoing standard excision and breast radiation). These unnecessary radical surgeries can then have negative impacts on the patients and add financial burden to the healthcare system.

In terms of breast cancer screening, there is little data that thoroughly compares mammography and MRI. While studies have shown an increase in sensitivity and increased detection using MRI, to date there have been no studies that use a prospective randomized design for screening and measure survival as the endpoint. Most recently, Saadatmand and colleagues conducted the first randomized trial and showed that MR screening detected three times the incidence of invasive cancers than mammographic screening (24 vs 8), suggesting that many invasive cancers went undetected by mammogram (20). Time will tell if this increase in detection leads to an increase in survival.

As a scientist I must argue that more information is better. If we, as a society, write off breast MRI on the basis of “overdiagnosis”, we are throwing away a wealth of data that could inform both researchers and clinicians. This knowledge can provide details, not only on who has cancer, but also on the characteristics and behavior of said cancer. Therefore, we should replace the word “overdiagnosis” with “misinterpretation”, and rather than focusing our energy on measuring what MRI has failed to do in breast cancer, consider what it can do in the future.

The unrivaled sensitivity of MRI gives us the ability to detect every breast cancer that manifests, which then facilitates the opportunity to study every breast cancer with a

variety of tools. Moreover, with radiomics, deep learning, and the ever-broadening contrasts available with MRI (i.e. diffusion, elastography, etc.), not only can MRI detect these cancers, it can also be used as one of many tools to better characterize and understand them. Thus, rather than concede to overdiagnosis, the breast MRI field should aspire to understand these cancers and predict how/when they will grow and metastasize and how they will respond to various treatments. It is my hope that, with continuing advances, breast DWI will be one of many factors that contribute to this ability, positively affecting the detection, diagnosis, and treatment planning of all breast cancers, both those that are innocuous and those that may be fatal.

Active Surveillance

Overdiagnosis is also thought to persist in the context of mammographic screening, especially for non-invasive and low risk ductal carcinoma in situ (DCIS). Although it is estimated that only 20%-30% of DCIS will progress to invasive breast cancer, 97% of all DCIS is treated (21). This overtreatment is generally due to the lack of prognostic factors that accurately distinguish these harmless cancers from life-threatening disease (22). One suggested approach to decrease treatment of insignificant disease is active surveillance (AS). AS, sometimes called watchful waiting, refers to the intentional decision not to treat known disease while undergoing close monitoring, such that treatment will begin if tests indicate change.

While AS has been an active area of research in prostate cancer, it is less often discussed for breast cancer treatment. In current practice, nearly all breast cancers are treated, either with surgery, radiotherapy, and/or systemic therapy. To date, there are no completed trials that have carefully compared AS with treatment options. However, some ongoing studies have recently started to address this gap in evidence, including the Comparison of Operative versus Monitoring and Endocrine Therapy (COMET) trial (NCT02926911), the Low Risk DCIS (LORD) study (NCT02492607), and the Low Risk DCIS (LORIS) trial (UKCRN study ID 16736) (21,22). Though MRI does not play a major role in these trials, it may find an important role in AS in the future, especially with further technological advancements and increased use in clinical trials. Epidemiologically, the high sensitivity of MRI can detect a wide range of cancers to

provide a larger view of the disease for research purposes. Varying MRI contrasts and quantitative methods may provide reliable prognostic factors that distinguish fatal cancers, guiding the decision to use AS in lieu of traditional treatment. Finally, MRI may provide a detailed view of the tumor's appearance and characteristics to closely monitor change over the course of AS, potentially reducing the need for repetitive biopsies.

Chapter 2: Fundamentals of Diffusion Weighted Imaging

Diffusion MRI, or diffusion weighted imaging (DWI), is an MRI technique that can be used to measure the diffusion of water molecules within tissue. In DWI, magnetic gradients are applied with varying amplitudes and times along different directions to encode the diffusion along that same direction. Because diffusion in biological tissues is restricted by things like macromolecules, cell walls, and fibers, the diffusion contrast can give insight of the microscopic environment in the tissue. DWI has been applied in MRI in many different ways using models of varying complexity, including diffusion tensor imaging (DTI), diffusion kurtosis imaging (DKI), intravoxel incoherent motion (IVIM), etc.

2.1 The Basics of MRI

A basic MRI sequence requires three parts, including 1) signal excitation paired with slice selection, 2) an echo formation paired with an analog to digital converter (ADC), and 3) spatial encoding.

Very briefly, magnetic resonance imaging (MRI) uses a strong magnetic field combined with radiofrequency pulses and magnetic gradients to measure the dipole precession of the protons that typically belong to the Hydrogen of the water molecules in the human body. Because hydrogen molecules contain a single proton that is positively charged, when placed in a magnetic field the hydrogen molecules act like tiny dipoles that align with the main magnetic field, B_0. This equilibrium state can be perturbed by a radiofrequency (RF) pulse. Typically, this RF pulse is played along with a slice selection gradient (G_{slice}) in Z; this gradient modulates the frequency precession based on each spin's position in Z. The frequency of the RF pulse, along with G_{slice}, will determine the slice thickness and location.

2.1.1 Image formation

Echoes

Directly after the RF is applied the spins will be in phase but will immediately begin to dephase at a rate dependent on the tissue characteristics (called T_2 decay), the field inhomogeneity (called T_2' decay), or a combination of both (called T_2^* decay). Acquiring this signal is referred to as a free induction decay (FID). This FID is can be used in spectroscopy but is insufficient for the purposes of imaging. Thus, magnetic gradients and/or RF pulses are used to manipulate the spins, causing them to rephase and produce a secondary signal called an echo, which is measured for imaging. The type of echo formed will dictate the types of decay that are observed. The simplest imaging sequence employs a gradient echo, which can also be used for spatial encoding in the RO direction, shown in Figure 2.1.

Figure 2.1 – A Simple Gradient Echo Sequence
The pulse sequence diagram (a) and the k-space trajectory of a gradient echo sequence. After the 90º excitation, an FID occurs with T_2* relaxation. A prephase gradient (orange) is used to quickly dephase the signal, followed by a readout gradient (red) that forms an echo before the signal fully relaxes according to T_2*. This RO gradient achieves formation of a gradient echo at every position while also providing frequency encoding in x, traversing k-space according to the orange and red arrows (b). Importantly, the areas marked by * are equal. The PE gradient amplitude is modified with every TR to acquire a specified line in k_{PE} (blue gradient and arrow). Black dots indicate sampling through the RO, consistent with the ADC.

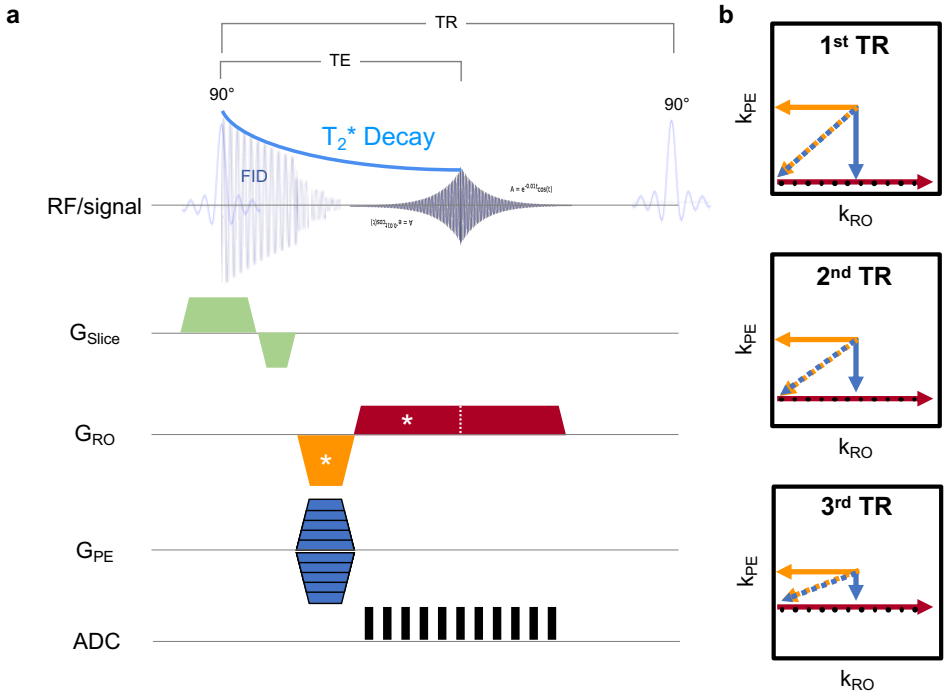

To form a gradient echo, a magnetic field gradient is played out on the frequency encoding axis. Prior to the readout, this gradient dephases the spins. An echo is formed as an equal and opposite gradient is played to rephase the spins, as shown in Figure 2.1a. In this case the signal decay caused by both the field inhomogeneity and the molecular interactions is not recovered and the signal is attenuated by T_2^* and dependent on the time that has passed, or the echo time (TE).

There are two other main types of echoes, which use RF pulses rather than magnetic gradients: Hahn spin echoes (SE) and stimulated echoes (STE) (Figure 2.2). For a spin echo, a secondary RF pulse is played along with a secondary slice select gradient to rotate the spins by 180º at time TE/2 so that they rephase at a time TE (see Figure 2.2a); in this case dephasing caused by field inhomogeneity is accounted for so that true T_2 decay is reflected in the signal. Finally, to form a stimulated echo, three excitation pulses are used consecutively with specific timing shown in Figure 2.2b. The time between the 2nd and 3rd excitations is called the mixing time (TM), during which the spins experience T_1 decay but no effect from T_2 decay.

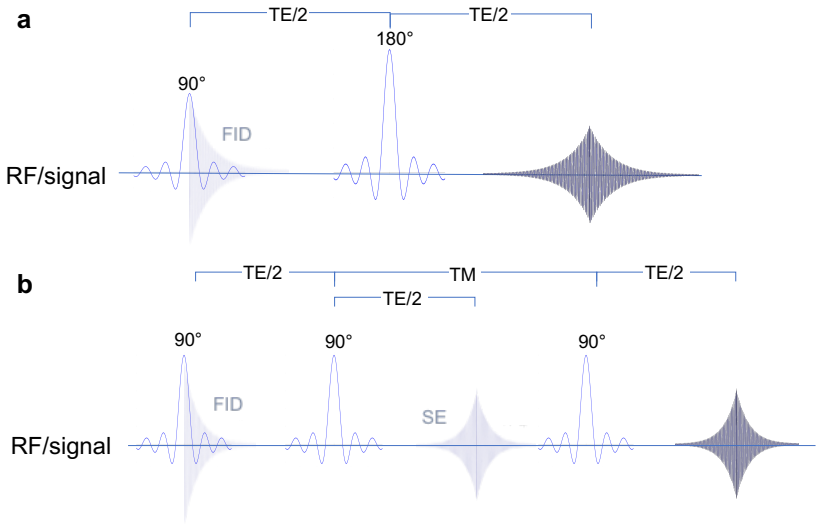

Figure 2.2 – Spin and Stimulated Echo Formation
a) Spin Echoes (SE) and b) Stimulated Echoes (STE) are two types of echoes that use RF pulses instead of gradients. Additional echoes are shown in faded blue. In SE, spins that experienced dephasing due to field inhomogeneity will be rephased by the 180º pulse, achieving T_2 decay. TM refers to the mixing time, during which the spins experience T_1 decay but not T_2 decay. Note that magnetic gradients (omitted in figure) are necessary for spatial encoding.

Spatial encoding and k-space

Spatial encoding is achieved by playing magnetic field gradients in two dimensions. The RO gradient is played in x during the echo formation and measurement of the signal, providing frequency encoding. The PE gradient is applied in y prior to the echo formation, providing phase encoding.

As phase encoding gradient (G_{PE}) is applied, the varying frequencies cause a phase difference between the neighboring spins, dependent on their position in y and the magnitude and duration of the gradient (t). When the PE gradient is turned off, this phase difference is maintained throughout the formation of the echo. For example, the modular blue gradient in Figure 2.1 causes a phase separation between neighboring spins in y prior to the echo formation. A large gradient will cause a larger phase separation, probing high resolution information and filling the edges of k-space where high spatial frequencies are stored. Thus, the gradient relates to k-space according to: $k_y = \frac{\gamma}{2\pi}\int_0^t G_{PE}(t)dt$, where γ is the gyromagnetic ratio.

Similarly, a prephase gradient is played in x to jump to the RO edge of k-space according to $k_x = \frac{\gamma}{2\pi}\int_0^t G_{RO}(t)dt$. During the echo formation, the RO gradient (G_{RO}) continues to play, such that the spins' frequencies are dependent on their position in x. This RO gradient supplies frequency encoding while simultaneously achieving a gradient echo at each position.

2.1.2 Echo-planar imaging

While the simple gradient echo sequence shown in Figure 2.1 contains all of the necessary parts to create an image, it is very inefficient, requiring an excitation for every line in k-space.

One widely used strategy is called echo-planar imaging (EPI), shown in Figure 2.3. EPI consists of a train of frequency-encoding gradients (G_{RO}) that alternate in polarity to traverse back and forth through k-space (k_{RO}) by forming gradient echoes. In order to step through the PE direction of k-space (k_{PE}), each of these gradients is separated by an additional phase-encoding gradient, or 'blip'.

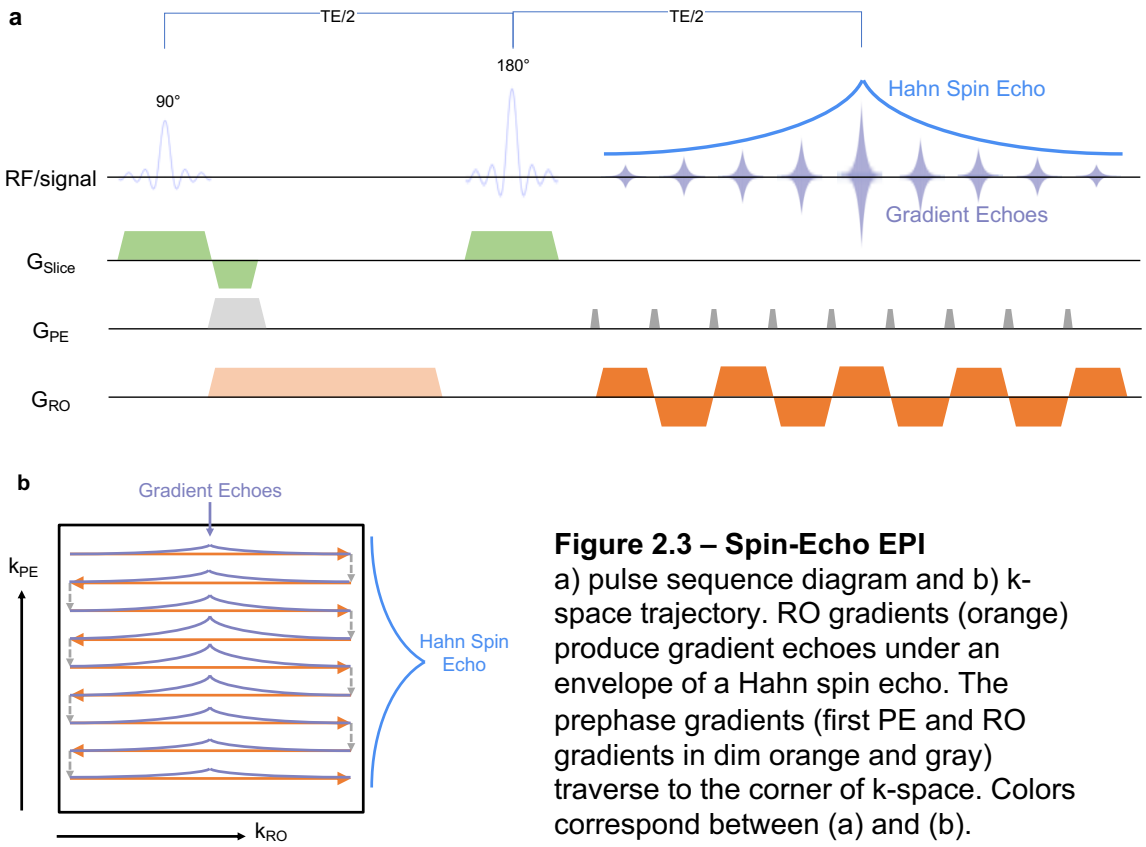

Figure 2.3 – Spin-Echo EPI
a) pulse sequence diagram and b) k-space trajectory. RO gradients (orange) produce gradient echoes under an envelope of a Hahn spin echo. The prephase gradients (first PE and RO gradients in dim orange and gray) traverse to the corner of k-space. Colors correspond between (a) and (b).

EPI can be used as the readout strategy underlying either a gradient echo or spin echo. The main differences between the two are signal weighting, scan time, and use cases. GE-EPI creates T_2^*-weighting in a very short scan time and is classically used for functional MRI scans in order to minimize the TR. The slower SE-EPI is typically used for DWI because the longer echo times allow for the addition of diffusion weighting gradients. While both GE-EPI and SE-EPI provide fast acquisition with relatively low power deposition, they are also associated with some characteristic challenges, including distortion, chemical shift displacement, and Nyquist ghosts.

EPI relies on a series of gradient echoes under the envelope of either another gradient echo or a Hahn spin echo, which forms at the center k_{PE} line (Figure 2.3b). Thus, any source of off-resonance (Δf) causes phase accumulation over the long echo spacing (t_{esp}), i.e. time between two echoes, causing a geometric shift (Δy_{PE}) in the image domain

along PE according to [Ref (23)]: $\Delta y_{PE} = \frac{\Delta f}{BW_{PE}} FOV_{PE}$ where Δf is measured in Hz and BW_{PE} refers to the effective bandwidth in the PE direction, i.e. $BW_{PE} = \frac{1}{t_{esp}}$. Note that the effect in the RO direction is negligible because the RO bandwidth is large in EPI.

Inhomogeneity in the B_0 field is one major source of off resonance that causes geometric distortion, as shown in Figure 2.4 (green arrow). Another large source of off resonance is the chemical shift of fat. Because the protons within water and fat molecules experience different amounts of shielding, their resonance frequencies differ by about 3.5 ppm, or ~440 Hz at 3 T. This also causes a shift by Δy_{PE} of the fat signal only, called chemical shift displacement (Figure 2.4, yellow arrows). Finally, due to the alternating polarity through the RO train, ghosting artifacts emerge in the presence of any gradient imperfections or eddy currents (Figure 2.4, red arrow). These artifacts will be explored further in subsequent sections.

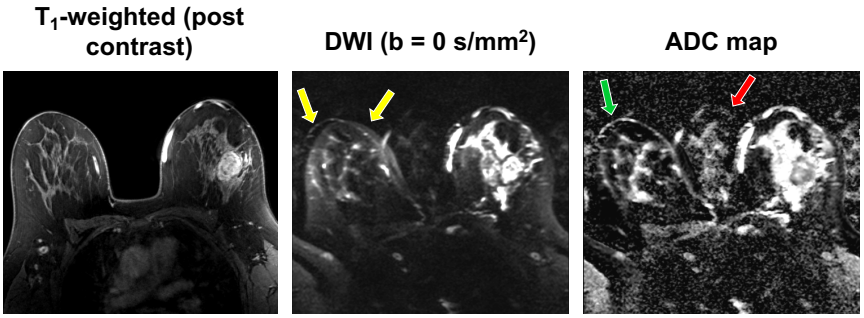

Figure 2.4 – Common DWI artifacts in breast imaging
Example of clinically available breast DWI and ADC map based on ACRIN 6698 protocol. A T_1-weighted anatomical is provided for comparison. Nyquist ghosts (red arrow), B_0 distortion (green arrow), and chemical shift (yellow arrows) are highlighted.

Distortion correction

EPI uses a low acquisition bandwidth in the PE direction so that any off resonance during this time will accumulate and cause dephasing. One major source of off resonance is B_0 inhomogeneity that is caused by non-uniform magnetic susceptibility of tissues, eddy currents, respiration, and subject motion. Because this inhomogeneity is spatially varying, this phase accumulation produces geometric distortion in the PE direction. The shimming system used in this work allows for B_0 corrections in the shape of spherical harmonics

(X, Y, Z, Z^2, ZX, ZY, X^2-Y^2, and XY), which produces adequate B_0 homogeneity in a sphere about the size of a human head at isocenter. However, the shimming available does not work as well for breast imaging due to the longer distance away from isocenter, non-spherical geometry, and close proximity to the lungs, demanding the need for retrospective distortion correction.

FSL's topup

The Centre for Functional Magnetic Resonance Imaging of the Brain (FMRIB) Software Library (FSL) provides software for analyzing fMRI, MRI, and DTI brain data, including topup (24–26) for retrospective correction of distortion in SE-EPI. Topup requires two images with opposite PE directions, and therefore equal and opposite distortions. It works by estimating the equal and opposite shift that would simultaneously result in both of the acquired images, from which a B_0 map can be calculated.

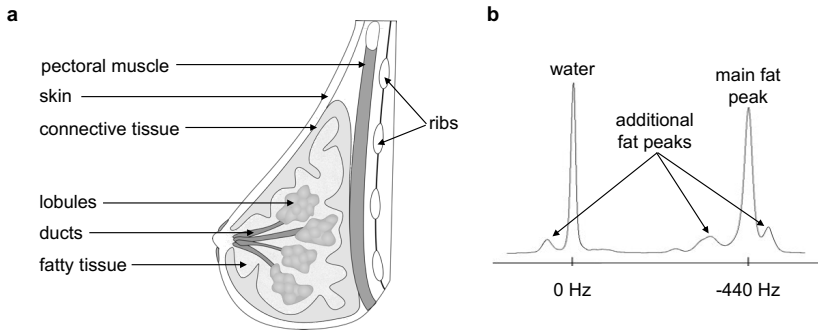

Modified from cancer.ca, courtesy of Dr. Geneva Hargis

Figure 2.5 – Signal from Adipose Tissue
Breast anatomy (a) contains glandular tissue (ducts and lobules) surrounded by a layer of fatty tissue. The fat spectrum (b), which includes four peaks surrounding that of water, makes fat suppression difficult. Frequencies listed correspond to 3 Tesla.

Fat suppression

The typical breast anatomy, shown in Figure 2.5a, consists of glandular tissue (ducts and lobules), where most breast cancers start, surrounded by a layer of fatty tissue. However, breast anatomy, unlike many other organs, is very heterogeneous across the population, including the fat content of breast tissue. In the BI-RADS system, for example, radiologists classify each patient's mammographic results base on the categories: almost entirely fatty (A), scattered areas of fibroglandular density (B), heterogeneously dense

(C), and extremely dense (D). This potentially large fat signal can be detrimental in EPI, due to chemical shift artifact, difficult B_0 shimming due to varying magnetic susceptibility, and phase shifts that disrupt assumptions used in things like ghost and distortion correction (see Experiment 3 in Section 3.3.1). Furthermore, residual fat signal can bias ADC and other quantitative measures. Thus, high quality breast DWI is dependent on robust fat suppression across a heterogeneous population. Fat suppression can be challenging, however, as there are 4 resonance peaks, that span either side of that of water, as shown in Figure 2.5b.

Figure 2.6 – Common fat suppression
SPAIR (a) uses a spectrally selective pulse to excite fat and applies the excitation when the fat signal is nulled based on the T_1 relaxation. This delay adds some scan time. In gradient reversal (b) the slice select gradient is reversed during the refocusing pulse so that the chemical shift displacement occurs in the opposite direction. Only the fat region of overlap (purple) is refocused.

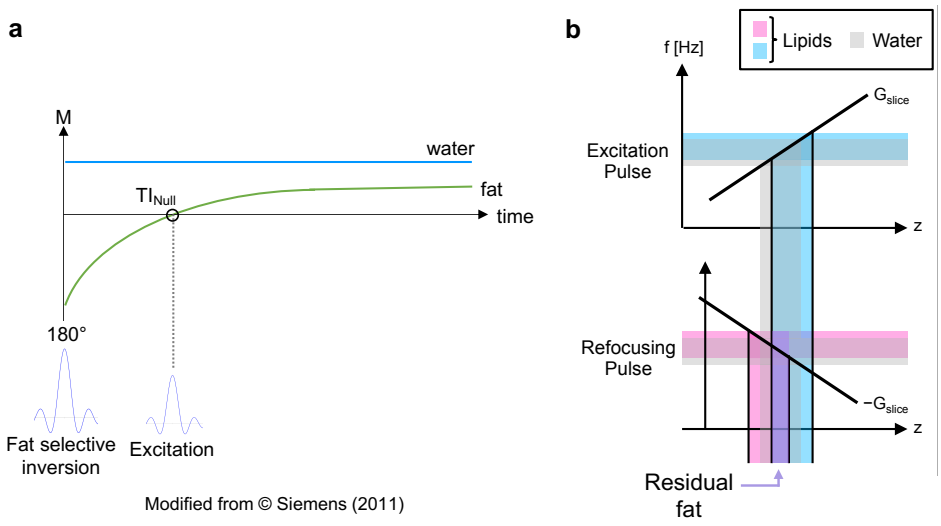

Modified from © Siemens (2011)

There are several approaches for fat suppression. Siemens commonly uses spectral selection attenuated inversion recovery (SPAIR) in combination with section-select gradient reversal (27). SPAIR applies a spectrally selective 180° RF pulse to invert fat only (Figure 2.6). Subsequent excitation is delayed based on the T_1 of fat so that the $M_z = 0$ at the time of the RF pulse, essentially nulling the fat signal for the rest of the acquisition. The gradient reversal strategy is best described in Figure 2.6b. The slice-select gradient is reversed during the refocusing pulse, which shifts the slice of fat that experiences the 180° pulse. This reduces the amount of fat that is refocused based on the

two slice profiles of fat but does not fully suppress the fat signal, as there remains a region of overlap between the two slices. Moreover, SPAIR's spectrally selective pulse is sensitive to B_0 and B_1 inhomogeneity, so its performance is often insufficient for the purpose of breast DWI.

2.2 Accelerated Imaging

Another way to reduce geometric distortion, chemical shift artifact, and T_2^* signal loss is to increase the PE acquisition bandwidth, i.e. to speed up the acquisition in the PE direction. Additionally, one of the major limitations of MRI is the long scan times required to fill k-space, which contribute to the high cost of MRI scans, cause patient discomfort, and lead to image artifacts from breathing and other motion that occurs during scanning. The speed at which k-space is acquired, however, is limited because the sampling in k-space, Δk, must be at least as small as $\frac{1}{L_{object}}$ to acquire an imaging without aliasing. In other words, $\frac{1}{\Delta k}$ corresponds to the FOV, which must include the full object in image space. Failure to satisfy this sampling criteria, known as the Nyquist sampling theorem, causes aliasing in the image domain as shown in Figure 2.7.

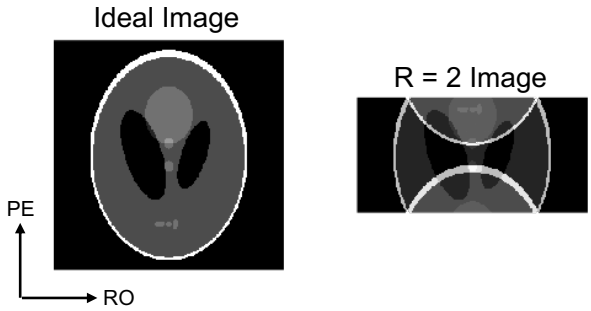

Figure 2.7 – Aliasing in the Image Domain
A simulated Shepp Logan phantom with R = 2 undersampling in PE.

In the readout direction the sampling rate is fast as it depends primarily on the ADC converter. In contrast, every additional sample in the phase encoding direction requires an additional phase encoding gradient and echo paired with a readout. Thus, although the scan time is defined by many different factors, it is approximately

proportional to the number of lines required in k_y, $N = \frac{2k_{y,max}}{\Delta k_y}$. Several tricks can be used to reduce the number of lines in k_y to minimize the scan time, but each corresponds to a tradeoff. Decreasing $k_{y,max}$ reduces the resolution in y; reduced FOV imaging requires 2D spatially selective RF pulse, which can be long and sensitive to B_1 inhomogeneity; and increasing Δk_y causes aliasing.

The concept of parallel imaging was introduced in 1988 by Hutchinson and Raff, who suggested using a large number of receiver coils in place of phase encoding. The idea was later refined and demonstrated in k-space by Sodickson and Manning in 1997, which they named SiMultaneous Acquisition of Spatial Harmonics (SMASH) (28), and in the image domain by Pruessman et al. in 1999 called SENSitivity Encoding (SENSE) (29). Parallel imaging has since been largely expanded, incorporating many types of regularization, compressed sensing, machine learning etc. In current practice, most reconstruction is based on SENSE or GeneRalized Autocalibrating Partially Parallel Acquisitions (GRAPPA), a more recent k-space based method (30). While there are many variations of PI reconstruction, they are all based on the concept that each channel in a receiver array is sensitive to a unique area in space, known as the sensitivity profile. This spatial encoding, learned using the sensitivity profiles, is combined with information within the gradient encoding to reconstruct an alias-free image from undersampled data.

2.2.1 Parallel Imaging

Formulation in the image domain: SENSE

Let's consider the signal equation, $s(k_x, k_y) = \int m(x,y) e^{-i2\pi(k_x x + k_y y)} dxdy$, which describes the signal at a given point in k-space (k_x, k_y) for an image, m, ignoring noise. For simplicity assume a constant gradient, G_x over time t; we can say $k_x = \int_0^t G_x(\tau) d\tau = G_x t$ and, similarly, $k_y = G_y t$. Then $(k_x, k_y) = \int m(x,y) e^{-i2\pi(G_x x + G_y y)t} dxdy$. For each coil, j, the actual signal received is determined by a combination of its sensitivity profile, $S_j(x,y)$, the object, and the gradient encoding as: $(k_x, k_y) = \int S_j(x,y) m(x,y) e^{-i2\pi(G_x x + G_y y)t} dxdy$.

Now consider a simple system with 2 surface coils and an undersampling or reduction factor of $R = 2$, as shown in Figure 2.8. The aliased pixel is a linear combination of two pixels in k-space, we'll call A and B. The signal intensity (I) in Coil 1 can be given by $I_{1\_alias} = S_{1A}A + S_{1B}B$ and in Coil 2: $I_{2\_alias} = S_{2A}A + S_{2B}B$. If the sensitivity profiles can be measured, we have two equations with two unknowns, A and B, and it is possible to solve for the unaliased image. This example can be generalized for any number of coils (N_{Ch}) and undersampling factor of $R < N_{Ch}$, where the signal in a given coil is described as $I_{j\_alias} = \sum_{i=1}^{R} S_{ij}x$, or more compactly in matrix notation, as:

$$\vec{I} = S \cdot \vec{x} \qquad [2.1]$$

where $\vec{x}$ represents the R pixels of the unaliased image and the matrix S contains the sensitivity profiles for each coil at each aliased position. Thus, it is possible to solve for the unaliased image by $\vec{x} = S^{-1} \cdot \vec{I}$. More generally, if the inverse of S does not exist,

$$\vec{x} = (S^H S)^{-1} S^H \cdot \vec{I} \qquad [2.2]$$

where H indicates the transposed complex conjugate.

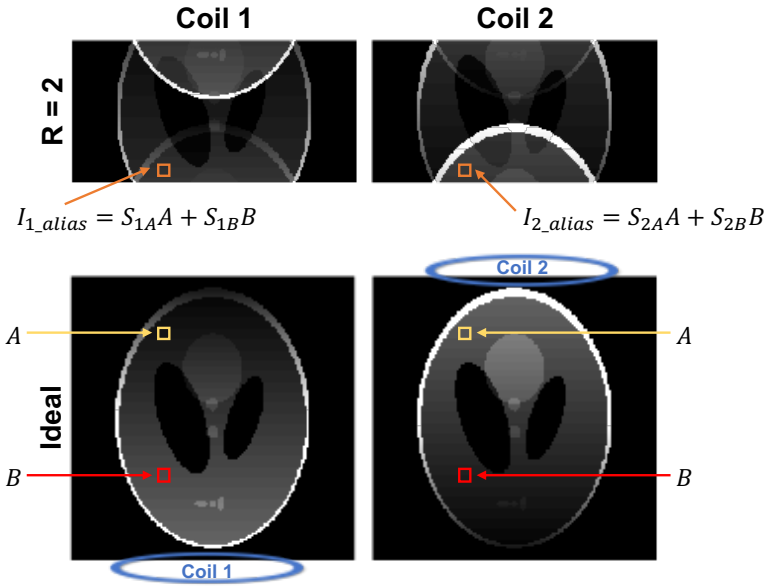

Figure 2.8 – SENSE Formulation
Shepp-Logan phantom simulated for 2 coils (blue) and R = 2. For each coil, each aliased pixel (orange) can be described as a linear combination of R pixels (A and B) weighted by that coil's sensitivity profiles.

Formulation in k-space: GRAPPA

Although Parallel Imaging is more intuitive in image space, the same principles apply in k-space. Specifically, Equation 2.1 can be written as

$$\hat{I} = \hat{S} \otimes \hat{x} \qquad [2.3]$$

based on the Fourier principle that multiplication in the image domain corresponds to convolution in frequency space, where the hat ($\hat{}$) denotes the k-space domain. Here, the sensitivity profiles are in the form of weights or kernels, and the convolution is done through k-space.

GRAPPA is based on the concept that an unacquired line in k-space, m, for a given channel, j, can be represented as a linear combination of the surrounding points of k-space, b steps away, of all the other channels, l. In equation form (30):

$$I_j(k_y - m\Delta k_y) = \sum_{l=1}^{N_{Ch}} \sum_{b=0}^{N_y N_x} S(j,b,l,m)x(k_y - bR\Delta k_y) \qquad [2.4]$$

In practice, the number of blocks can be chosen as $N_b < N_y N_x$.

Reference data

The previous discussion assumed that $S(x,y)$ or $S(j,b,l,m)$ is known. In practice, the sensitivity profiles or k-space weights need to be estimated from reference data that is fully sampled. In image space, the sensitivity profiles can simply be estimated by comparing the signal magnitude from each channel to the signal in a coil-combined fully sampled image. In k-space, the weights are calculated by solving equation 2.4, where the left-hand side is known. An autocalibration scan (ACS), typically acquired with low resolution, is used to fill in I_j above. Thus,

$$I_j^{ACS}(k_y - m\Delta k_y) = \sum_{l=1}^{N_{Ch}} S_l^m I_l^{ACS}(k_y) \qquad [2.5]$$

Equation 2.5 is fit across many kernels throughout the ACS lines to estimate the set of weights $S(j,b,l,m)$.

Noise in parallel imaging

Parallel imaging affects the SNR in two distinct ways. First, the theoretical SNR of an image is proportional to the size of a voxel and the square root of the total sampling time, i.e.

$$SNR \propto \Delta z \frac{FOV_x}{N_x} \frac{FOV_y}{N_y} \sqrt{NEX\ N_y \frac{N_x}{BW_{rec}}} \quad [2.6]$$

where Δz is the slice thickness, NEX is the number of excitations or averages, and BW_{rec} is the receiver bandwidth. In parallel imaging the number of points acquired in the PE direction, N_y, is reduced by a factor of R (31). If total scan time is not limited, this reduction can be mitigated by a corresponding number of averages.

Additionally, there is an SNR cost of acceleration that is dependent on the geometry of the coils with respect to the object. The previous sections ignored noise and assumed that the sensitivity profiles were fully unique to each coil. In reality, the coil sensitivity maps contain noise and overlap with one another in some regions, which reduces the ability to solve the system of equations. This reduces the SNR by the geometry factor, g, which is spatially varying because it measures the correlation between coils. Therefore, the overall SNR of an accelerated image is $SNR_{accel} = \frac{SNR_{full}}{\sqrt{R} g(x,y)}$, where $g(x,y)$ was formulated in the seminal SENSE paper as $g_{x,y} = \sqrt{[(I^H \Psi^{-1} I)^{-1}]_{x,y} [I^H \Psi^{-1} I]_{x,y}}$, where Ψ is the sampling noise matrix (29). Importantly, $g(x,y) > 1$, always.

2.2.2 Simultaneous multislice imaging

The parallel imaging discussed to this point is limited to the phase encoding direction. While it can be applied along two axes in 3D imaging, in 2D imaging, only one of the three directions can be accelerated with SENSE, GRAPPA etc. It is also limited by the number of receiver coils and the distinction between sensitivity profiles in the PE direction. Thus, it is desirable to extend the concept into the slice encoding direction.

One can take advantage of the varying coil sensitivities in two different directions through space, and greatly reduce scan time by reducing the number of slice excitations needed. Simultaneous multislice (SMS) imaging, alternatively known as multiband (MB)

imaging, is an acceleration technique similar to that described in the PE direction. While the concept was proposed in 1988 (32), it wasn't until parallel imaging saw major advancements that SMS was practically introduced in a way that sped up acquisition by Larkman et al. in 2001 (33).

The concept and reconstruction of SMS is very similar to that of acceleration techniques in the PE direction, with a few important distinctions. In SMS imaging, RF pulses are used to excite several slices simultaneously (Figure 2.9). As in PE acceleration, the aliased image can be described as a superposition of slices of the ideal image modulated by the coil sensitivity profiles, which allows for unaliasing of the image using matrix inversion to solve the system of equations. Like in-plane undersampling, the sensitivity profiles or kernel weights are estimated based on a fully sampled reference dataset, referred to as the single band (SB) reference. While in-plane undersampling reduces the amount of data acquired in PE, by R, SMS still acquires a full set of data for each slice. Thus, SMS does not affect the echo spacing or the number of lines acquired, and therefore does not achieve reduced distortion from phase accumulation as PE undersampling does. However, it also does not suffer from a $\sqrt{R}$ reduction in SNR. Moreover, SMS requires some distinct considerations for slice excitation.

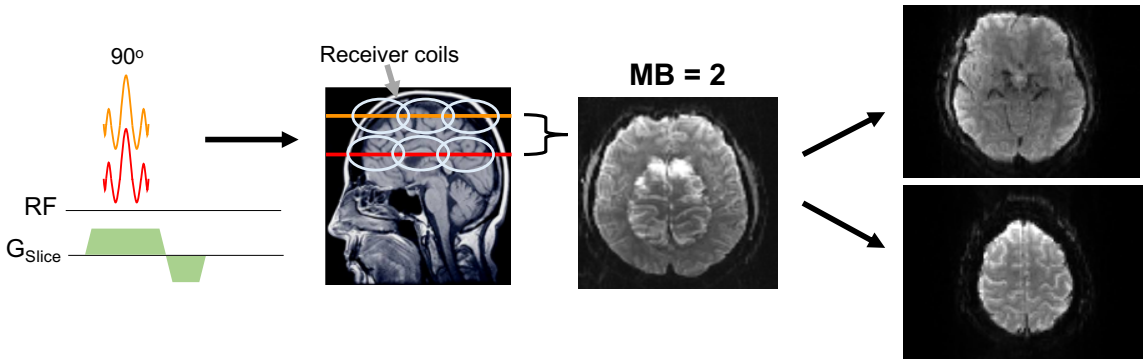

Courtesy of Dr. Patrick Bolan

Figure 2.9 – Simultaneous Multislice (SMS) Example for MB = 2
Spectrally selective excitation pulse excites two slices, causing aliasing in the slice direction. Sensitivity profiles are used to separate slices.

In typical 2D imaging, a finite slice is excited using a specific RF pulse in conjunction with a slice select gradient, as shown in Figure 2.9. The RF pulse can be described through time as $RF(t) = A(t)P(t)$, where the amplitude $A(t)$ determines the

slice profile and $P(t)$ describes a phase according to: $P(t) = e^{i\Delta\omega t+\varphi}$, where $\Delta\omega$ determines the slice position and φ determines the phase at the echo. In SMS, various RF pulses can be added together to excite an arbitrary number of slices, which is referred to as MB, or the multiband factor. The RF pulse becomes:

$$RF_{SMS}(t) = A_n(t)\sum_{n=1}^{MB} e^{i\Delta\omega_n t+\varphi_n} \quad [2.7]$$

where $A_n(t)$ represents an arbitrary slice profile that can vary based on the slice and transmit channels to improve sensitivity to B_1 inhomogeneity with parallel transmission.

Challenges of SMS

The main issue that SMS faces is the increased power demands with increasing RF pulses. The desired excitation in SMS often requires RF pulses that exceed the peak power abilities of the amplifier or increase the total power deposition beyond safety limitations of the specific absorption rate (SAR). To reduce the power requirement, one can increase the duration of the RF pulse. However, this can negatively impact the sequence timing, worsen the sensitivity to off-resonance, and increase the effect of T_2^* decay (34). Finally, SMS reconstruction faces a spatially varying increase in noise according the g-factor, as described in Section 2.2.1.

CAIPIRINHA

One major development in SMS imaging is a method called Controlled Aliasing in Parallel Imaging Results in Higher Acceleration (CAIPIRINHA). CAIPIRINHA was developed to improve g-factors in Parallel Imaging by separating the aliased images in space. Similarly, with SMS imaging, CAIPIRINHA involves shifting the slices to reduce the overlap between slices, as shown in Figure 2.10. The geometry can be modified in order to increase the variation in sensitivity profiles within the PE direction and improve the condition of the system of equations, potentially improving image quality and allowing for higher acceleration factors (35).

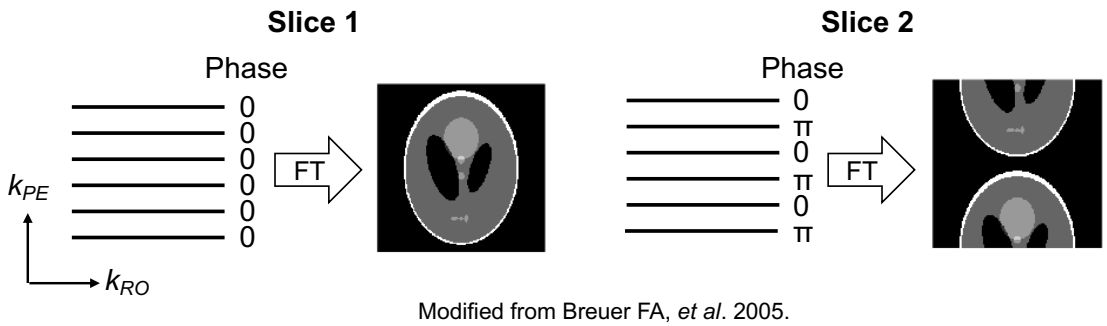

Modified from Breuer FA, *et al*. 2005.

Figure 2.10 – CAIPIRINHA
Modulating the phase of every other line causes a FOV/2 phase shift.

One easy way to shift the slices relies on the Fourier shift theorem, in which a phase ramp in k-space corresponds to a shift in the image domain. In terms of the signal equation, a shift of Δy in the image domain can be described by:

$$M(x, y - \Delta y) = \int m(k_x, k_y) e^{+i2\pi(k_x x + k_y y)} dk_x dk_y \cdot e^{-i\Delta y k_y} \qquad [2.8]$$

For example, in a simple case imaging the brain with MB = 2, to shift the slice by $\Delta y = \frac{FOV_y}{2}$, the phase ramp corresponds to $\frac{2\pi}{2}$ per Δk_y, which is equivalent to alternating the phase by π between every line because of the periodicity in k-space, as shown in Figure 2.10.

The original formation of CAIPIRINHA is not compatible with EPI in which all of the phase encoding lines are read out after a single RF excitation, therefore not allowing for a phase modulation between lines. A more recent strategy, called blipped-CAIPI, applies small gradients in the slice encoding direction at the same time of the PE blips for the EPI readout. These gradient "blips" add a phase offset to the given lines of k-space, which is rewinded using a blip of opposite polarity (36).

2.3 Diffusion Methods

2.3.1 Diffusion encoding

The purpose of diffusion encoding is to modify the image signal based on the rate of diffusion of the water molecules within the tissue. Classically, diffusion weighting is

achieved using a Stejskal-Tanner diffusion sequence, also called monopolar diffusion, that is incorporated into an imaging sequence prior to the readout. In a Stejskal-Tanner diffusion sequence, following the excitation, a pair of equal diffusion gradients are played surrounding a 180º refocusing pulse (Figure 2.11a). During the first gradient, the spins dephase based on their position in the direction of the diffusion gradient, and magnitude and duration of the gradient, G_{Diff} and δ. With the 180º pulse, the direction of the spins' precession is flipped so that a 2nd gradient, which is equal to the first, will rephase the stationary spins. However, spins that experience motion between the two gradients will experience unequal magnetic fields before and after the 180º pulse. Thus, these mobile spins will not fully rephase causing signal loss based on the rate of diffusion and the strength and timing of the diffusion weighting.

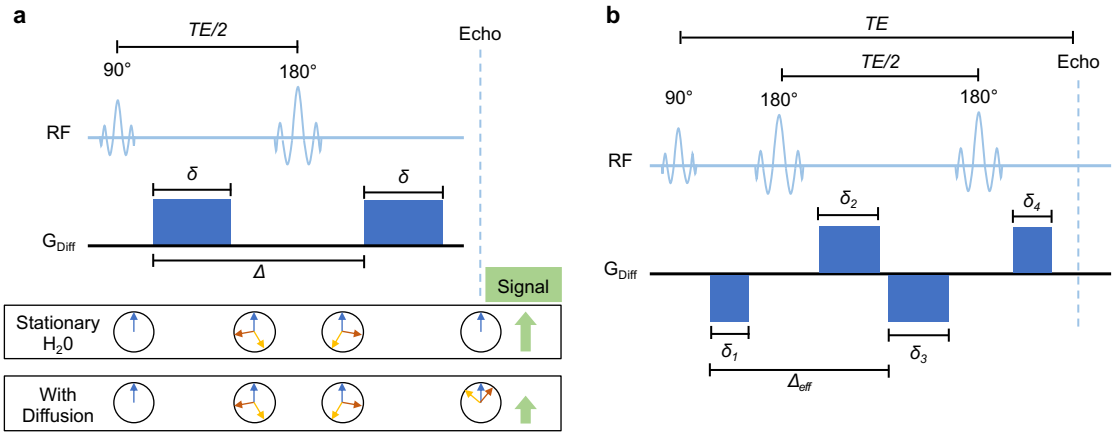

Figure 2.11 – Diffusion Encoding
a) Stejskal-Tanner (monopolar) diffusion sequence using spin echo. G_{Diff} can be applied on any combination of spatial axes to measure directional diffusion. Spins of stationary water molecules fully refocus. Spins of moving water molecules experience unequal gradients, reducing the signal (green). The magnitude of G_{Diff}, δ, and Δ determine the diffusion weighting.
b) Bipolar diffusion sequence, which reduces eddy current effects but requires longer TE and spoilers (not shown). The b-value can be calculated by considering each pair of diffusion gradients to be like a single diffusion gradient in the monopolar scheme. Thus, Δ relates to Δ_{eff} and $\delta_{eff} = \delta_1 + \delta_2 = \delta_3 + \delta_4$.

For a monopolar diffusion scheme, the diffusion weighting is described by the b-value according to: $b = \gamma^2 {G_{Diff}}^2 \delta^2 \left(\Delta - \frac{\delta}{3}\right)$ where Δ is the separation between the gradient pair and γ is the gyromagnetic ratio of Hydrogen, in this case. The diffusion

gradient can be played in any combination of x, y, and z to probe the diffusion in any direction on a sphere.

While monopolar diffusion allows for a short TE, the use of strong gradient pulses can create eddy currents that causes distortion in the PE direction of the image that is inconsistent across b-values and diffusion directions. An alternative method, called bipolar diffusion, uses a pair of refocusing pulses and two pairs of diffusion gradients to reduce these gradient-induced eddy currents. In the bipolar diffusion scheme, shown in Figure 2.11b, the diffusion gradients are played as two bipolar pairs (37). The reversed gradient will induce nearly equal and opposite eddy currents that cancel out those generated by the first gradient, thus reducing the eddy current effects in the echo. The use of two refocusing pulses, however, increases the power deposition and requires a much longer echo time, which both reduce SNR. Additionally, the second refocusing pulse can illicit complicated echo pathways that requiring additional spoiling gradients.

2.3.2 Standard SE-EPI

DWI is most commonly acquired using single-shot (SS) spin-echo echo-planar imaging (SE-EPI), combining the standard SE-EPI scheme (Figure 2.3) with a diffusion encoding scheme around the refocusing pulses (Figure 2.11). SE provides a long enough echo time to incorporate diffusion gradients, and the fast acquisition speed of EPI facilitates the measurement of a wide range of b-values and diffusion directions (i.e. the axis chosen for G_{Diff}) within a reasonable scan time. Additionally, because SS SE-EPI acquires a full k-space in one shot, it does not suffer from phase differences between the TRs, which are caused by even small movement during the diffusion gradients. However, SE-EPI produces DWI of limited spatial resolution and quality as discussed earlier. SE-EPI has been advanced in several ways to mitigate these challenges. Other less common methods have also been applied to DWI, each with its own tradeoffs.

2.3.3 Advanced SE-EPI

Multishot EPI

In single shot SE-EPI the resolution depends on the echo train length, which is limited by the T_2 signal decay of the spin echo. Additionally, any B_0 inhomogeneity causes phase accrual over every line of k-space and results in often severe geometric distortion in the PE direction. One obvious way to extend SE-EPI and reduce these problems is to acquire the full k-space across several TRs rather than in a single shot. This method is referred to as multishot EPI (MS-EPI) and can reach a high spatial resolution with geometric distortion reduced by a factor equal to the number of shots used (N_{shot}) but also increases the scan time by a factor of ~N_{shot}.

As previously mentioned, each shot will have its own spatially varying phase according to the motion that occurs during the diffusion gradients, including small body movement, respiration, cardiac motion, or even pulsation of the CSF. If left uncorrected, the shot-to-shot phase differences will manifest as a ghosting artifact in the image. Many phase correction methods have been proposed throughout the literature. The most straightforward approach acquires a 2D navigator as a second echo after the acquisition that is used to estimate and correct the phase difference. MUSE (multiplexed sensitivity-encoding) is a more recent navigator-free method that estimates the phase map using parallel imaging techniques, and other methods iteratively estimate the phase based on a low rank, often including deep-learning (38–42).

In breast imaging, respiratory motion contributes to large phase errors between shots. Thus, MS-EPI is challenging in breast DWI and rarely used, especially as large acceleration factors in-plane can have the same benefit on distortion without the large increase in time and circumventing shot to shot differences. Hu et al. applied MS-EPI in breast with MUSE, which is an extension of SENSE reconstruction. They found that MS-EPI improved lesion conspicuity and perceived image sharpness. However, they did not realize an improvement in distortion, as the number of shots was equal to the undersampling factor in SS-EPI, and they found that MS-EPI increased the image artifact (43). Hu et al. also proposed an alternative phase correction called locally low-rank (LLR) for severe motion (44).

Readout-segmented EPI

Readout-segmented (RS) EPI (called RESOLVE by Siemens) is another multishot approach that segments the k-space in the RO direction rather than through the PE direction (45). By segmenting in the RO direction with N_{shot}, the echo time can potentially be reduced by a factor of about N_{shot}, which reduces the geometric shift and image blurring from T_2^* decay, and TE accordingly. As segmenting is done in the RO direction, RS-EPI is also a good candidate for in-plane undersampling in the PE direction, which can further reduce geometric distortion and T_2^* decay (46).

Similar to other multishot techniques, RS-EPI requires more excitations and therefore suffers from longer scan time. Moreover, it is subject to non-linear phase errors that are caused by movement throughout the diffusion gradient that varies across shots. These phase differences are generally corrected using a 2D navigator that is required with every shot, further increasing the scan time. The navigator is used to estimate and remove the shot-specific phase before combining the shots into a full k-space. However, if the motion is severe, the phase errors may not be readily estimated from the navigator as the center of k-space may shift outside the navigator region (46).

As a widely available product diffusion sequence, RS-EPI has been used for breast DWI, often with high spatial resolution. Several reports suggest that RS-EPI is superior to SS-EPI in diagnostic performance (47–50). Baltzer et al. even showed that the diagnostic performance of RS-EPI was comparable to that of DCE-MRI, suggesting RS-ESPI as a non-contrast alternative (51).

Reduced-FOV

In reduced-FOV, or rFOV, RF pulses are applied in a way that excites a specified FOV, generally smaller than the size of the actual object in the PE direction, followed by a typical EPI readout. A smaller FOV corresponds to relaxed sampling requirements without the use of PI techniques, as $\Delta k = \frac{N}{FOV}$, which reduces geometric distortion and T_2^* blurring. There are three main strategies for excitation, including inner volume imaging, outer volume suppression, and 2D spatially selective RF pulses for localized excitation followed by a standard slice-selective refocusing pulse (46). Unfortunately,

rFOV's increased demands on RF pulses can cause increases in SAR, scan time, and limitations on slice selection (46).

Reduced-FOV imaging is a promising candidate for an advanced SE-EPI acquisition in breast imaging, typically acquired axially with PE in the HF direction. Results suggest that using rFOV to achieve a higher resolution helps to better characterize the heterogeneity of tumors and improves the measurement of low b-values characteristic of malignancies (52–54).

2.3.4 Alternative methods

Many other methods have been explored to overcome the disadvantages of SE-EPI. These methods are often applied to brain imaging initially and are applied to body imaging much less frequently due to the additional challenges of imaging the body.

Turbo spin-echo

In single shot turbo spin-echo (TSE) or fast spin-echo (FSE), which is also often called HASTE, an RF refocusing pulse is added between every PE line of k-space. Compared to standard SE-EPI, TSE has little to no geometric distortion in the PE direction because the RF pulse refocuses the phase of every readout. However, playing the refocusing pulse requires a substantial amount of time, which increases the overall scan time. Moreover, it is difficult to satisfy the Carr-Purcell-Meiboom-Gill (CPMG) condition of the refocusing pulses because the phase accrued is spatially varying and depends on the motion occurring during the diffusion gradients. One popular strategy to overcome this challenge is to use gradients to crush the non-CPMG component of the signal, but this greatly reduces the SNR.

Another variation of a TSE sequence combines the RF refocusing pulses with a short EPI-like RO, trading off the advantages and disadvantages of both SE-EPI and TSE. This method is called gradient- and spin-echo (GRASE) and involves adding RF refocusing pulses between groups of readouts rather than for every line (55).

TSE can also be applied in a non-cartesian way in a method called periodically rotated overlapping parallel lines with enhanced reconstruction (PROPELLER) (56).

PROPELLER is a multishot technique that covers k-space with a set of "blades" that each pass through the center of k-space to allow for self-navigating in post processing. This method still faces the challenges of the non-CPMG component but is free of geometric distortion and can reach high spatial resolutions provided the blades are wide enough for sufficient phase correction between shots.

Steady-state free precession

In steady-state free precession (SSFP), the signal is rapidly excited with a small flip angle with a TR < T_1, such that the signal does not fully recover between excitations. Although the small flip angle causes a low signal, the sequence is so efficient that it allows for large amounts of data to be acquired in a short period of time, which salvages the SNR (57). However, DW-SSFP faces two major challenges. As a 3D sequence, SSFP requires segmentation in order to fully sample k-space, which subjects it to phase errors between shots as described above. Additionally, SSFP creates a complicated combination of spin and stimulated echo coherence pathways, which creates a signal weight that is highly dependent upon T_1, T_2, and the flip angle. Thus, defining diffusion weights (or b-values) becomes complicated and requires measurement of T_1, T_2, and B_1 maps in order to achieve ADC quantification (57).

Unbalanced SSFP was first applied to breast imaging. in 2014 by Granlund et al. using a double-echo steady-state (DESS) sequence (58). They achieved full coverage diffusion weighted images within 3 minutes and 35 seconds with higher nominal resolution than SE-EPI acquired in a longer scan time (5:41). They reported that radiologists preferred DESS images compared to standard DWI with respect to resolution and level of distortion.

Spatiotemporal encoding

Spatiotemporal encoding (SPEN) is a single shot imaging method that progressively excites and refocuses the signal through space using frequency-swept pulses with quadratic phase played in the presence of a magnetic gradient. Three inherent advantages of SPEN that make it a good candidate for DWI are 1) it is insensitive to field inhomogeneities; 2) it achieves true T_2 weighting, and thus does not suffer from T_2^*

blurring; and 3) it is robust against chemical shifts. However, the additional encoding gradient in SPEN causes additional weighting that leads to spatially varying b-values.

Solomon et al. proposed SPEN for breast imaging achieved ADC maps with markedly lower distortion and ghosting artifact compared to SE-EPI, without significantly affecting the ADC measurement. However, the frequency-swept inversion pulse caused high SAR deposition, which limited the number of slices that could be acquired (59,60).

2.4 Diffusion Models

2.4.1 ADC and cellularity

The most basic DWI model measures the apparent diffusion coefficient (ADC), which captures both the pure Brownian diffusion of the water within the tissue along with pseudo-diffusion, e.g. perfusion (61). To measure the ADC, diffusion weighting is integrated into an imaging sequence as described in Section 2.3.1. This diffusion weighting, described by the b-value (b), affect the signal intensity (S) based on the ADC of the water molecules within the tissue according to (62):

$$S(b) = \mathrm{S}_0 \exp(-b * ADC) \qquad [2.9]$$

where S_0 is the signal intensity in the absence of a diffusion gradient. By acquiring a series of images with at least two b-values, a quantitative ADC value can be calculated on a pixel-by-pixel basis by solving Equation 2.9 according to the signal attenuation between the images. When using the ADC, it is typically assumed that the diffusion is isotropic. Therefore, if several averages are acquired, the diffusion gradients are often applied in three orthogonal directions and averaged together to get a directionless ADC value.

This basic DWI has clinical value in various fields. In brain and body imaging, low ADC values are associated with malignancies, and increasing ADC values serve as an early indication of treatment response prior to conventional anatomical measurements (63). In neuroimaging, the high-b-value images are often used to assess damage caused by acute ischemic stroke.

While the ADC is the most widely used diffusion-based metric used in breast imaging due to its simplicity and clinical usefulness, true diffusion is not always isotropic, gaussian, and fully modeled with the monoexponential shown in Equation 2.9. Many other models have been established that attempt to include these other complexities, like non-gaussian diffusion, perfusion, directionally dependent restriction of diffusion, etc.

2.4.2 DTI and anisotropy

While ADC maps assume isotropic diffusion (or at least ignore anisotropy by averaging over several diffusion directions), diffusion tensor imaging (DTI) models 3D Gaussian free diffusion. Rather than measure a scalar value for diffusion, in DTI diffusion is described by a directional apparent diffusion tensor, $\boldsymbol{D}$. Thus, equation 2.9 can be expanded as $S(b) = S_0 \exp\left(-\left(b_{xx}D_{xx} + 2b_{xy}D_{xy} + 2b_{xz}D_{xz} + b_{yy}D_{yy} + 2b_{yz}D_{yz} + b_{zz}D_{zz}\right)\right)$, where b_{ij} and D_{ij} are components of the matrices $\boldsymbol{b}$ and $\boldsymbol{D}$, respectively. To solve for $\boldsymbol{D}$, one must apply diffusion gradients along at least six directions (64).

It is then convenient to define several parameters which will describe the diffusion based on the diffusion tensor, $\boldsymbol{D}$, that are independent of the orientations of the laboratory frame, the object in the scanner, and $\boldsymbol{b}$. The diffusion can be characterized by ellipsoids where the surface represents the average distance traveled by a water molecule. The ellipsoids are described with three principle directions, $\varepsilon_{x\prime}$, $\varepsilon_{y\prime}$, and $\varepsilon_{z\prime}$, which are coincident with the eigenvectors of $\boldsymbol{D}$, $\lambda_{x\prime}$, $\lambda_{y\prime}$, and $\lambda_{z\prime}$, where the laboratory frame, x, y, and z has been rotated to x', y', and z' to align with the principle directions of diffusion. These eigenvectors are typically sorted by size and described as λ_1, λ_2, and λ_3.

Another relevant quantity is the overall size of the ellipsoid, which is proportional to the mean diffusivity, $\langle D \rangle = \frac{1}{3}\left(D_{xx} + D_{yy} + D_{zz}\right) = \frac{1}{3}(\lambda_1 + \lambda_2 + \lambda_3)$. While $\langle D \rangle$ is related to ADC, ADC assumes isotropic diffusion, whereas $\boldsymbol{D}$ is more general and is independent of direction. For example, changes in $\langle D \rangle$ should truly reflect a change in the overall diffusivity of the tissue, while a change in the ADC value could be caused by changing the diffusion direction.

The shape of the ellipsoid is also important and is often measured in terms of anisotropy (65), which characterizes the amount of which the ellipsoid is non-spherical. The Fractional anisotropy (FA) is defined as:

$$FA = \frac{3}{\sqrt{2}} \frac{\sqrt{Var(\lambda)}}{\sqrt{{\lambda_1}^2 + {\lambda_2}^2 + {\lambda_3}^2}} \quad [2.10]$$

and is a measure between 0 and 1 that represents the fraction of diffusion that is anisotropic, as its name suggests. The FA is often displayed in a colormap where the color indicates the direction of the largest eigenvalue. One extension of DTI is fiber tractography, in which axonal maps are inferred based on the main direction of diffusion from voxel to voxel in a deterministic or probabilistic way.

DTI is frequently used in neuroimaging for both research and clinical applications. Axonal pathways can help with surgical planning prior to brain tumor resection (66). In multiple sclerosis (MS) patients, MS lesions have been found to have increased mean diffusivity and decreased fractional anisotropy, which correspond to disruption to the axons and myelin (66). Other clinical applications include Alzheimer disease, diffusion axonal injury, and epilepsy.

DTI is much less commonly used in breast imaging. Some groups have suggested that the mammary ductal network and surrounding stroma are characterized by anisotropy, which may be disrupted by malignancy (67). Some studies suggest that FA or other combinations of the eigenvalues can be used to differentiate between benign and malignant tissue (68,69). However, results are conflicting and the use of DTI in breast imaging remains controversial and requires further investigation.

2.4.3 DKI and non-Gaussian diffusion

The monoexponential diffusion model considered in Equation 2.9 assumes a Gaussian distribution of diffusion, based on the physics of free diffusion. At high b-values the diffusion has been shown to become less Gaussian, requiring a more complex model to accurately fit the data. Diffusion kurtosis imaging (DKI) is an extension of the DWI model that measures the non-Gaussian component according to: $S(b) = S_0 \exp\left(-b *\right.$

$D_{app} + \frac{1}{6} b^2 * D_{app}^2 * K_{app}\Big)$. D_{app} is the diffusion coefficient, which is similar to ADC that has been corrected for the non-Gaussian component. K_{app} measures the apparent diffusional kurtosis, quantifying the non-Gaussian component, or in other words, how peaked the distribution is.

The underlying biophysical principles that determine ADC and K_{app}, alike, are not fully understood. The most accepted hypothesis suggests that at low b-values ($b < 1000\ s/mm^2$), ADC measures the diffusion in extracellular space and thus reflects cell density (70). K_{app} is thought to represent the interaction between the water with cell membranes and the diffusion in the intracellular space (70), which may cause increased kurtosis in irregular and heterogeneous environments like malignancies (71,72). Thus, DKI has been applied in breast imaging for classifying benign and malignant breast lesions and been associated with histologic grade (67). However, DKI proves challenging in breast imaging as it requires high b-values (b ~ 1000-2000 s/mm^2), which inherently limits the SNR.

2.4.4 IVIM and perfusion

Perfusion of blood through the capillary beds is an incoherent biophysical process that closely resembles the Brownian diffusion of water in tissue. Intravoxel incoherent motion (IVIM) is another diffusion model that attempts to capture this perfusion along with the apparent diffusion coefficient. The simple monoexponential model in Equation 2.9 is extended to a biexponential fit to sum up the diffusion and perfusion components:

$$S(b) = S_0\big(f_{perf}\ \mathrm{e}^{-b(D^* + D_{blood})} + \big(1 - f_{perf}\big)e^{-b * D_{app}}\big) \qquad [2.11]$$

where f_{perf} is the fraction of blood that is flowing, D^* is the pseudodiffusion coefficient that describes the random blood flow across the capillary bed, D_{blood} describes the diffusion of water molecules in blood, and D_{app} is the diffusion coefficient within the tissue, like ADC (73). Note that the perfusion effects are prominent at low b-values and are observed to be negligible at higher b-values, as shown in Figure 2.12. Thus, a simplified way to fit Equation 2.11 is to separately fit two ranges of b-values, where both diffusion and perfusion effects are considered in the low range and only diffusion is

considered for higher b-values (i.e. Equation 2.9). In this way, diffusion and perfusion effects can be separated using fewer b-values.

Figure 2.12 – IVIM Model
The biexponential model accounts for perfusion (blue) and diffusion (green)

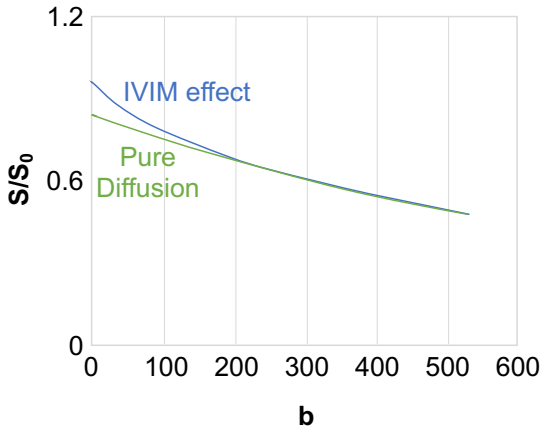

In its early stages, IVIM was investigated as a way to assess brain perfusion, which is related to brain function. However, the technical challenges of IVIM were limiting and the blood oxygen level dependent (BOLD) imaging became the leading method being that it was more reliable and sensitive (74). Currently, IVIM is used primarily in oncology to measure angiogenesis and heterogeneity of the microvasculature. IVIM is used throughout the literature for clinical applications including brain tumors and prostate, liver, and breast cancers.

In 2011, Sigmund et al. reported significant differences in IVIM parameters between normal fibroglandular tissue and malignant lesions. They also showed that the perfusion fraction may play a role in differentiating lesions subtypes. Since then, several groups have investigated the use of IVIM in breast cancer for diagnosis, treatment monitoring, predicting pCR, and prediction of prognostic factors (67).

2.5 DWI in Breast Cancer

Although it is widely accepted that CE-MRI is extremely sensitive to breast cancer, the specificity of CE-MRI is debated, which plays a role in the controversial use of MRI for breast cancer screening and staging as discussed above. Moreover, the safety of

gadolinium-based agents is not fully understood. Thus, it is desirable to establish an MRI method to use in place of or adjunct to CE-MRI. DWI has been widely suggested in research to fill this roll and increasingly used clinically. Low ADC values reflect high cell density and are associated with malignancies (75). Normal tissue is reported to have ADC values of 1.6–2.0 × 10^{-3} mm^2/s, while the mean ADC of malignant tumors has been measured between 0.87–1.36 × 10^{-3} mm^2/s and the optimal threshold for differentiation has been reported between 0.9 and 1.76 × 10^{-3} mm^2/s (68,76). Accordingly, when combined with CE-MRI, DWI may be a powerful tool for more informed decision-making prior to and during breast cancer treatment. Moreover, DWI has potential application in breast cancer screening as it may improve the speed, cost-effectiveness, and accuracy of the MRI exams (77).

2.5.1 DWI applications in breast imaging

Typically, a simple diffusion model is used for DWI in breast cancer to measure ADC maps. Many clinical studies have been performed to assess the usefulness of ADC in breast cancer applications from screening to monitoring treatment response. Though less common, more complex DWI measures have also been increasingly investigated, including synthetic ADC, DTI, DKI, IVIM, and others. Some studies also combined DWI with other radiomic features. Here, I'll present a brief overview of the literature and supporting evidence for DWI in breast cancer. See recent publications by Iima et al. (67) and Partridge et al. (78) for more detailed reviews.

Detection and characterization

The most widely used application of DWI in breast cancer is the use of ADC values to determine the malignancy of a lesion, which can help reduce false positives and thereby reduce unnecessary biopsies. In a meta-analysis of 13 studies by Chen et al., ADC was shown to have 84% sensitivity and 79% specificity distinguishing malignant and benign lesions (76). Another meta-analysis by Zhang et al. further showed that DWI can improve accuracy of MRI diagnosis when used in conjunction with CE-MRI (79). This increased accuracy can have important effects on negative biopsy rates; in a 2019 multicenter study

by Rahbar et al. ADC was found to reduce the biopsy rate by 20.9% without losing sensitivity (80).

Based on these results many groups have begun investigating the use of DWI for abbreviated and/or non-contrast screening protocols to greatly reduce the scan time and cost and potentially circumvent the risk of Gadolinium injection altogether. One major limitation of DWI is its low resolution, which greatly limits the sensitivity to small lesions in the screening setting. More research is also needed to understand the role of diffusion for non-mass-like lesions. most studies to date have been performed in mass-like lesions and others have found that ADC has limited accuracy in non-mass enhancing lesions (81).

Prognosis

As medicine becomes more personalized, it is important to determine characteristics that can guide the choice of treatments. Some literature suggests that ADC values may be able to determine tumor subtype. For example, many studies have shown that ADC is negatively correlated with higher proliferation (82–85). Others have found that DWI can help identify pre-invasive ductal carcinoma in situ (DCIS) (82,86), suggesting that DWI could have major clinical implications in the reduction of overtreatment of non-invasive cancers (78). Throughout the literature, associations have also been seen between ADC and expression of estrogen receptor (ER), progesterone receptor (PgR), and human epidermal growth factor receptor 2 (HER2) (67). However, the current results and attempts to correlate diffusion characteristics with histological phenotype are conflicting throughout the field. ADC values and other DWI metrics may serve as useful biomarkers, but significant research is still required before they are clinically relevant.

Another important prognostic factor for breast cancer patients is the status of the axillary lymph nodes. Current measures of the lymph nodes by CE-MRI are insufficient in distinguishing malignant from benign nodes. Thus, surgical staging, which often leads to edema and paresthesia, is required for accurate assessment. DWI may provide a non-invasive method to stage the nodes. A meta-analysis by Xing showed that lower ADC values were measured on metastatic nodes compared with high sensitivity (83%) and

specificity (82%) (87). Once again, other studies found conflicting conclusions, suggesting the need for further investigation.

Treatment response

Choosing the right systemic treatment for a breast cancer patient is critical, and it has been shown that patients who achieve pCR prior to surgery from systemic therapies have improved survival rates (88). Many recent studies have established DWI as a noninvasive and quantitative way to both predict response to treatment, as measured by pCR, and to monitor the post-treatment response. However, some studies have shown that these results are dependent on the tumor subtype and still others find contradictory results, causing lack of consensus at the current time (67).

2.5.2 Challenges of DWI in breast imaging

Despite significant advancement in DWI methods, especially in brain, and much academic evidence of the value of breast DWI, it is still rarely used clinically. For example, at the University of Minnesota, DWI is acquired for patients enrolled in I-SPY 2 according to the ACRIN 6698 protocol. However, even though the images are readily available to the breast radiologists, they are rarely read in the clinical setting. Anecdotally, one University of Minnesota radiologist said that DWI and ADC maps are not typically used in practice because they are so “crappy”. More rigorously, there are two important challenges that must be addressed prior to the adoption of DWI for clinical use: standardization and image quality.

In order for ADC to be useful as a quantitative measure it must be reproducible across scanners, sites, time, users, and patients. However, even as the name suggests, the *apparent* diffusion coefficient is strongly dependent upon the acquisition parameters used. Recall that sampling different b-values probes different types of diffusion, as explained in Section 2.4. Additionally, the b-value is defined based on the diffusion time and strength of the diffusion gradient. However, the same b-value can measure different scales of diffusion by changing the time. Another consideration is that the prescribed b-value can be different than the achieved weighting based on gradient and timing errors or diffusion weighting that is caused from other parts of the sequence. Gradient nonlinearity

also causes ADC bias, especially far from iso-center, that is spatially varying, system-specific. One group measured as much as ~25% bias in an ice water phantom around 15 cm from isocenter in the superior/inferior direction (89). Thus, is it important to use quality control across vendors, scanners, sites, etc.

On the processing side, ADC maps can be calculated with a wide range of fitting algorithms and denoising thresholding. These maps are often treated quite differently depending on the reader; some prefer to measure the ADC in the lowest region of the tumor, while others measure the whole tumor, while still others normalize the ADC compared to that of normal fibroglandular tissue. With such large variation, it is difficult to define a threshold that distinguishes malignant from benign tissue that is reliable across a large range of patients.

Fortunately, there is a strong effort in the research community to achieve standardization in quantitative imaging by bringing experts in the field together to form a consensus on optimal methods and guidelines. Some initiatives include the Radiological Society of North America's (RSNA) Quantitative Imaging Biomarkers Alliance (QIBA), the National Cancer Institute's (NCI) Quantitative Imaging Network (QIN), and the European Society of Breast Radiology (EUSOBI). For example, EUSOBI recently published breast recommendations in [Ref (90)], covering acquisition parameters (b-value specifications, fat saturation methods, resolution, TR, TE), ROI placement, and quality assurance. Other groups are developing methods for measuring ADC bias and robust quality assurance, like using a temperature-controlled ice water phantom (91).

Another major challenge of clinical breast DWI is the poor image quality of current methods. DWI is typically acquired using a standard SE-EPI sequence. While this standard approach performs sufficiently in brain imaging, bilateral breast DWI with full coverage can be much more challenging. Good B_0 shimming is especially difficult outside of isocenter and respiratory motion throughout the scan causes a dynamic change in the B_0 field. The large FOV requires a high sampling frequency in the PE direction (usually Left/Right in axial images), which causes geometric distortion and blurring in PE. Low inherent SNR, T_2^* decay, and long scan times limit the resolution achievable. Breast anatomy is very heterogeneous and often contains a large adipose signal,

demanding for robust fat suppression and causing a large chemical shift artifact. Finally, poor Nyquist ghost correction leaves residual ghosting artifacts that disrupt image interpretation and can bias ADC measurements.

The ACRIN 6698 protocol reasonably represents high-quality, clinically available breast DWI. Acquired in 4-6 minutes, the study requires resolution of 1.7-2.8 mm x 1.7-2.8 mm x 4-5 mm, which is further blurred in the PE direction from dephasing. Compare to a typical CE-MRI acquisition, the key sequence of breast imaging, that is acquired at $\leq$1.4 mm x $\leq$1.4 mm x $\leq$ 2.5 mm (0.6 mm x 0.6 mm x 1.3 mm at our site). Of course, on this low-resolution DWI some small lesions will be undetectable, partial volume effects will add bias to ADC measurements, and other useful clues (e.g. spiculated borders) will be indiscernible.

One example of this DWI is shown in Figure 2.4, which highlights large geometric distortion, chemical shift artifact, residual Nyquist ghosts, and low resolution. While this case is admittedly cherry-picked for demonstration purposes, each of these artifacts are commonly observed in typical breast DWI. Technical improvements of breast DWI are very important for successful clinical integration. Two of these, Nyquist ghost correction and spatial resolution, will be addressed in the chapters to come.

Chapter 3: Understanding the Nyquist Ghost

Nyquist ghosts are a phenomenon of EPI imaging that arise in the image due to the back and forth nature of the readout train. Eddy currents, timing errors, and imperfect gradients can cause inconsistencies between the forward and reverse RO lines (RO+ and RO-). This manifests in the image as a replica of the object that falls at ½ of the FOV. Here, I will assume a simple linear model of a Nyquist ghost and derive the representation of the artifact in image space. Note that this derivation is meant to provide intuition to understand the connection between the Nyquist ghost in image space and k-space. For simplicity, the $RECT(\quad)$ finite sampling window of k-space will be ignored, and the continuous and discrete Fourier transforms will be used jointly.

3.1 The Ghost Model

3.1.1 The linear ghost

The first assumption of Nyquist ghost is that the error affects every other line equally and oppositely. Thus, we will start with the signal equation and a comb operator (III) to separate out the RO+ and RO- lines from k-space:

$$\begin{aligned} m(x,y) = FT^{-1}\left\{\mathrm{III}_{2\Delta k_y}(k_y)M(k_x,k_y)\right\} \\ + FT^{-1}\left\{\mathrm{III}_{2\Delta k_y}(k_y-\Delta k_y)M(k_x,k_y)\right\} \end{aligned} \quad [3.1]$$

where $m(x,y)$ is the signal in the image domain, FT^{-1} represents the inverse Fourier transform, and $M(k_x,k_y)$ represents the signal in k-space that is sampled at $\Delta k_x = \frac{1}{FOV_x}$ and $\Delta k_y = \frac{1}{FOV_y}$ to satisfy the Nyquist sampling criteria. The comb operator has a period of $2\Delta k_y$ and can be written as: $\mathrm{III}_{2\Delta k_y}(k_y) = \frac{1}{2\Delta k_y}\mathrm{III}\left(\frac{k_y}{2\Delta k_y}\right)$. Thus,

$$\begin{aligned} m(x,y) = FT^{-1}\left\{\frac{1}{2\Delta k_y}\mathrm{III}\left(\frac{k_y}{2\Delta k_y}\right)M(k_x,k_y)\right\} \\ + FT^{-1}\left\{\frac{1}{2\Delta k_y}\mathrm{III}\left(\frac{k_y-\Delta k_y}{2\Delta k_y}\right)M(k_x,k_y)\right\} \end{aligned} \quad [3.2]$$

A typical Nyquist ghost can be modeled as a first-order phase offset between RO+ and RO- lines of k-space, which are acquired with positive and negative gradients in x, respectively, as shown in Figure 3.1. Assume that the odd lines of k-space are perturbed by a phase offset $(-\phi)$ and shifted in k_x by $(-\kappa)$; oppositely the even lines are modified by $+\phi$ and $+\kappa$. The signal equation can then be written as:

$$\begin{aligned} m'(x,y) = FT^{-1}\left\{\frac{1}{2\Delta k_y}\,\mathrm{III}\left(\frac{k_y}{2\Delta k_y}\right)M\big(k_x-\kappa,k_y\big)e^{+i\phi}\right\} \\ + FT^{-1}\left\{\frac{1}{2\Delta k_y}\,\mathrm{III}\left(\frac{k_y-\Delta k_y}{2\Delta k_y}\right)M\big(k_x+\kappa,k_y\big)e^{-i\phi}\right\} \end{aligned} \quad [3.3]$$

For simplicity, consider the equation in two parts, evens and odds. First, consider the even RO lines:

$$\begin{aligned} FT^{-1}\left\{\frac{1}{2\Delta k_y}\,\mathrm{III}\left(\frac{k_y}{2\Delta k_y}\right)M\big(k_x-\kappa,k_y\big)e^{+i\phi}\right\} \\ = FT^{-1}\left\{\frac{1}{2\Delta k_y}\,\mathrm{III}\left(\frac{k_y}{2\Delta k_y}\right)\right\} * FT^{-1}\big\{M\big(k_x-\kappa,k_y\big)e^{+i\phi}\big\} \end{aligned} \quad [3.4]$$

where the Fourier transform of the comb function with period T is defined as $FT^{-1}\{\mathrm{III}_{\mathrm{T}}(k)\} = \frac{1}{T}\mathrm{III}_{\frac{1}{\mathrm{T}}}(\mathrm{y})$ such that $FT^{-1}\left\{\frac{1}{2\Delta k_y}\,\mathrm{III}\left(\frac{k_y}{2\Delta k_y}\right)\right\} = \mathrm{III}\left(\frac{y}{\frac{1}{2\Delta k_y}}\right)$ and $\frac{1}{\Delta k_y} = FOV_y$.

Thus, the righthand side becomes

$$\begin{aligned} = e^{+i\phi}e^{2\pi i\kappa x}m(x,y) * \mathrm{III}\left(\frac{y}{\frac{FOV_y}{2}}\right) \\ = e^{i(2\pi\kappa x+\phi)}\int m(x,y-\tau)\sum_{n=-\infty}^{\infty}\delta\left(\tau-\frac{FOV_y}{2}n\right)d\tau \\ = \sum_{n=-\infty}^{\infty} m\left(x,y-\frac{FOV_y}{2}n\right)e^{i(2\pi\kappa x+\phi)} \end{aligned} \quad [3.5]$$

Now consider the odd RO lines:

$$
\begin{aligned}
&FT^{-1}\left\{\frac{1}{2\Delta k_y}\mathrm{III}\left(\frac{k_y-\Delta k_y}{2\Delta k_y}\right)M\big(k_x+\kappa,k_y\big)e^{-i\phi}\right\}\\
&\qquad=FT^{-1}\big\{M\big(k_x+\kappa,k_y\big)e^{-i\phi}\big\}*FT^{-1}\left\{\frac{1}{2\Delta k_y}\mathrm{III}\left(\frac{k_y-\Delta k_y}{2\Delta k_y}\right)\right\}\\
&\qquad=FT^{-1}\big\{M\big(k_x+\kappa,k_y\big)e^{-i\phi}\big\}*FT^{-1}\left\{\frac{1}{2\Delta k_y}\mathrm{III}\left(\frac{k_y}{2\Delta k_y}\right)\right\}e^{2\pi i\Delta k_y y}\\
&\qquad=e^{-i(2\pi\kappa x+\phi)}m(x,y)*\sum_{n=-\infty}^{\infty}\delta\left(y-\tfrac{FOV_y}{2}n\right)e^{2\pi i\Delta k_y y}\\
&\qquad=e^{-i(2\pi\kappa x+\phi)}\int_{-\infty}^{\infty}m(x,y-\tau)\sum_{n=-\infty}^{\infty}\delta\left(\tau-\tfrac{FOV_y}{2}n\right)e^{2\pi i\Delta k_y\tau}\,d\tau\\
&\qquad=e^{-i(2\pi\kappa x+\phi)}\sum_{n=-\infty}^{\infty}m\left(x,y-\tfrac{FOV_y}{2}n\right)e^{2\pi i\Delta k_y\frac{FOV_y}{2}n}\\
&\qquad=e^{-i(2\pi\kappa x+\phi)}\sum_{n=-\infty}^{\infty}m\left(x,y-\tfrac{FOV_y}{2}n\right)e^{i\pi n}\\
&\qquad=\sum_{n=-\infty}^{\infty}m\left(x,y-\tfrac{FOV_y}{2}n\right)e^{i(-2\pi\kappa x-\phi+\pi n)}
\end{aligned}
\qquad [3.6]
$$

Now add the even and odd lines back together:

$$
\begin{aligned}
m'(x,y)=&\sum_{n=-\infty}^{\infty}m\left(x,y-\tfrac{FOV_y}{2}n\right)e^{i(2\pi\kappa x+\phi)}\\
&+\sum_{n=-\infty}^{\infty}m\left(x,y-\tfrac{FOV_y}{2}n\right)e^{i(\pi n-2\pi\kappa x-\phi)}\\
&=\sum_{n=-\infty}^{\infty}m\left(x,y-\tfrac{FOV_y}{2}n\right)\left(e^{i(2\pi\kappa x+\phi)}+\ e^{i(\pi n-2\pi\kappa x-\phi)}\right)\\
&=\sum_{n=-\infty}^{\infty}m\left(x,y-\tfrac{FOV_y}{2}n\right)(\cos(2\pi\kappa x+\phi)\\
&+i\sin(2\pi\kappa x+\phi)+\cos(\pi n-2\pi\kappa x-\phi)\\
&+i\sin(\pi n-2\pi\kappa x-\phi))
\end{aligned}
\qquad [3.7]
$$

Now consider the sum n for $-\infty$ to ∞. When n is even, $\cos(\pi n - 2\pi\kappa x - \phi) = \cos(2\pi\kappa x + \phi)$ and $i\sin(\pi n - 2\pi\kappa x - \phi) = -i\sin(2\pi\kappa x + \phi)$. When n is odd, $\cos(\pi n - 2\pi\kappa x - \phi) = -\cos(-2\pi\kappa x + \phi)$ and $i\sin(\pi n - 2\pi\kappa x - \phi) = i\sin(-2\pi\kappa x - \phi)$. Thus,

$$\begin{aligned} m'(x,y) = \sum_{n\ even} & m\left(x, y - \tfrac{FOV_y}{2}n\right)(\cos(2\pi\kappa x + \phi) \\ & + i\sin(2\pi\kappa x + \phi) + \cos(2\pi\kappa x + \phi) - i\sin(2\pi\kappa x - \phi)) \\ & + \sum_{n\ odd} m\left(x, y - \tfrac{FOV_y}{2}n\right)(\cos(2\pi\kappa x + \phi) \\ & + i\sin(2\pi\kappa x + \phi) - \cos(2\pi\kappa x + \phi) + i\sin(2\pi\kappa x - \phi)) \\ & = \sum_{n\ even} m\left(x, y - \tfrac{FOV_y}{2}n\right) 2\cos(2\pi\kappa x + \phi) \\ & + \sum_{n\ odd} m\left(x, y - \tfrac{FOV_y}{2}n\right) 2i\sin(2\pi\kappa x + \phi) \end{aligned} \quad [3.8]$$

and due to the cyclic nature of the FOV and ignoring the scaling factor due to the lack of windowing, we can simplify this as:

$$m'(x,y) = m(x,y)\cos(2\pi\kappa x + \phi) + m\left(x, y \pm \tfrac{FOV_y}{2}\right) i\sin(2\pi\kappa x + \phi) \quad [3.9]$$

Equation 3.9 shows that there will be an object in its correct position but it will have a signal modulation dependent on $\cos(2\pi\kappa x + \phi)$ and that there will be an imaginary ghost that falls at $\frac{FOV_y}{2}$ and is modulated by $\sin(2\pi\kappa x + \phi)$. Notice that the ghost-free image corresponds to when $\kappa = \phi = 0$; as expected, Equation 3.9 becomes

$$m'(x,y) = m(x,y)\cos(0) + m\left(x, y \pm \tfrac{FOV_y}{2}\right) i\sin(0) = m(x,y) \quad [3.10]$$

The derivation of Equation 3.9 assumes that k-space is fully sampled. In the case of accelerated acquisitions with undersampling factor R, Equation 3.9 becomes less straightforward; the unaliased and reconstructed image will contain multiple replicas (m_{ghost}) of the object (m_{object}) at locations given by

$$m_{ghost}(x,y) = \sum_{j=0}^{R-1} m_{object}\left(x, y \pm \frac{(2j+1)FOV_y}{2R}\right) \quad [3.11]$$

These ghosts will have an additional spatially dependent signal modulation that depends on the sensitivity profiles. For example, for an acquisition with $R = 3$ undersampling, the ghost will appear shifted by $\frac{1}{6}FOV_y$, $\frac{3}{6}FOV_y$, and $\frac{5}{6}FOV_y$ relative to the object.

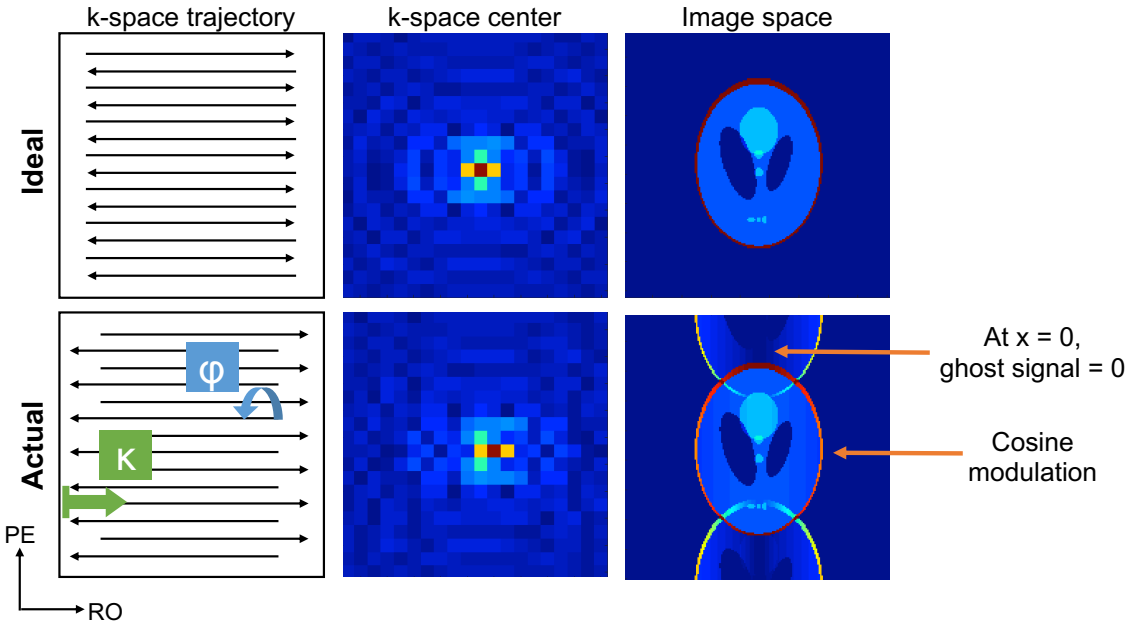

Figure 3.1 – First order Nyquist ghost
Nyquist ghosts can be modeled as a shift in k_{RO} (κ) and a phase offset (ϕ) between RO+ and RO- lines. A Nyquist ghost is simulated with κ = 1 and ϕ = 0. The signal intensity of the ghost is modulated in x by sin($2\pi\kappa x$), which causes a signal null at x = 0. The object is modulated by cos($2\pi\kappa x$); see Equation 3.3.

3.1.2 The 2-dimensional ghost

While a 1-dimensional linear ghost is caused by shift in the RO lines of k-space in k_x, there can also be slight differences in k_y, which causes a 2D ghost, or sometimes called an oblique ghost. We can describe this as a shift in k_y that we will call λ. Similarly, the ghosted image can be described as:

$$m'(x,y) = FT^{-1}\left\{2\Delta k_y \mathrm{III}\left(\frac{k_y}{2\Delta k_y}\right) M\left(k_x - \kappa, k_y - \lambda\right) e^{-i\phi}\right\} + FT^{-1}\left\{2\Delta k_y \mathrm{III}\left(\frac{k_y - \Delta k_y}{2\Delta k_y}\right) M\left(k_x + \kappa, k_y + \lambda\right) e^{+i\phi}\right\} \quad [3.12]$$

Following the same derivation given above, the 2D ghost can be described in image space as:

$$m'(x,y) = m(x,y)\cos(2\pi\kappa x + 2\pi\lambda y + \phi) + m\left(x, y \pm \frac{FOV_y}{2}\right) i \sin\left(2\pi\kappa x + 2\pi\lambda y + \phi - \lambda\frac{FOV_y}{2}\right) \quad [3.13]$$

Figure 3.2 demonstrates a shift in k_y, simulating the effect in image space as this equation predicts. Notice that in the case where $\lambda = 0$, Equation 3.13 simplifies to Equation 3.9 describing a linear ghost.

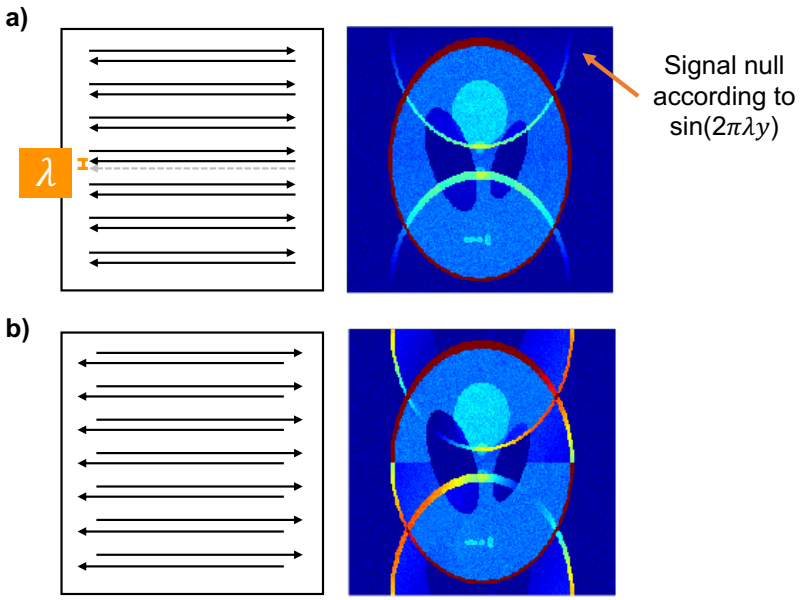

Figure 3.2 – The oblique ghost
An oblique, or 2D, ghost can be caused by a shift in k_y between the RO+ and RO- lines, as shown exaggerated in (a). Shifts in k_x and k_y can occur simultaneously (b). The Shepp-Logan was simulated with the following parameters: a) $\phi = 0, \kappa = 0, \lambda = 0.3$ and b) $\phi = 0, \kappa = 0.6, \lambda = 0.3$, where ϕ is a 0th order phase offset [radians], κ is a 1st order shift in k_x [units Δk_x], and λ is a 1st order shift in k_y [units Δk_y]. The ghost always falls at FOV/2 in the PE direction. In an oblique ghost there is an additional signal modulation in y of $\sin(2\pi\lambda y)$ in the ghost and $(2\pi\lambda y)$ in the object. See Equation 3.7.

3.2 Ghost Correction Methods throughout Literature

3.2.1 The three-line navigator

Based on the linear model of Nyquist ghosts, the most common correction of ghosts uses a three-line navigator. As the name suggests, the three-line navigator samples three RO lines in the center of k_y before every acquisition. The first and third lines (RO+) are averaged together to reduce the effect from B_0 inhomogeneity. The RO- and averaged RO+ lines are Fourier Transformed in the RO direction and the phase is compared between the two in hybrid k_y-x space. The phase difference is fit to a line, where the slope is κ and the intercept is ϕ, as shown in Figure 3.3.

Figure 3.3 – The three-line navigator
The phase difference between RO+ and RO- is fit to a line. The 1st order correction is applied in k_y-x space.

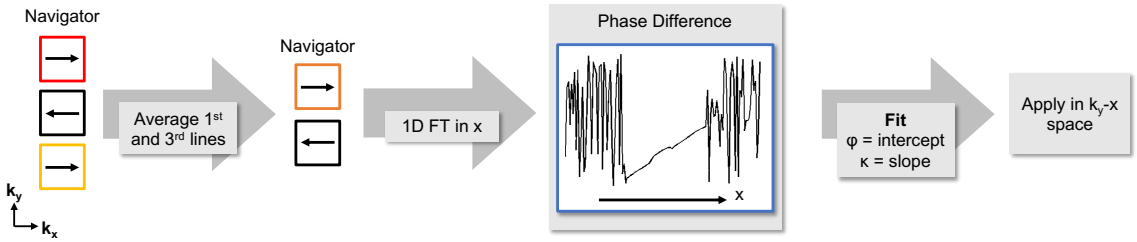

Base on Maier JK, Vavrek RM, Glover GH. US Patents 5,151,656.1992

While this navigator approach performs well in brain imaging, it often fails in breast DWI because of residual fat signal, respiration, lower SNR for fitting, and bigger B_0 inhomogeneity. Figure 3.4 shows an example of a mild ghost failure that is typical in breast DWI acquired with the ACRIN 6698 protocol and reconstructed online. Notice how even a small ghost in the source images can have significant affect in the ADC map, which inhibits the interpretation of the ADC map and can bias the ADC values in the lesion depending on its location.

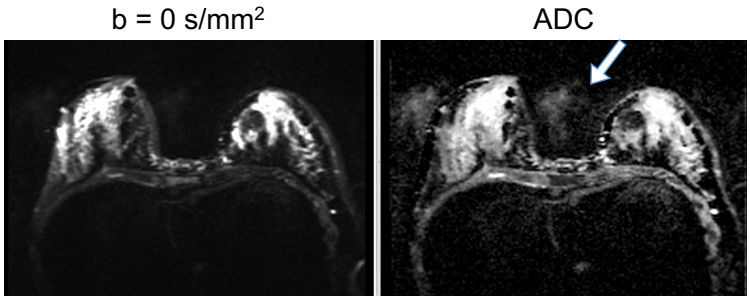

Figure 3.4 – Nyquist ghost in breast DWI
An example of a small residual ghost, typical in breast DWI (ACRIN 6698) after 3-line navigator correction. Small ghosts in source images (left) can greatly affect the ADC map.

3.2.2 The full phase navigator

The linear 3-line navigator assumes that the Nyquist ghost is caused by a phase difference between the positive and negative RO lines that it constant over the whole RO train. However, one potential source of Nyquist ghosts is eddy currents, which are time varying and may change drastically or even die out completely over the course of the readout. Similar to the model used with the three-line navigator described above, the full phase navigator is based on the assumption that the phase difference between any two subsequent lines of k-space can be described as a shift in k_x (κ) and a phase offset (ϕ). However, the model is relaxed to account for a time-varying component of this linear ghost caused by time-dependent eddy currents.

The full phase navigator is measured as a separate acquisition that is a replica of the typical pulse sequence modified to disable the phase encoding blips, thus repeating the navigator throughout the whole RO train. Then every RO+ line is compared to the average of the two RO- lines on either side of it. This phase difference is fit to a linear model, as described above, and corrected in the subsequent acquisitions, assuming that the eddy currents caused by the pulse sequence are reproducible.

While the full phase navigator can more accurately correct for time varying ghosts, it is associated with some disadvantages. First, T_2^* decay causes signal loss throughout the readout train, which may lead to insufficient SNR to measure the phase offset later in the readout. Second, acquiring a full navigator is time consuming, which can cause a large increase in scan time. One may choose to acquire just a single navigator to avoid lengthening the scan time too much, but this additionally assumes that the phase error is not dependent on diffusion gradients and does not vary over the course of the scan from respiration or scanner drift.

3.2.3 Phase mapping approaches

Based on the Fourier relationship between k-space and image space, the inconsistencies between the even and odd lines of k-space correspond to phase differences between an image based on the even echoes compared to an image based on the odd echoes. In fact, the navigator approach measures the phase difference in the 1D image space, assuming it is constant through k_y. If the ghost is caused by inconsistencies in k_x and k_y, this phase difference can be described by a 2D surface, rather than a line. Thus, many ghost correction methods measure this phase difference in x-y image space, which requires fully sampled k-space with RO+ and fully sampled k-space with RO-, or other tricks to circumvent aliasing. Several strategies to acquire this reference data have been proposed throughout literature.

In one method by Chen and Wyrwicz (92), two reference scans are acquired without diffusion weighting: one is a typical fully sampled acquisition, the other contains one additional PE blip that effectively reverses the RO polarity of each line. These two reference sets are stitched together in a way to create RO+ and RO- only images, whose phase is compared to create a 2D phase map in image space that represents the difference in phase between RO+ and RO-. The inverse of this phase map can be directly applied to the RO+ lines in subsequent acquisitions or first fit to a model, like Equation 3.13 or even higher order if needed.

Another way to obtain a 2D phase map is to fully sample k-space with double FOV, proposed by Zur and extended by Xu et al. In this case, the RO+ and RO- echoes can be separated to provide RO+ and RO- images without aliasing (Figure 3.5). Again, their phases are compared as described above (93,94). One disadvantage with this approach is that the echo spacing is doubled in the reference acquisition, thus the geometric distortion will be unmatched in the phase map compared to the data itself.

Figure 3.5 – Nyquist ghost correction by 2D phase mapping
Double FOV is used to obtain one RO+ and one RO- image without aliasing. In this case, the phase map can be well-described by a linear phase in x, which corresponds to κ and ϕ.

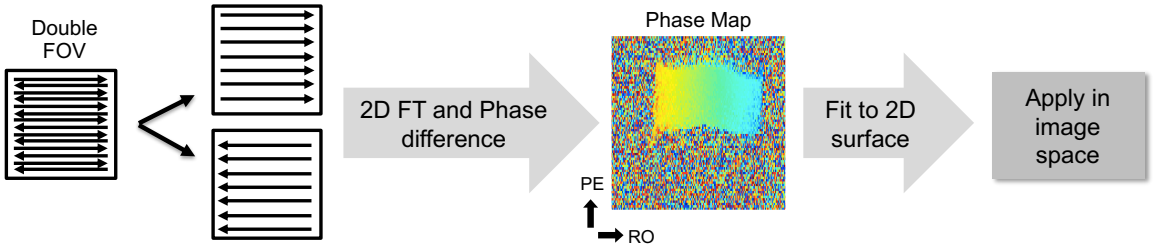

3.2.4 Phase cancellation

Phase labeling for additional coordinate encoding (PLACE) can be used for both geometric distortion and/or Nyquist ghost correction (95). In PLACE, data is acquired two or three times: the first image (I_0) adheres to the normal encoding strategy, while the additional images (I_{+d} and I_{-d}) are modified by an additional PE blip of area $\pm d$, where d corresponds to one step in k_{PE}. One of the additional images is used for Nyquist ghost correction; the ghost in I_0 will have opposite phase compared with that of I_{+d}, so that complex additions will cause cancellation of ghosts and yield ghost-free images. The third acquisition I_{-d}, can be used for distortion correction. Based on the Fourier shift theorem, in image space, the phases of I_0 and I_{-d} differ by a phase ramp that is exactly linear in the PE direction in an ideal B_0. However, in the presence of inhomogeneity, the nonlinearity of the phase difference corresponds directly to the distortion experienced by a given pixel.

An easy alternative to PLACE that is based on the same concept is RO-reversal. In this case the full acquisition is simply repeated with reversed RO polarities. Complex addition of these two data sets will cancel out static ghosts (Figure 3.6). Either PLACE or RO-reversal requires a large increase in scan time, as a second acquisition of the full data is required.

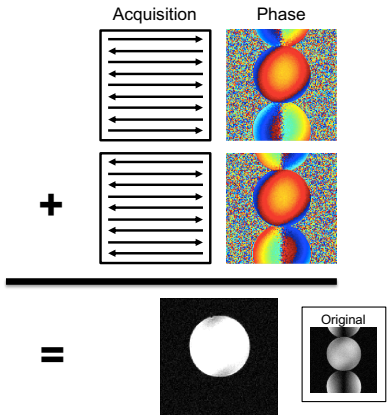

Figure 3.6 – Nyquist ghost phase cancellation
Assuming the phase difference between RO+ and RO- is reproducible across scans, the phase is equal and opposite when the RO direction is reversed.

3.2.5 Parallel imaging-based methods

As coil sensitivity profiles can be used to infer imaging data, they can also be used to measure spatially varying phase differences between the positive and negative RO lines in a variety of ways. The major PI-based methods are PAGE, EPI-GESTE, and DPG, described below.

Phased array ghost estimation (PAGE)

Phased array ghost estimation (PAGE), proposed in 2006 by Kellman and McVeigh, separates the even and odd echoes to obtain two sets of data with R = 2 undersampling (96). Then, SENSE is employed to reconstruct each set, forming two ghost-free images These two images can simply be incoherently added using a sum of squares, but this causes a reduction in SNR due to additive noise. Instead, the individual images are weighted by their point spread function and coherently combined using a complex weighted sum.

PAGE was extended to real-time PAGE by Kim et al., in which the reference data is no longer acquired. Instead, the RO polarity is reversed for every other timepoint (97). Interleaving two consecutive sets provides a fully sampled k-space that can be used for PI calibration.

EPI Nyquist ghost elimination via spatial and temporal encoding (GESTE)

Real-time PAGE was further extended by Hoge et al. to form EPI Nyquist ghost elimination via spatial and temporal encoding (GESTE), which follows the PAGE procedure but also includes an aspect of the PLACE method (98). A single acquisition is deinterleaved to produce RO+ and RO- data with R = 2 undersampling. Again, PI is used to fill in the unacquired lines in each set. However, in this case the PI is calibrated on a PLACE recon from two consecutive scans with opposite RO polarity. The two reconstructed sets are then combined coherently to cancel out residual ghosts.

Both GESTE and real-time PAGE maintain the temporal footprint of the acquired data, compared to PLACE and PAGE that combine contrasts acquired from two separate timepoints in the final acquisition. One major disadvantage of these methods is their incompatibility with typical PI for acceleration. In both PAGE and GESTE, deinterleaved images require R = 2 undersampling to reconstruct fully sampled RO+ and RO- acquisitions, which limits the amount of undersampling that can be used in the acquisition.

Dual-polarity GRAPPA (DPG)

Dual-polarity GRAPPA (DGP), proposed by Hoge and Polimeni, combines EPI ghost correction with GRAPPA unaliasing and uses the GRAPPA reconstruction to correct non-linear ghosts (99). In standard GRAPPA, the kernel is considered shift-invariant, meaning that a single kernel can be used for the entirety of k-space. Thus, GRAPPA is described as: $\hat{k} = wk$, where $\hat{k}$ is the reconstructed full k-space, k represents measured data, and w contains the weights that map the acquired data to the undersampled lines.

In DPG, the conventional GRAPPA reconstruction is slightly modified to estimate two separate kernels that are unique to the polarity of the RO lines involved. In other words, one set of weights, w, is applied to RO+ lines, and another, v, is applied to RO- lines: $\hat{k} = wk_{-} + vk_{+}$. In this case $\hat{k}$ is the estimated ghost-free data that is synthesized despite having been acquired. The weights w and v are estimated based on two sets of reference data; one, a full ghost-free acquisition and the other is a typical ghosted EPI acquisition. This reference data is one disadvantage of DPG; for robust ghost correction a clean reference set is required. Moreover, the ghosting artifact must be

consistent between the reference data and the subsequent acquisition. One advantage of DPG is that it can readily be extended to accelerated data, although it does require a larger number of weight sets that are consistent with the RO polarities.

3.2.6 Referenceless methods

Another class of methods, referenceless methods, uses some defined metric to quantify the level of ghost to solve an optimization over the 0th (ϕ) and 1st (κ) order ghost parameters to minimize the ghost intensity. Several measures have been defined throughout the literature that serve as cost functions ($f_{cost}(\phi, \kappa)$) in the minimization. Clare proposed a heuristic cost function as the image entropy in the spatial domain (100,101). Another, proposed by Peterson et al., is based on a singular value decomposition (SVD) of k-space after rearranging into GRAPPA-like kernels (102). Others use summation over the image space of manually drawn ROIs or certain regions of the image defined by the FOV (103).

Referenceless methods may be advantageous because they are based on the imaging data itself and do not require any additional navigator or reference data, which could allow for decreased acquisition time and/or shortened TE. Furthermore, they are easily integrated into any acquisition strategy and can be applied to retrospective data. They are not strictly limited by in-plane acceleration and SMS because they do not rely on any coil sensitivity data (33,36,104,105); however, previous reports have suggested that the image-space-based referenceless methods may be limited by aliasing (100,102). As a data-driven correction, referenceless methods may also be limited by signal intensity, deteriorating for low SNR acquisitions like high b-value or high-resolution scans.

3.3 Characterization of the Nyquist ghost in breast DWI: Preliminary Studies

Many advanced ghost correction methods proposed throughout the literature are based on the assumptions that a linear, time-invariant model is insufficient for describing the phase error. For example, phase mapping methods (Section 3.2.3) assume a 2D phase error that

varies over x-y space, PI-based methods (Section 3.2.5) circumvent using a model altogether and therefore account for nonlinearities, and full phase navigators (Section 3.2.2) measure a time-varying phase error. Thus, it is important to characterize the ghosting artifact in order to reduce the residual ghost. In this work, several phantom and *in vivo* studies were conducted under various conditions to measure and understand the Nyquist ghost that arises in breast DWI acquisitions.

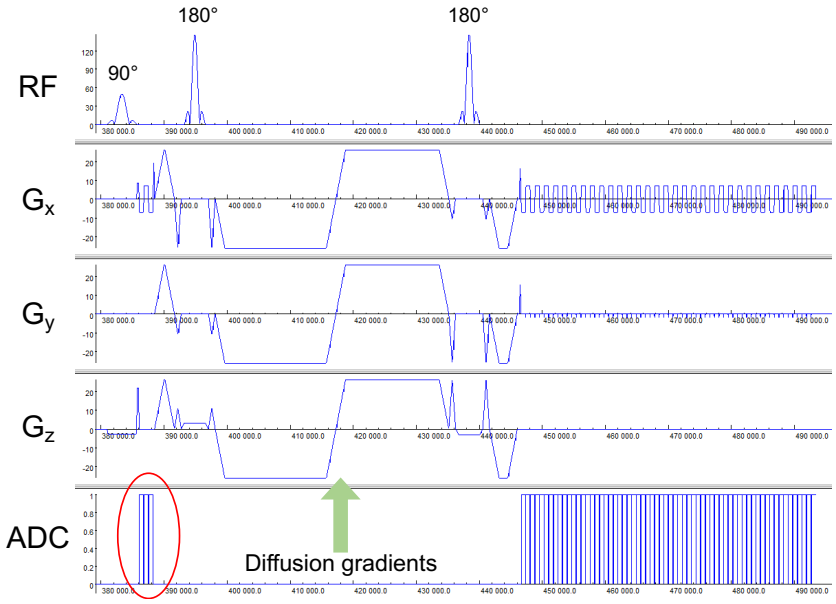

Figure 3.7 – DWI pulse sequence example
The three-line navigator (circled in red) is acquired prior to the diffusion gradients (bipolar diffusion shown).

3.3.1 Performance of three-line and full-phase navigators

The three-line navigator is typically acquired prior to the acquisition and prior to the diffusion weighted gradients, as shown in Figure 3.7. Thus, each acquisition is associated with a unique navigator that is acquired a short time before it, including each reference scan, slice, b-value, and average. Note, however, that the 3-line navigator does not include effects from diffusion weighting gradients. For example, in the ACRIN 6698 DWI protocol, there are about 60 ms between the navigator and the beginning of the echo, or a ~80-90 ms delay until the center of the echo. It is also independent across coils, as the ghost parameters may be spatially varying or depend on time delays in the hardware. By carefully examining the three-line navigator and comparing it to the full-

phase navigator, we will characterize the slice-, coil-, and time dependence of the ghost, making the assumption that it can be reasonably described by a linear phase error in k_x-y space.

Experiment 1 – Sensitivity to B_0 Inhomogeneity

The purpose of this experiment was to determine how B_0 inhomogeneity and off resonance affect the 3-line navigator. Several shimming conditions were used to simulate B_0 inhomogeneity and the resonance frequency was shifted to simulate off resonance.

Methods: A cylindrical saline phantom was scanned at iso-center with a 2-channel head coil for a single slice using standard SE-EPI DWI for a single repetition of b = 0 s/mm^2. In the control case, interactive, static shimming was used to optimize B_0 homogeneity. The experiment was repeated with various alterations from the optimized shimming solution to simulate poor shimming or a change in the field between shimming and scanning. The shimming parameters were changed from the control case as follows: 1) modified shim in X of 10 μT/m, 2) modified shim in Y of 10 μT/m, and 3) modified X^2Y^2 shim of 189 μT/m^2. Finally, the scan was repeated with optimal shimming and a shift in the center frequency of +100 Hz to represent a constant off resonance, similar to that of adipose signal. A three-line navigator was acquired with each and the phase difference was plotted for three different combinations, including the phase between lines 1 and 2, lines 3 and 2, and the average of lines 1 and 3 with line 2.

Results: The effect of poor shimming is evident in the image domain, as shown in Figure 3.8. The distortion occurs in the PE direction, as expected, because of the phase accrual over the echo train in k_y. Notice that the amount of shift in y is dependent on the shimming parameter. For example, with inhomogeneity in X, the shift is to the left for x > FOV/2 and to the right for x < FOV/2. With Y inhomogeneity, the magnitude of the shift in y depends on the y position (i.e. more at the edges of the phantom as they are farther from y = FOV/2. In the X^2Y^2 case, the distortion depends on the position in both x and y.

Figure 3.8 – Effect of B_0 on 3-line navigator
The effect of shimming is shown in the image domain (left) compared to a true circle (white line). Distortion occurs in y with magnitude dependent on the direction of B_0 shimming. The effect on the navigator phase (center) is zoomed (right) to show that averaging the 1st and 3rd lines (red) of the 3-line navigator accounts for inhomogeneity in x.

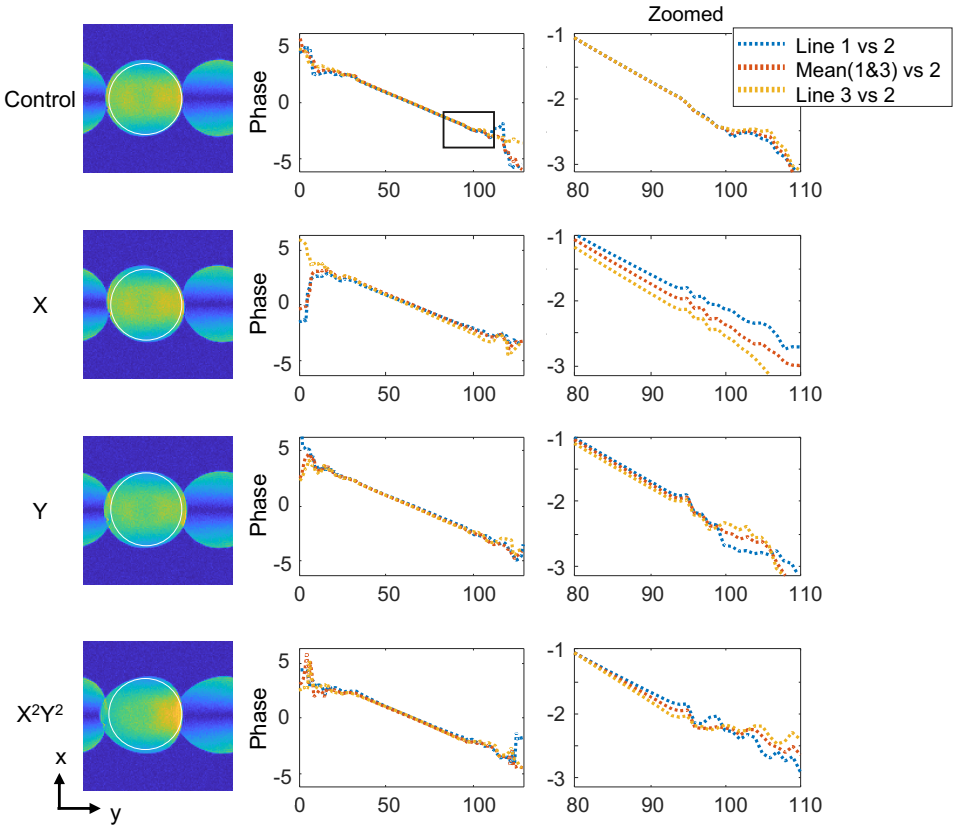

The phase differences measured in three different ways are shown in Figure 3.8, which shows the effect of poor shimming. When the B_0 field is homogeneous, as in the control case, the 3-line navigator (averaging the 1st and 3rd lines) is equivalent to the 2-line navigator (using either line 1 or 3). However, in the case of poor shimming in x, the navigator estimated different ghost correction depending on what lines are used, as evident in the zoomed part of Figure 3.8 (right). While all three had similar slopes, the 0-order phase offset (ϕ) shifted as the phase accrued through the echo-train. Averaging lines 1 and 3 together gave some average ϕ estimate. Poor shimming in the y-direction did not affect the navigator because the navigator represents a projection through the y

direction. This effect was much larger when the off resonance is 100 Hz, as shown in Figure 3.9. Furthermore, the 0th order phase offset is much larger than that measured on resonance even after accounting for the phase accrual by averaging RO+ navigator lines 1 and 3.

Figure 3.9 – Off resonance effect on 3-line navigator
With 100 Hz off resonance, the navigator experiences a large phase shift despite averaging over lines 1 and 3 (red), possibly due to phase wrapping. Compare to control in Figure 3.8.

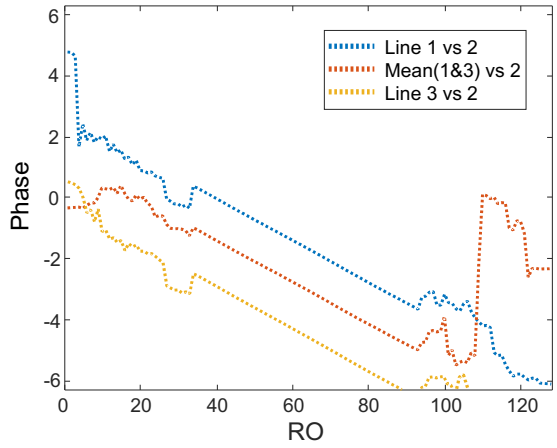

Discussion: In breast DWI, even with the use of high order B_0 shimming, geometric distortions are often greater than those shown in Figure 3.8, especially around the nipple. Thus, Figure 3.8 highlights the importance of the 3-line navigator compared to a 2-line navigator. Inhomogeneity in X causes phase to accumulate between the two lines that is not caused by the even/odd nature of the echo train but is consistent along the whole acquisition. In this case, the averaging over the 1st and 3rd lines canceled out this phase accrual, i.e. simulated the measurement of the RO+ line at the same time that line 2 (RO-) was measured. However, this assumes that the inhomogeneity is static throughout the scan and the navigator, which is not always the case, especially with respiratory motion and eddy currents.

Considering off-resonance, we chose 100 Hz, which is about 1/4th the frequency separation between water and the resonance peaks of adipose signal at 3 T. This magnitude of off resonance caused a large shift in ϕ, likely caused by phase wrap. Moreover, in this experiment the off resonance was constant in space; in reality, the fat

signal will occur throughout space in various amounts, which may add discontinuities to the phase measurement in the RO direction. Due to the projection nature of the navigator in the y direction, the water and fat signal will mix together across the PE direction potentially causing nonlinearities dependent on the magnitudes of each signal. This is further demonstrated in Experiment 3 below.

Conclusion: It is important to combine lines 1 and 3 of the three-line navigator in order to account for B_0 inhomogeneity in x. Inhomogeneity that is not corrected for may cause a small shift in ϕ. A large frequency offset may lead to a large phase shift in the navigator estimation.

Experiment 2 – the effects of slice, coil, and breathing

The purpose of this experiment was to understand how variable RO+/RO- phase differences are across coils, slices, and repetitions with and without simulated breathing. A case of navigator failure was closely examined.

Methods: The CaliberMRI breast phantom (model 131) was scanned axially using a standard SE-EPI DWI protocol based on the ACRIN 6698 clinical trial with a 16-channel breast coil (Sentinelle). The data were acquired with undersampling of R = 2, but the FOV was doubled so that the data could be treated as fully sampled. Because the 3-line navigators are not affected by the diffusion weighting, it was set to b = 0 s/mm^2 but the acquisition was repeated for 10 repetitions under two conditions. For the control, the phantom was scanned as usual with interactive static shimming. The experiment was then repeated with simulated "breathing" by rolling a saline bottle towards (up to about an ½ inch away) and away (up to about 10 inches away) from the phantom at about once per 2 seconds without touching the phantom. The movement of the water bottle through air will change the magnetic susceptibility of the scan area, which will change the B_0 shimming. This simulates the up and downward motion of the diaphragm that displaces air, which affects the B_0 field dynamically through time and is not accounted for with standard static shimming.

Offline, the phase difference of the complex raw 3-line navigator data was fit to a linear model after some smoothing (Savitzkey-Golay) and weighting by the signal

intensity, which provided a 0^{th} (ϕ) and 1^{st} (κ) order correction term that is unique for every coil, slice, and repetition. To consider the distribution of ϕ and κ in the control case, the edge slices with no signal were removed, as the fit is invalid without any signal. Assuming outlier estimates were caused by poor navigator fitting, outlier pairs were also removed. ϕ and κ were separately considered across the slices with signal, all channels, and ten repetitions of control data; pairs were removed if either was an outlier, defined based on three median absolute deviations from the median estimation.

In cases with navigator failures, a referenceless linear ghost correction technique, (ghost/object minimization, described in Chapter 4) was applied to consider whether other linear corrections could improve performance in individual slices and coils. The 2D simplex search was started at $\kappa = -0.6$ and $\phi = 0$. The resulting parameters were plotted with the navigator to compare solutions.

To consider the effect of simulated breathing, a single channel and slice was chosen with sufficient signal. The 10 timepoints represent a range throughout the respiratory cycle, where the worst-case scenario would be a navigator separated in time from the data by about ½ the respiratory cycle to cause the largest change in B_0. For demonstration purposes, the κ and ϕ pair from the repetition with the biggest difference between "breathing" and control was chosen and used for the following analysis.

Results:

Slice and coil dependence

Navigator estimates for a single repetition of control phantom data are shown in Figure 3.10a. Six slices were removed due to little or no signal in the slice. Out of 4800 estimated pairs, 112 κ estimates and 204 ϕ estimates were considered outliers, combined for 246 total pairs removed. The mean values were $\kappa = -0.643 \pm 0.0409$ and $\phi = 0.085 \pm 0.0438$, which correspond to a shift in k_x of about $0.64 * \Delta k_x$ between RO+ and RO- and 0.09 radians phase offset. The ghost correction parameter is mostly stable across the whole acquisition (Figure 3.10a); which is also consistent with other *in vivo* breast DWI acquisitions (data not shown) scanned on the same coil and two Siemens 3 T Prisma^{fit} systems. The parameters tend to vary smoothly over slices but have a clear

bimodal distribution across coils as shown in Figure 3.10b, which did *not* seem to correspond to the Left/Right coils or the position within the coil.

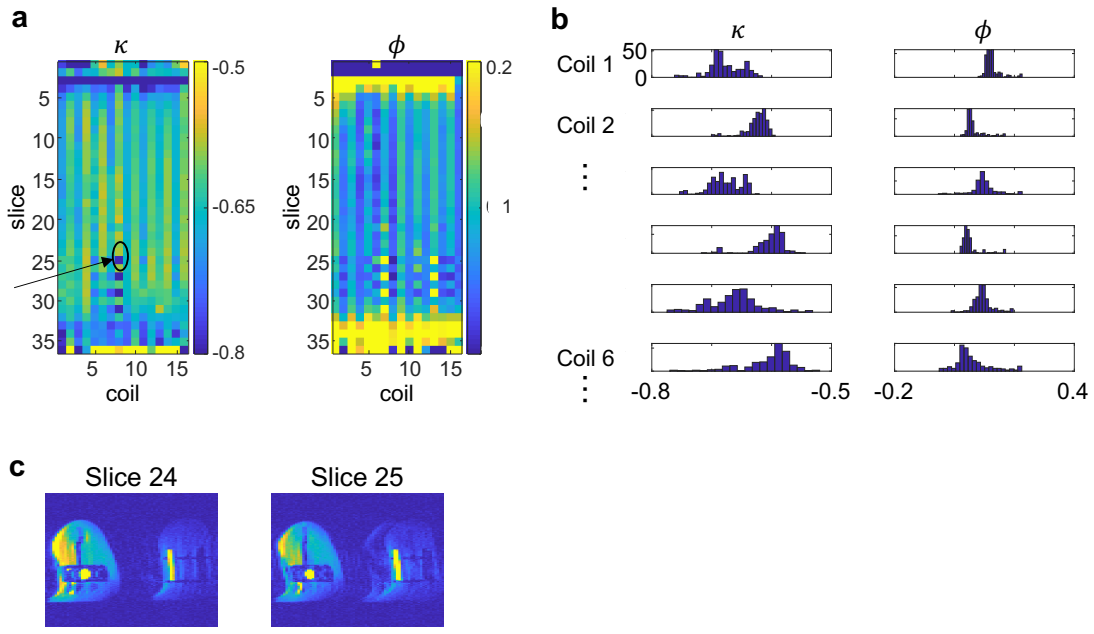

Figure 3.10 – Slice and coil distribution of κ and ϕ
The ghost parameters varied smoothly over slice (a) and showed a bimodal distribution across coils (b). Corrected images for coil 8, slices 24 and 25 are shown (c). The estimate for slice 24 was consistent with the rest of the acquisition, while slice 25's correction parameters were not (a, arrow). The outlier correction led to a residual ghost (c).

Considering the consistency across the acquisition, looking at these outlier data points can reveal some insight into where the navigator correction went wrong. From Figure 3.10, it is clear that channel 8, slice 25 did not follow smooth variation over the slices as expected. Figure 3.10c shows the reconstruction using the estimated ghost correction, demonstrating that this inconsistent point led to inferior ghost correction, compared to its neighbor whose correction was closer to the mean.

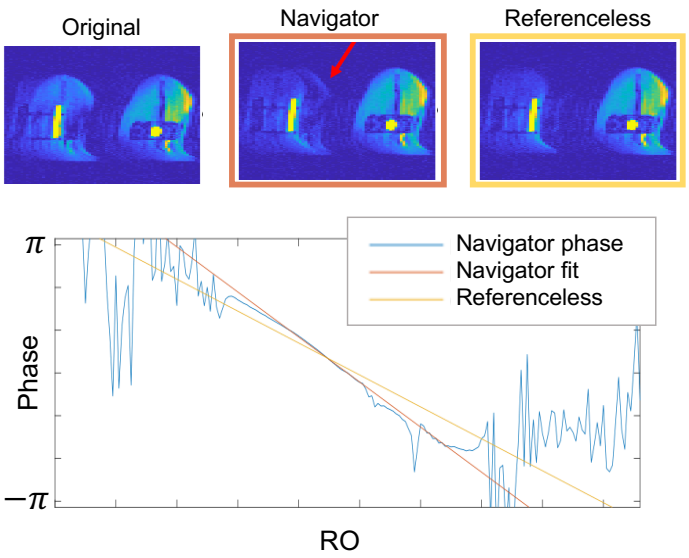

Figure 3.11 – Navigator with residual ghost
The navigator correction (red) left a residual ghost (arrow). The referenceless correction (yellow) did not fit the navigator data well but did reduce the ghost.

Considering this failed ghost correction, an interesting question was whether or not any combination of linear parameters would reasonably correct the ghost. If there was none, the ghosting artifact itself was likely non-linear. However, if another pair of ϕ and κ succeeded in correcting the ghost, this suggested that the navigator data was insufficient at measuring the linear phase error in this case. The 3-line navigator phase (blue line) and linear fit (red line) are shown in Figure 3.11. Although the navigator solution reasonably fit the navigator data, there was substantial residual ghosting (red arrow). On the other hand, the referenceless estimation (yellow line) reduced the residual ghost.

Breathing effect

The simulated breathing caused a shift in the image domain through time, as shown in Figure 3.12, which compares the control and breathing cases. Looking at a time series (data not shown), the phantom appeared to jump around in the PE direction through the 10 repetitions with simulated breathing and stayed stationary in the control case. To demonstrate this effect, a single time point (repetition 9) is shown in Figure 3.12, where a there is a small shift between the two images in the PE direction as demonstrated by plotting the signal through the PE direction. A constant shift in PE is caused by a shift in

the center resonance frequency, which can be readily estimated based on the magnitude and direction of the shift in PE. Notice that, to a lesser extent, the shift between the edges varied over the image space, consistent with geometric distortion caused by spatially varying change in B_0.

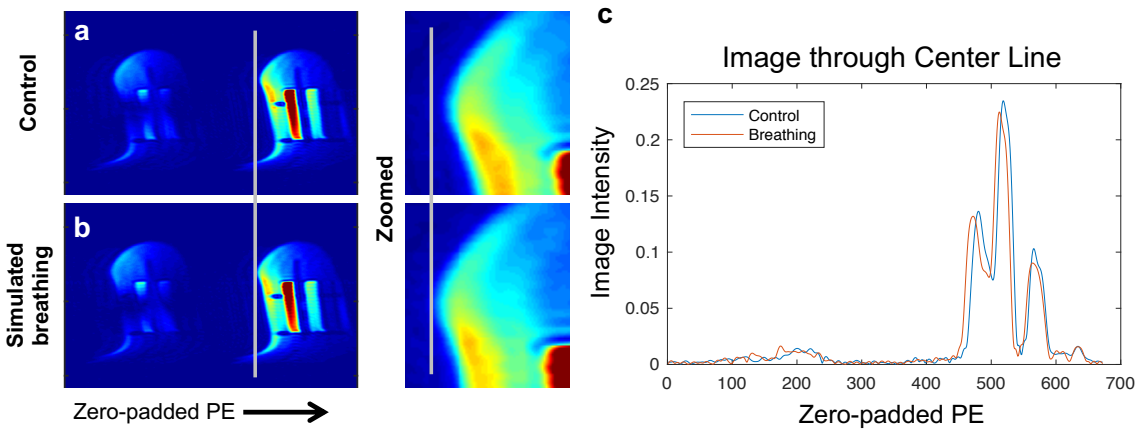

Figure 3.12 – The effect of "breathing" in the image domain
Breathing was simulated by rolling a water phantom into and out of the scanner. Images are pre-ghost corrected and zero-padded for better visualization. There is a small apparent shift in the PE direction between the control (a) and simulated breathing (b) cases, demonstrated by the grey line. The effect is further demonstrated by plotting the signal intensity through the center

Similarly, the navigator phase difference shifted slightly as the B_0 field changed, as shown in Figure 3.13b, which caused a larger variability in the estimates of κ (Figure 3.13c) and ϕ (Figure 3.13d). Figure 3.13e shows the effect of breathing on the navigator correction. Here, the control data was corrected based on the control navigator or based on the 'breathing' navigator. The inconsistent data caused a very small residual ghost (Figure 3.13e) that was not present in the static case.

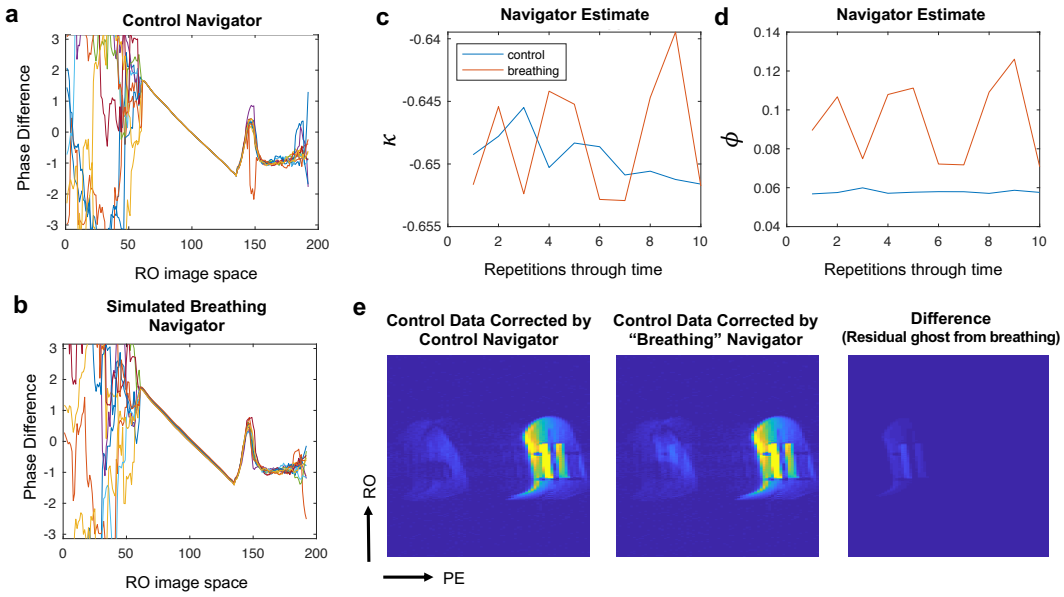

Figure 3.13 – The effect of "breathing" on the navigator
A small variability is visible in the navigator data when breathing was introduced (b vs a). This led an increase in variation of the estimated ghost parameters (c, d), which can lead to a residual ghost (e).

Discussion: Linear ghost correction parameters are relatively consistent throughout a data set where there is sufficient signal, varying smoothly over the slices and varying negligibly through repetitions in a phantom case without respiration or movement. There is a small bimodal effect across coil in the 16-channel Sentinelle breast coil that may be caused by delays in the electronics based on some polarity of the surface coils. These consistent corrections are associated with reliable ghost correction. However, in many cases the outlier ghost correction parameters correspond to insufficient ghost correction. These cases seem to occur for arbitrary combinations of slice, coil, and repetition despite being measured in phantom data without the presence of motion. Moreover, the failures were not consistent over repetitions (data not shown), highlighting the unreliable nature of the 3-line navigator. Importantly, there is in fact a linear correction that outperforms the navigator solution, adequately correcting the ghost.

When 'breathing' is introduced the variability across repetitions increases. However, the variability caused by changing B_0 inhomogeneity is small compared to the arbitrary failures, which suggests that large ghost correction failures observed in *in vivo* data are likely not caused solely by respiratory motion between the navigator and the

imaging data. However, small residual ghosts may be caused by small field perturbations between the time the navigator is measured and when the center of the echo is measured, as shown in Figure 3.13e. This effect was shown here for a breathing-like ΔB_0, however, eddy currents can also cause spatially varying field perturbations. Moreover, these effects can vary through the echo, causing a time-varying ghost (see Experiment 4 below).

Conclusion: The linear ghost parameters varied smoothly over slices and demonstrated a bimodal distribution across coils. Simulated breathing caused a small residual ghost but did not account for a navigator failure. Instead, outlier parameters caused ghost correction failure.

Experiment 3 – Sensitivity to Fat

The purpose of this experiment was to understand how large off resonance caused by unsuppressed adipose signal affects the linear navigator.

Methods: A cylindrical phantom containing water in the center surrounded by oil was scanned using a 2-channel head coil at isocenter. Low spatial resolution was used to achieve high SNR for a single 10 mm slice. The center frequency was purposefully shifted by 164 Hz towards the resonance peak of fat (from 12373715 to 123173551 Hz) in order to include some fat signal, representing failed fat suppression. 8 repetitions were acquired both with and without simulated breathing, as described above.

In a second experiment, two phantoms were scanned at multiple slices with the 16-channel breast coil. On one side of the coil, the phantom contained a tube of water surrounded by oil. In the other side, a cylindrical saline phantom was used. Thus, through the slice direction, some images contained water only, fat only, or both water and fat.

Results: In the image domain, there was significant signal left in the fat, which was shifted significantly from the water in the PE direction based on the echo spacing and the frequency difference. In this case, the water also shifted from its center position in PE because the frequency of water was also off resonance caused by the shift of the center frequency of the receiver, as Figure 3.14 shows. There was also a geometric distortion that occurred in both the water and the fat but more prominently in the fat; notice that the shape of the center tube of fat is much less round than that of the water signal.

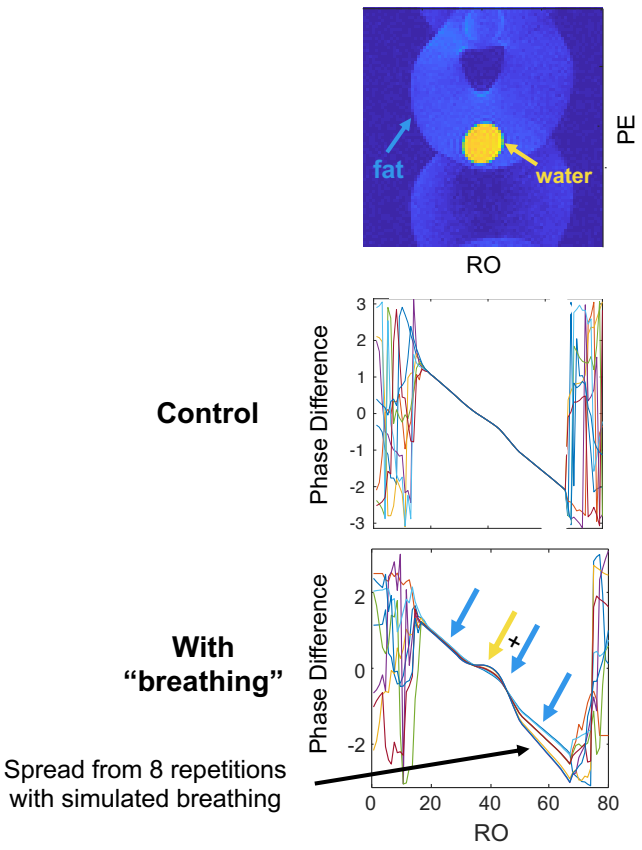

Figure 3.14 – The fat/water phantom
The water and fat were shifted in the PE direction. In the navigator, there was discontinuity between the water (yellow) and the fat (blue). The variability increased when breathing was introduced.

In the control case, the phase difference was quite linear in the region that corresponds to the fat, and there was a small non-linearity at the RO position that contained both fat and water through the PE projection. When a field perturbation was introduced by simulated breathing, this non-linearity became very prominent and varied with increasing and decreasing contribution from the water signal through the PE projection. Similar to Figure 3.13b, when breathing was introduced, the B_0 inhomogeneity caused phase accrual that increased through the RO train, which contributed to inconsistency in the phase difference.

These navigator solutions were tested in Figure 3.15. Despite the very linear phase in the control case and close fit (red line), the navigator solution was still insufficient and left a residual ghost of both the water and fat signal. However, another

linear solution, estimated by a referenceless method and plotted with a yellow line, reduced the ghost in both the fat and water regions (Figure 3.15).

Figure 3.15 – Ghost correction with failed fat suppression.
The navigator fit left residual ghost in both the water and the fat signal, while the referenceless correction, which does not reflect the navigator data, corrected the ghost.

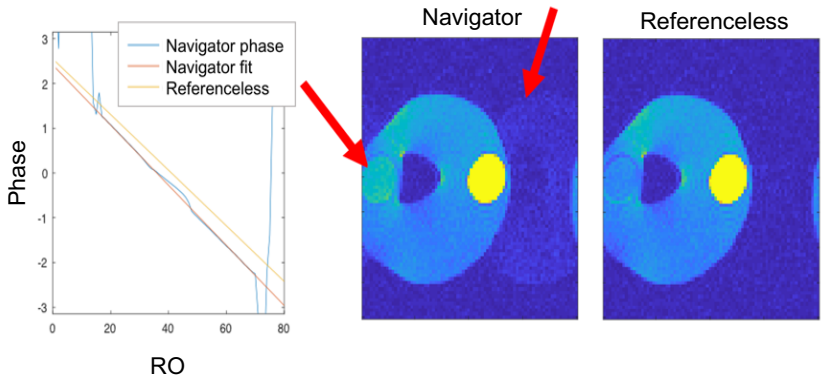

In the first experiment, in the single slice acquired, the content of fat and water varied across the RO direction, which led to two distinct regions of the navigator data throughout the RO: a region of all fat or a combination of both water and fat. In the second experiment, with rotated orientation and more slices, the distinction between water and fat occurred in the slice direction and the PE direction, which is collapsed in the navigator data. Thus, Figure 3.16 shows navigators from three slices that represent different scenarios. In a slice with water only, represented by the yellow line, the phase was linear, as expected. In a slice containing only fat (blue line), the phase was significantly shifted and nonlinear. The third navigator represents a PE projection at the slice marked by a red line, which included a mixture of fat and water; importantly, the fat and water signal were not separated in the RO direction as they were in the previous example. Here, the 0^{th} order component was consistent with that of water, but the non-linearity increased as the distance from isocenter increased caused by the simultaneous signal from both water and fat.

Discussion: These two water/fat phantom experiments are different in two major ways. First, we see that the orientation of alternating water and fat signal impacts the navigator data in different ways. In the RO direction, fat signal can cause discontinuities in the

phase, as seen in Figure 3.14. Whereas in the PE direction, the mixture of signal from fat and water affected the whole navigator, adding a non-linearity dependent of the distance from isocenter rather than the spatial location of the fat.

Figure 3.16 – Navigator through fat vs. water
Data is shown from three navigators. Navigator colors correspond to their spatial position in the T_2-weighted image (left). The fat only (blue) was nonlinear and had a large phase offset. The navigator in water (yellow) was linear as expected. While the navigator through fat and water (red) was close to that of water only, it was slightly nonlinear and shifted.

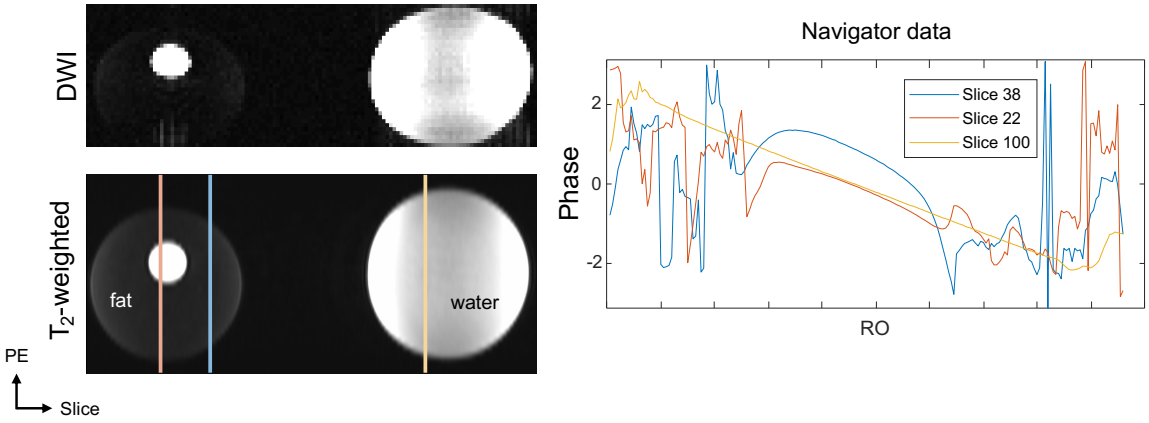

Secondly, the two experiments represent the inconsistent fat suppression that is often achieved in breast DWI. We can relate the first scenario to an *in vivo* scan with poor fat suppression. In this case, the fat signal greatly impacts the navigator data, increasing the susceptibility to B_0 changes and adding a large 0^{th} order phase shift. The second experiment represents a case in which the breast anatomy is mostly fatty, and the fat suppression performed well. Even though the fat signal is sufficiently suppressed and barely visible in the image domain (see Figure 3.16), it contributes to a strong phase difference measured by the navigator (blue line). This may be caused by the sequence timing; the gradient reversal is used for fat suppression of the imaging data, but the navigator is acquired prior to these 180º refocusing pulses. When this small signal is mixed with the strong water signal, the water plays a much larger role in the navigator phase, especially the 0^{th} order component, despite the small physical size of water region compared to the fat. However, the adipose signal still adds a non-linearity that can bias the navigator fit and cause residual ghosts.

Conclusion: Although the fat signal may appear to be suppressed in the image domain, the presence of adipose signal can largely shift the phase of the 3-line navigator, which may cause non-linearities where water and fat are mixed in the PE projection. The effect was especially large when simulated breathing was introduced, perturbing the system from its carefully shimmed state.

Experiment 4 – The full phase navigator

The full phase navigator is thought to correct for a time-varying ghost that is linear in space. Here this time-varying component was be characterized using simple phantom data and a full phase navigator.

Methods: A single saline phantom was scanned in one side of the 16-channel breast coil with full FOV and no undersampling. For a full-phase navigator acquisition, the scan was repeated with phase encoding disabled. For every other line, a 1st-order phase error was estimated based on the line and its two surrounding lines averaged together. This corresponds to a three-line navigator that is repeated through time for the length of the echo train with the same timing as the main acquisition.

Results: The 1st order phase error parameters are plotted through the echo train for 5 consecutive slices with high signal measured by 4 different channels (Figure 3.17a). In this simple saline phantom, the 1st order phase error varied substantially over the echo train, especially in the beginning of the echo train. This time dependence was consistent across the slices and coils, except for a shift between two sets of coils, similar to the observations in Figure 3.10 above.

In Figure 3.17c, data from one slice were corrected with the solutions shown in Figure 3.17b, which compares the time-varying 1st order phase with three static estimates based on the three-line navigator, the average over the full phase navigator, and a referenceless method. The 3-line navigator solution closely resembled that measured at the beginning of the echo train, as one would expect. This correction left a clear residual ghost whereas the full phase average and the referenceless methods compared more to the latter part of the echo train and reduced the ghost. While these static estimates were

reasonably effective, applying the full phase 1st order correction further reduced the ghost.

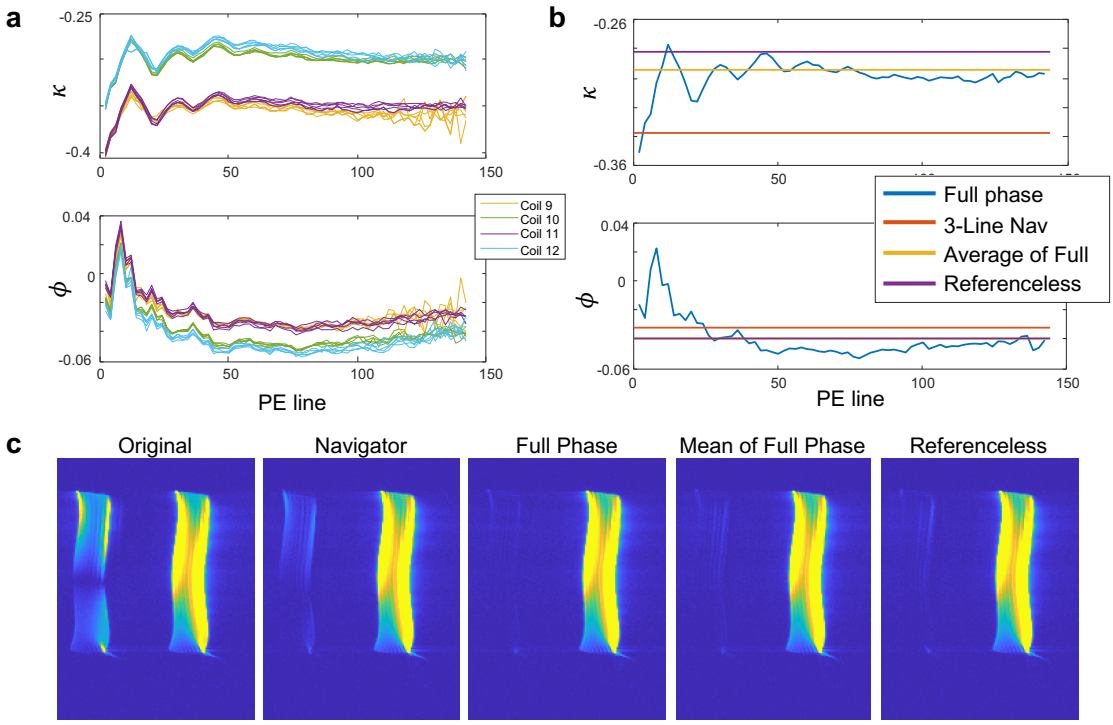

Figure 3.17 – The full phase navigator in phantom
The full phase parameters are plotted for 5 slices and 4 different coils with high signal (a). The full phase estimates are compared to the navigator, average of full phase over the echo train, and a referenceless solution (b). All corrections were applied for comparison (c).

An example of an *in vivo* full phase navigator estimation from 3 slices is shown in Figure 3.18. Here, there was again a large variation at the beginning of the RO train that stabilized around $k_x = 20$. However, the time course was less distinct, especially towards the end of the train where the full phase navigator estimated outlier values that suggest a fitting failure.

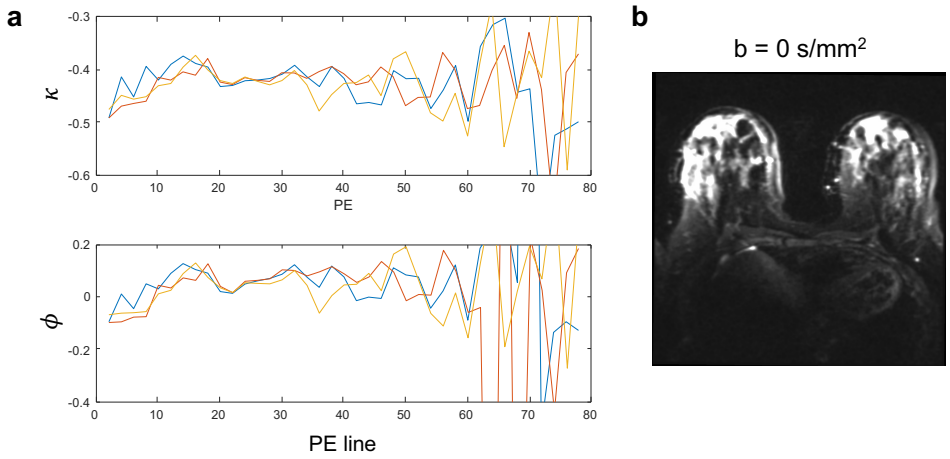

Figure 3.18 – The full phase navigator *in vivo*.
The full phase parameters are plotted for a single coil and three slices (b) with high signal for a case with high SNR (b)

Discussion: In the clean phantom case, the full phase κ estimates that sufficiently correct for ghosts distinctly resemble a dampened harmonic oscillator, which is consistent with eddy currents that quickly die off after the excitation. If one can reliably measure these effects, the dynamic correction better corrects for ghosts. However, in the *in vivo* case this estimation is complicated by respiratory motion and fat signal that may disrupt the phase measurement. We also see that the error increases towards the end of the RO train as the signal decays, especially in the *in vivo* data. Moreover, the full phase navigator is separated in time from every subsequent acquisition. Heating could cause a change in the eddy currents and repeating the full phase navigator throughout the scan adds significant scan time as it requires a full acquisition. Thus, a less accurate but more reliable correction should represent the majority of the readout, especially near the center of k-space, rather than the beginning of the train where the eddy current effect is likely strongest.

Conclusion: The linear ghost parameters evolved over time in a way similar to that of eddy currents that quickly die off. Measuring the navigator soon after the excitation where the eddy current effect is greatest, may cause residual ghosts.

3.3.2 The 2-dimensional ghost

Many advanced ghost correction methods assume that the linear ghost model is insufficient. In this experiment the 2D phase map was characterized and tested compared to a 1D correction.

Methods: The CaliberMRI breast phantom was scanned at 3 T using the 16-channel Sentinelle breast using a standard axial SE-EPI, b = 0 s/mm$_2$, and R = 2 undersampling. For a phase reference, an additional b = 0 s/mm^2 acquisition was acquired with double FOV and fully sampled (R = 1). The reference scan was separated to make two full FOV images with fully sampled RO+ and RO- data. The 16 channels were combined using a SENSE R = 1 combination based on the sensitivity profiles, and a phase map was generated by comparing the two coil-combined image phase. Phase maps were fit to a 1-dimensional surface ($\Phi = \phi + \kappa x$) and a 2-dimensonal surface ($\Phi = \phi + \kappa x + \lambda y + \gamma xy$), which were applied to the tight FOV, R = 2 data and ACS lines before unaliasing with GRAPPA.

Figure 3.19 – 2D phase mapping in phantom
The phase map (a) was measured on fully-sampled, double FOV data. It was fit to 1D (b) and 2D surfaces (c) and applied to the undersampled imaging data. The 2D model did not improve the ghost correction compared to the 1D model.

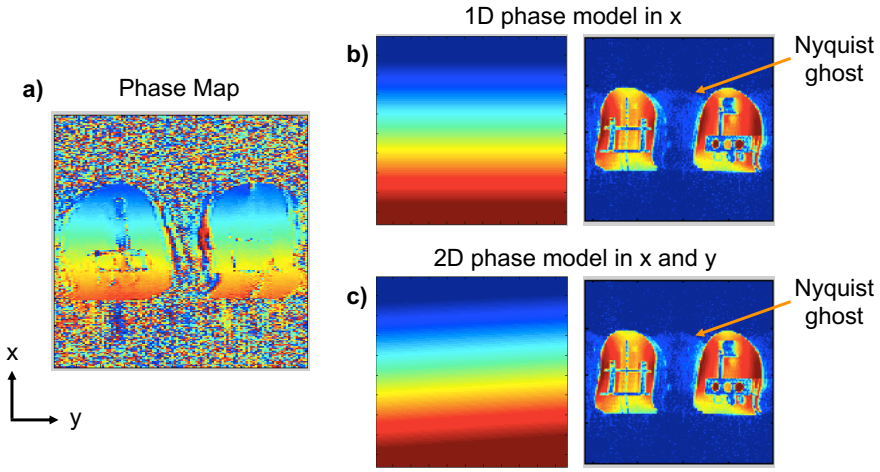

Results: On the coil-combined, phase maps (Figure 3.19a), the 1D model estimated $\kappa = 1.3131$ and $\phi = -0.1105$ (Figure 3.19b), and the 2-D model estimated $\kappa = 1.3055$, $\phi = 0.0461$, $\lambda = 0.0785$, and $\gamma = 0.0068$ (Figure 3.19c), indicating that the phase contained a non-negligible y component. The resulting root sum of square images are

shown in Figure 3.19 from both models, which shows that the 2-D phase correction did not improve the Nyquist ghosts. Note that Nyquist ghosts fall at FOV/4 in unaliased images based on the R = 2 undersampling.

Discussion: Although the phase map seems to contain a y component, the 2D model did not improve the ghost correction compared to a simple 1D model. Moreover, phase mapping faces some other key challenges. For one, the 16 channels were combined in order to obtain a full phase map that could be reliably fit. This prevents the use of coil-specific corrections, which may be especially important considering the bimodal coil dependence observed in Section 3.3.1, Experiment 2 above. Secondly, phase mapping requires the additional acquisition to obtain fully sampled RO+ and RO- sets. The acquisition of this reference is time consuming and can be complicated. For example, in this case, a fully sampled double FOV b = 0 s/mm^2 image was used, which has 4 times the amount of distortion compared to the imaging data. A single b = 0 s/mm^2 reference is practical, considering scan time, but does not account for changes in the ghost parameters or additional effects of eddy currents induced by diffusion encoding gradients.

Conclusion: The Nyquist ghost phase was mostly linear in space. The 2D components were negligible in the image domain and measuring the 2D phase requires time consuming reference data and prevents a channel-specific correction.

3.3.3 Nyquist ghosts and accelerated imaging

EPI is typically acquired with some level of in-plane parallel imaging to reduce the echo spacing and scan time. Nyquist ghosts can affect both undersampled data and reference data, like autocalibration scans (ACS), which can have downstream effects on GRAPPA unaliasing etc. The purpose of this experiment was to understand the various artifacts caused by GRAPPA, ghosts, and combinations thereof.

Methods: A modified Shepp-Logan phantom was simulated as if acquired with 8 channels arranged in a circular pattern, including smooth sensitivity profiles, added complex noise, and undersampling for $1 \leq R \leq 4$. 1st order ghost artifacts ($\kappa = 0.4, \phi = 0$) were added to either the undersampled data, ACS data, or both. Aliasing artifacts were simulated by randomly setting 20% of weights to 0.

Results: Figure 3.20 demonstrates the overall effect of uncorrected Nyquist ghosts in both the reference and the undersampled data. The ideal correction and unaliasing are shown in the top row. Notice that when the ACS data was not fully ghost corrected, it caused a GRAPPA aliasing artifact at FOV/2 (row 3).

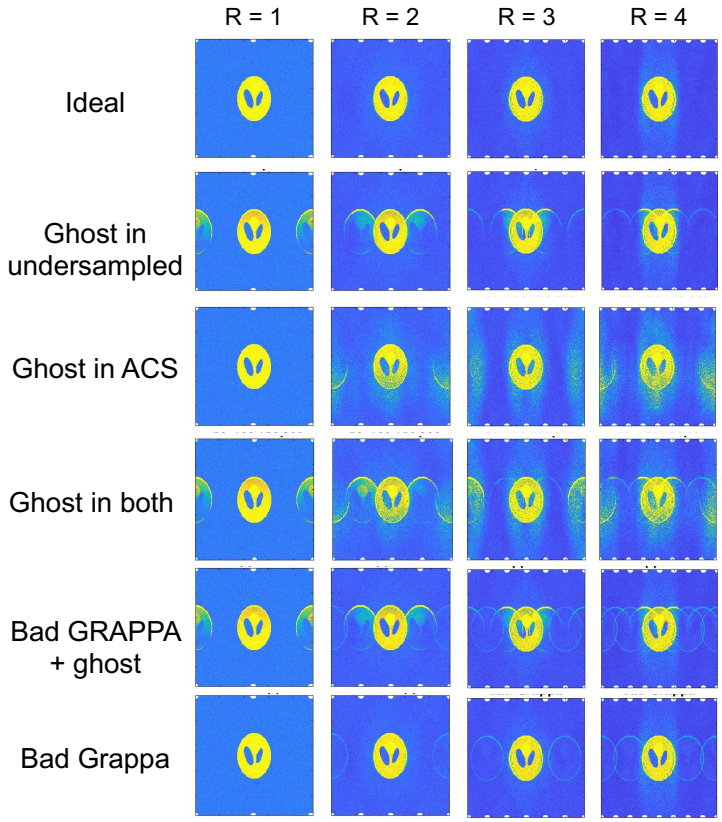

Figure 3.20 – Ghosts vs. aliasing artifacts
Various combinations of simulated ghosts and aliasing artifacts, which both occur in the PE direction. Importantly, residual ghosts in ACS data cause aliasing artifacts (row 3). White dots mark 1/2R intervals.

Discussion: This demonstrates that reliable and accurate ghost correction of all data is critical for high-quality images, especially if unaliasing comes downstream the pipeline from ghost correction. An iterative approach, alternating between ghost correction and other processing, may be useful but time consuming.

Because Nyquist ghosts occur in the PE direction, ghosts and aliasing artifacts can get messy when the two are mixed together. Unaliasing errors are often mislabeled as Nyquist ghosts and vice versa. However, it is possible to tell them apart based on their

location in the image. For example, aliasing artifacts fall at $\frac{FOV}{R}$, while Nyquist ghosts in the undersampled data will fall at $\frac{FOV}{2R}$.

Conclusion: Reliable ghost correction of both the ACS data and undersampled data is important for high quality unaliasing. Nyquist ghosts and aliasing artifacts are often mis-diagnosed.

3.4 Discussion

The preliminary studies above were critical in the development of this work, creating a clear path forward in the correction of Nyquist ghosts in breast DWI. To review, these explorations found the following results:

- Using a three-line navigator accounts for small, static B_0 inhomogeneity by averaging over two RO+ lines acquired before and after a single RO- line.
- The ghost parameters vary slowly across slices and bimodally across coils. Outlier correction parameters estimated by the navigator suggest a navigator failure. In these cases, the navigator data poorly represents the data itself.
- Respiration causes dynamic changes in B_0, which causes spatial shifts in PE in the image domain and slight variation of the navigator data. In the presence of breathing, separation between the navigator and ghosted data may lead to small residual ghosts.
- While fat suppression may appear sufficient in the image domain, it can add deleterious phase shifts to the navigator data. These affects are even greater in the presence of respiration, which alters the B_0 field.
- The linear ghost parameters change through time, probably caused by short-lived eddy currents. While a full phase navigator correction most accurately corrects the ghosts, the measurement of such navigator is unreliable. Thus, it is important to account for the majority of the readout for ghost correction estimation, rather than just the beginning of the acquisition, as the 3-line navigator typically does.

- The RO+/RO- phase differences are mostly linear in space. Measuring the small 2D components requires combination of channel data and does not seem to improve the ghost correction performance.
- Accurate and complete ghost correction of reference data is critical for quality downstream reconstruction, like GRAPPA unaliasing and slice separation in SMS.

To sum it up: in breast DWI the ghost artifact is mostly linear. However, the linear three-line navigator is unreliable for the estimation of the 1st order correction parameters. The navigator is extremely sensitive to fat and is separated in time from the center of the echo.

While there are numerous advance ghost correction methods that assume more complicated models, the ghosting problem seems to boil down to the unreliable nature of the 3-line navigator, rather than a failure to capture more complex behavior. This suggested the need for an alternative linear strategy that is consistent with 1) the center of the echo, and 2) the fat suppressed imaging data. Referenceless methods fulfill these criteria as they use the data itself to estimate the ghost correction by minimizing a specified cost function that corresponds to the ghost level. Additionally, these methods can be applied to a wide variety of data without the need of extra navigators, including reference data and independent slices, channels, and acquisitions.

The success of referenceless methods can be dependent on the image geometry and the use of undersampling. Thus, several cost functions have been proposed, including image entropy, a singular value decomposition of k-space, and others that require manual ROI placement. In the exploration of the variable performance of these referenceless methods and the derivation of the ghost artifact in the image domain (Section 3.1), the idea for a novel referenceless method was developed. This method, Ghost/Object minimization (Chapter 4), is based on the predictable nature of the ghost in the image domain, including a sine and cosine signal modulation and a FOV/2 position.

Chapter 4: Ghost/Object Minimization: A Novel Referenceless Ghost Correction Method

Illuminating the nature of the Nyquist ghost and understanding the failure of the standard 3-line navigator in breast DWI guided the use of referenceless methods and the development of a new referenceless ghost correction. The method, called Ghost/Object (as in "ghost over object"), minimizes Nyquist ghosts using a cost function that relies on the sine and cosine modulation of the ghosted image. This development led to the publication of a paper (106) and a patent application (107) and contributed to 4 conference abstracts (108–111).

4.1 Formulation of Ghost/Object Minimization

The cost function for Ghost/Object minimization (G/O) is calculated by taking the ratio of the magnitude of the measured image over a shifted copy, applying a 2D median filter for denoising, and summing over all pixels in the image domain as follows:

$$f_{cost}{}^{-1} = \sum_{x,y} F_{med\ 2D}\left(\frac{|I_{meas}(x,y)|}{|I'_{meas}(x,y)|}\right) \quad [4.1]$$

where $F_{med\ 2D}$ refers to a 2D median filter applied to reduce image noise and $I_{meas}(x,y)$ is the measured image. $I'_{meas}(x,y)$ refers to the measured image that is shifted by $\frac{(2j+1)FOV_y}{2R}$ for j from 0 to $R-1$ such that the object is aligned with the theoretical location(s) of the ghost(s), per Equation 3.9, and FOV_y refers to the FOV in the PE direction. For practical purposes, j can be restricted to the sum over $j = 0$ and $j = R-1$, which corresponds to the higher intensity ghosts located closest to the object.

The summation is taken over the entire image and does not require selection of the object or ghost regions, however, any pixels in $I'_{meas}(x,y)$ with very low noise values may bias the cost function by adding an overly large value to the summation. Therefore, the 2D median filter, $F_{med\ 2D}$, is applied to remove these outlier values.

4.1.1 Justification for G/O minimization

The exact value of the cost function will depend on the geometry of the object, which will determine the amount of overlap between the ghost and the object in the PE FOV. Thus, it cannot be shown analytically that f_{cost} is minimized when $\phi = \kappa = 0$ for all conditions. However, by separately considering ϕ and κ, the cost function can be analytically shown to be minimized in a ghost-free image in order to gain intuition about why it works. Consider the case in which k-space is fully sampled ($R = 1$) with one segment ($N_{seg} = 1$), and the ghost only contains a 0th order component. While this situation can be understood to be impractical, it provides an illustration of the method.

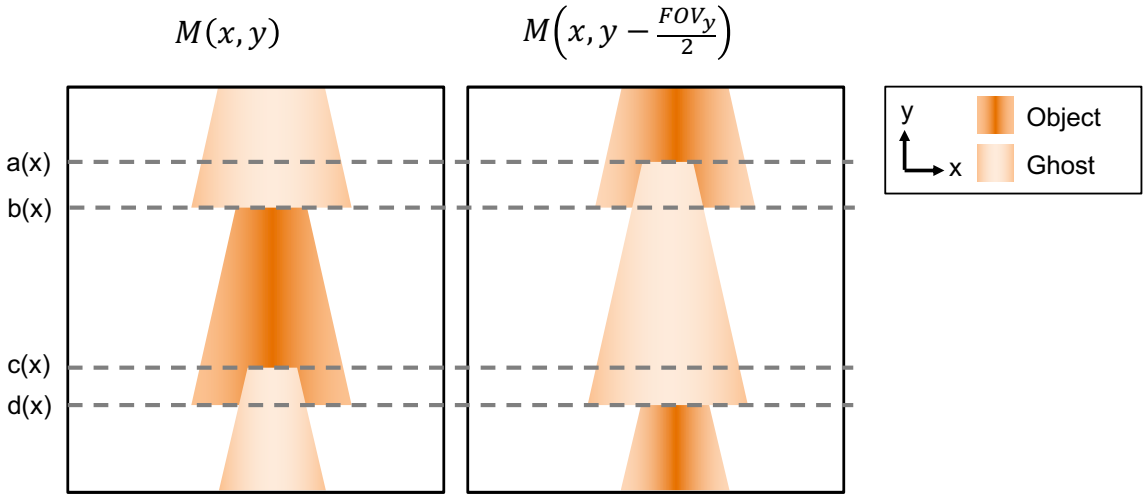

Figure 4.1 Introducing Ghost/Object Minimization
Assume a non-overlapping linear ghost, as shown. We consider each region through PE (0 to a, a to b, etc.).

Case 1: 0th order ghost only ($\kappa = 0, \phi \neq 0$)

First plug Equation 3.9 into the cost function; for simplicity we assume $\kappa = 0$, temporarily ignore the median filter, and describe the discrete sum as a continuous integral over the image.

$$f_{cost}{}^{-1} = \int_0^{FOV_x} \int_0^{FOV_y} \frac{I_0(x,y)\cos(\phi) + iI_0\left(x, y - \frac{FOV_y}{2}\right)\sin(\phi) + \epsilon(x,y)}{I_0\left(x, y - \frac{FOV_y}{2}\right)\cos(\phi) + iI(x,y)\sin(\phi) + \epsilon\left(x, y - \frac{FOV_y}{2}\right)} dy\, dx \quad [4.2]$$

For any given position in x, the image can be broken into four parts over dy, one region of pure ghost defined between $0 \rightarrow a(x)$, a region of overlapping object and ghost defined between $a(x) \rightarrow b(x)$ and $c(x) \rightarrow d(x)$, a region of pure object defined between $b(x) \rightarrow c(x)$, and another region of pure ghost from $d(x) \rightarrow FOV_y$, where a, b, c, and d are functions of x (demonstrated in Figure 4.1). Thus, the integral becomes:

$$
\begin{aligned}
f_{cost}{}^{-1} = \int_0^{FOV_x} \Bigg(& \int_0^{a(x)} \frac{I_0(x,y)\cos(\phi) + iI_0'(x,y)\sin(\phi) + \epsilon(x,y)}{I_0'(x,y)\cos(\phi) + iI(x,y)\sin(\phi) + +\epsilon'(x,y)}\,dy \\
& + \int_{a(x)}^{b(x)} \frac{I_0(x,y)\cos(\phi) + iI_0'(x,y)\sin(\phi) + \epsilon(x,y)}{I_0'(x,y)\cos(\phi) + iI(x,y)\sin(\phi) + +\epsilon'(x,y)}\,dy \\
& + \int_{b(x)}^{c(x)} \frac{I_0(x,y)\cos(\phi) + iI_0'(x,y)\sin(\phi) + \epsilon(x,y)}{I_0'(x,y)\cos(\phi) + iI(x,y)\sin(\phi) + +\epsilon'(x,y)}\,dy \\
& + \int_{c(x)}^{d(x)} \frac{I_0(x,y)\cos(\phi) + iI_0'(x,y)\sin(\phi) + \epsilon(x,y)}{I_0'(x,y)\cos(\phi) + iI(x,y)\sin(\phi) + +\epsilon'(x,y)}\,dy \\
& + \int_{d(x)}^{FOV_y} \frac{I_0(x,y)\cos(\phi) + iI_0'(x,y)\sin(\phi) + \epsilon(x,y)}{I_0'(x,y)\cos(\phi) + iI(x,y)\sin(\phi) + +\epsilon'(x,y)}\,dy \Bigg) dx
\end{aligned}
\qquad [4.3]
$$

Where $I_0'(x,y) = I_0\left(x, y - \frac{FOV_y}{2}\right)$, $\epsilon' = \epsilon\left(x, y - \frac{FOV_y}{2}\right)$, and we describe the inverse cost-function to simplify the notation. Due to the N/2 nature of the ghost, the regions $0 \rightarrow a(x)$ and $b(x) \rightarrow c(x)$ can be combined; we can also simplify them by 1) recognizing that some of the terms are 0 in the specified region, and 2) assuming the noise is negligible, i.e.:

$$
\begin{aligned}
& \int_0^{a(x)} \frac{|I_0(x,y)\cos(\phi) + iI_0'(x,y)\sin(\phi) + \epsilon(x,y)|}{|I_0'(x,y)\cos(\phi) + iI_0(x,y)\sin(\phi) + \epsilon'(x,y)|}\,dy \\
& \qquad = \int_0^{a(x)} \frac{|I_0(x,y)\cos(\phi) + \epsilon(x,y)|}{|I_0(x,y)\sin(\phi) + \epsilon'(x,y)|}\,dy \approx \int_0^{a(x)} |\cot(\phi)|\,dy
\end{aligned}
\qquad [4.4]
$$

and

$$\int_{\mathrm{b(x)}}^{c(x)} \frac{|I_0(x,y)\cos(\phi) + iI_0'(x,y)\sin(\phi) + \epsilon(x,y)|}{|I_0'(x,y)\cos(\phi) + iI_0(x,y)\sin(\phi) + \epsilon'(x,y)|}dy$$

$$= \int_{b(x)}^{c(x)} \frac{|iI_0'(x,y)\sin(\phi) + \epsilon(x,y)|}{|I_0'(x,y)\cos(\phi) + \epsilon'(x,y)|}dy \approx \int_{b(x)}^{c(x)} |\tan(\phi)|dy \quad [4.5]$$

Thus, we can rewrite the cost function as

$$f_{cost}^{-1} \approx \int_0^{FOV_x} \left(\int_0^{a(x)} |\cot(\phi)| + |\tan(\phi)|\, dy \right.$$

$$+ \int_{a(x)}^{b(x)} \frac{|I_0(x,y)\cos(\phi) + iI_0'(x,y)\sin(\phi)|}{|I_0'(x,y)\cos(\phi) + iI_0(x,y)\sin(\phi)|}dy$$

$$+ \int_{c(x)}^{d(x)} \frac{|I_0(x,y)\cos(\phi) + iI_0'(x,y)\sin(\phi)|}{|I_0'(x,y)\cos(\phi) + iI_0(x,y)\sin(\phi)|}dy$$

$$\left. + \int_{d(x)}^{FOV_y} \frac{|\epsilon(x,y)|}{|\epsilon'(x,y)|}dy \right) dx \quad [4.6]$$

$$\approx \int_0^{FOV_x} \left(\int_0^{a(x)} |\cot(\phi)| + |\tan(\phi)|\, dy \right.$$

$$+ \int_{a(x)}^{b(x)} \frac{\left|\cos(\phi) + i\frac{I_0'(x,y)}{I_0(x,y)}\sin(\phi)\right|}{\left|\frac{I_0'(x,y)}{I_0(x,y)}\cos(\phi) + i\sin(\phi)\right|}dy$$

$$\left. + \int_{c(x)}^{d(x)} \frac{\left|\cos(\phi) + i\frac{I_0'(x,y)}{I_0(x,y)}\sin(\phi)\right|}{\left|\frac{I_0'(x,y)}{I_0(x,y)}\cos(\phi) + i\sin(\phi)\right|}dy + \int_{d(x)}^{FOV_y} \frac{|\epsilon(x,y)|}{|\epsilon'(x,y)|}dy \right) dx$$

where we have again assumed $\epsilon(x,y) \approx 0$ in the signal regions $a(x) \to b(x)$ and $c(x) \to d(x)$.

Now we can evaluate the limits of each region; it is sufficient to consider $\phi = 0$, $\phi = \pm\frac{\pi}{4}$, and $\phi = \pm\frac{\pi}{2}$ due to the sinusoidal behavior and the absolute value. In the overlap regions:

$$\frac{\left|\cos(\phi) + i\frac{I_0{}'(x,y)}{I_0(x,y)}\sin(\phi)\right|}{\left|\frac{I_0{}'(x,y)}{I_0(x,y)}\cos(\phi) + i\sin(\phi)\right|} = \begin{cases} \dfrac{1}{\frac{I_0{}'(x,y)}{I_0(x,y)}} = \dfrac{I_0(x,y)}{I_0{}'(x,y)} & \text{for } \phi = 0 \\ \dfrac{\frac{1}{\sqrt{2}}\left(1 + \frac{I_0{}'(x,y)}{I_0(x,y)}\right)}{\frac{1}{\sqrt{2}}\left(\frac{I_0{}'(x,y)}{I_0(x,y)} + 1\right)} = 1 & \text{for } \phi = \dfrac{\pm\pi}{4} \\ \dfrac{\frac{I_0{}'(x,y)}{I_0(x,y)}}{1} = \dfrac{I_0{}'(x,y)}{I_0(x,y)} & \text{for } \phi = \dfrac{\pm\pi}{2} \end{cases} \quad [4.7]$$

In the ghost- and object-only regions:

$$|\cot(\phi)| + |\tan(\phi)| = \begin{cases} \infty + 0 = \infty & \text{for } \phi = 0 \\ 1 + 1 = 2 & \text{for } \phi = \dfrac{\pm\pi}{4} \\ 0 + \infty = \infty & \text{for } \phi = \dfrac{\pm\pi}{2} \end{cases} \quad [4.8]$$

Finally, we can assume the noise-only regions are negligible due to the median filter, which removes salt and pepper noise: $F_{med2D}\left(\frac{|\epsilon(x,y)|}{|\epsilon\prime(x,y)|}\right) \approx 0$

It is clear that the regions that dominate the magnitude of the cost function are the ghost- and object- only regions. Thus:

$$\begin{aligned} {f_{cost}}^{-1} &\approx \int_0^{FOV_x}\int_0^{a(x)} |\cot(\phi)| + |\tan(\phi)|\, dy\, dx \\ &= 2A_{Object}(|\cot(\phi)| + |\tan(\phi)|) \end{aligned} \quad [4.9]$$

where $A_{Object} = A_{Ghost}$ is the number of pixels in the object- or ghost-only image. This inverse cost function approaches ∞ at $\phi = 0$, which corresponds to the ghost-free image, and $\phi = \frac{\pi}{2}$, which manifests as a ghost-only image. Therefore, f_{cost} has a unique minimum at $\phi = 0$, when the image is ghost-free, if ϕ is restricted between $\frac{-\pi}{2} < \phi < \frac{\pi}{2}$.

Case 2: 1st order ghost only ($\phi = 0, \kappa \neq 0$)

Similarly, if we consider f_{cost} as a function of κ and let $\phi = 0$,

$$
\begin{aligned}
{f_{cost}}^{-1} \approx \int_0^{FOV_x} \Bigg(& \int_0^{a(x)} \left|\cot\left(\frac{2\pi\kappa x}{N_x}\right)\right| + \left|\tan\left(\frac{2\pi\kappa x}{N_x}\right)\right| dy \\
& + \int_{a(x)}^{b(x)} \frac{\left|\cos\left(\frac{2\pi\kappa x}{N_x}\right) + i\frac{I_0'(x,y)}{I_0(x,y)}\sin\left(\frac{2\pi\kappa x}{N_x}\right)\right|}{\left|\frac{I_0'(x,y)}{I_0(x,y)}\cos\left(\frac{2\pi\kappa x}{N_x}\right) + i\sin(\frac{2\pi\kappa x}{N_x})\right|} dy \\
& + \int_{c(x)}^{d(x)} \frac{\left|\cos\left(\frac{2\pi\kappa x}{N_x}\right) + i\frac{I_0'(x,y)}{I_0(x,y)}\sin\left(\frac{2\pi\kappa x}{N_x}\right)\right|}{\left|\frac{I_0'(x,y)}{I_0(x,y)}\cos\left(\frac{2\pi\kappa x}{N_x}\right) + i\sin(\frac{2\pi\kappa x}{N_x})\right|} dy \\
& + \int_{d(x)}^{FOV_y} \frac{|\epsilon(x,y)|}{|\epsilon'(x,y)|} dy \Bigg) dx
\end{aligned}
\qquad [4.10]
$$

Again, in the ghost- and object-only regions, the value within the integral approaches ∞, so we approximate the cost function as $f_{cost}^{-1} \approx \int_0^{FOV_x} \int_0^{a(x)} \left|\cot(\frac{2\pi\kappa x}{N_x})\right| + \left|\tan(\frac{2\pi\kappa x}{N_x})\right| dy\, dx$. Now ${f_{cost}}^{-1}$ approaches ∞ in the ghost-free image where $\kappa = 0$ but also approaches ∞ where $X = 0$ and for some other values of κ and X. However, due to noise in the image, the practical values of $\left|\cot\left(\frac{2\pi\kappa x}{N_x}\right)\right| + \left|\tan\left(\frac{2\pi\kappa x}{N_x}\right)\right|$ never reach ∞. Therefore, because $\lim_{\kappa\to 0} \left|\cot\left(\frac{2\pi\kappa x}{N_x}\right)\right| + \left|\tan\left(\frac{2\pi\kappa x}{N_x}\right)\right| = \infty$ for all values of X, taking the integral over X yields a global maximum at $\kappa = 0$ and local maxima at the other values where $\left|\cot\left(\frac{2\pi\kappa x}{N_x}\right)\right| + \left|\tan\left(\frac{2\pi\kappa x}{N_x}\right)\right| = \infty$, theoretically.

This can be shown graphically as well in Figure 4.2. First consider the case where $\phi = 0$ and choose a reasonable range for x and κ, -96 < x < 96 and -1.5 < κ < 1.5. It can be seen in Figure 4.2a that $\kappa = 0$ minimizes the Ghost/Object for all values of x. Thus, the sum over x is also minimized at $\kappa = 0$, as shown in Figure 4.2b. Next, consider the case in which κ = 0 and choose -96 < x < 96 and –π/2< ϕ < π/2. Again, for all values of x, $\phi = 0$ minimizes the Ghost/Object, as seen in Figure 4.2c-d.

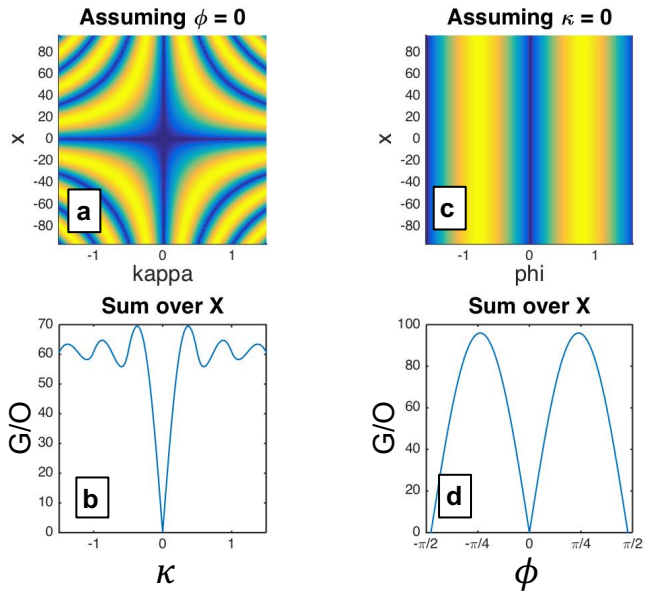

Figure 4.2 Ghost/Object metric for simple case
When ϕ = 0, we can show that G/O is minimized for κ = 0 (a and b). Similarly, when κ = 0, we can show that G/O is minimized for $\phi = 0$ (c and d).

To summarize, due to the sine and cosine modulation of the signal intensity in the ghost and object, respectively (Equation 3.9), the range of the inverse cost function for G/O minimization, ${f_{cost}}^{-1}$, spans from some finite positive number, which we will call C, to ∞ in the ghost- and object-only regions, where C depends on the size of the object-only region. Within the region of overlap, ${f_{cost}}^{-1}$ also spans between two finite numbers that depend on the dynamic range of the object signal and the size of the object region. Therefore, it is reasonable to assume that the cost function is dominated by the ghost-only region, and thus has a minimum when $\kappa = \phi = 0$, which characterizes the ghost-free image.

Numerical Demonstration of G/O minimization

In the more realistic case where the ghost consists both a linear and constant terms, a simulation of a Shepp-Logan phantom can be used to demonstrate that there is also a local minimum at $\kappa = 0$ and $\phi = 0$ for various degrees of ghost/object overlap and PE undersampling. A linear ghost was added to each ideal phantom for κ from -2 to 2 in steps of 0.1 and ϕ from -0.5 to 0.5 in steps of 0.02. In this study, the Ghost/Object cost

function was again minimized in the ideal case where $\kappa = 0$ and $\phi = 0$. (Figure 4.3a). Similarly, the Ghost/Object cost function was minimized at $\kappa = \phi = 0$ for undersampling from R = 1 to R = 4 (Figure 4.3b). *Note: An alternative to dealing with undersampling is to measure the G/O metric on unaliased images after ghost correction; in this case the shift factors should be chosen to align with the ghost. In this way, Ghost/Object is not limited by undersampling. However, incorporating GRAPPA unaliasing into the minimization is time consuming.

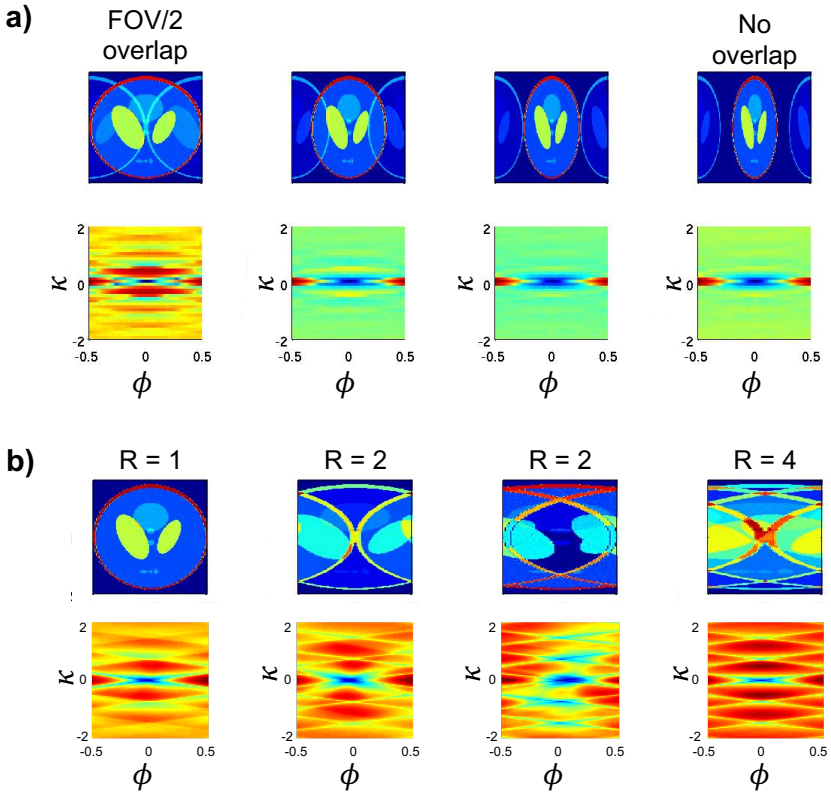

Figure 4.3 – Testing G/O with overlap and undersampling
The G/O metric is shown for Shepp-Logan simulations with varying degrees of ghost and object overlap (a) and undersampling from R = 1 to 4 (b). The global minimum occurs at $\kappa = \phi = 0$ for all cases in the Shepp-Logan phantom, confirming that Ghost/Object minimization was not sensitive to undersampling or tight FOVs. However, the exact value of the cost function will depend on the geometry and signal variation in y.

4.2 Nyquist Ghost Correction of Breast DWI using Referenceless Methods

This work was previously published in *Magnetic Resonance in Medicine*, 2019; 81:2624-2631. Jessica A McKay, Steen Moeller, Lei Zhang, Edward J Auerbach, Michael T Nelson, Patrick J Bolan

4.2.1 Introduction

DWI of the breast is typically acquired using single-shot spin-echo (SS SE) EPI. Due to the alternating nature of EPI readout (RO) lines, eddy currents, imperfect gradients, and timing errors can cause inconsistencies between k-space lines of opposite polarity (RO+/RO-), which manifest as Nyquist, or N/2, ghosts. Nyquist ghosts are often corrected by acquiring a three-line navigator to measure the difference between alternating RO lines, which is modeled as a linear phase error. While the three-line navigator generally performs well for brain imaging, it often fails in body imaging due to insufficient fat suppression and increased B_0 inhomogeneity. Several other ghost correction methods have been proposed including a full-phase navigator (112), 2D phase-mapping approaches (92–95,113–115), acceleration-based techniques (96,98,99), methods that enforce low-rank structure of multi-channel data (38,40), and a class of methods, termed referenceless methods, that use the EPI data for self-correction (40,100–103,116,117).

These referenceless methods work by defining a cost function that is minimized when the data is ghost-free. The “Entropy” method (100,101,116) uses the image entropy after a 2D Fourier Transform as a heuristic cost function. The “SVD” method (102) defines a cost function based on a singular value decomposition of k-space after rearranging into GRAPPA-like kernels. Referenceless methods may be advantageous because they do not require the acquisition of any additional navigator or reference data, potentially allowing for decreased acquisition time and/or shortened TE, and easy integration with a wide range of acquisition strategies, including retrospective data. Because these techniques do not rely on coil sensitivity profiles, they should be suitable for combination with acceleration techniques, like in-plane parallel imaging (PI) and

simultaneous multislice acquisition (SMS) (33,36,104,105); however, previous reports have suggested that the image-space-based referenceless methods may be limited by aliasing (100,102). Additionally, because they are data-driven, they may be limited by the low SNR of high b-values and high resolution DWI.

In this work we compare the performance of the standard 3-line navigator with referenceless methods for Nyquist ghost correction of breast DWI. We investigate previously proposed methods Entropy and SVD, introduce a referenceless method called Ghost/Object minimization (G/O), and assess a combination of all three. We also describe an iterative approach that allows these referenceless methods to be used in combination with PI. The methods are compared first using simulated data to assess their sensitivity to noise, and subsequently in an *in vivo* study to compare overall performance.

4.2.2 Methods

Linear ghost model and correction

Nyquist ghosts arise due to differences between k-space lines with positive and negative polarity. The phase difference is often modeled in x-k_y hybrid space as a 1st order polynomial: $\delta = \frac{\pi\kappa}{N_x}x + \phi$, where x refers to the discrete position in the RO dimension of the spatial domain, ϕ is a spatially constant phase shift between the RO+ and RO- lines, κ characterizes the slope ($\kappa = 1$ corresponds to a one pixel shift between RO+ and RO- in k-space), and N_x is the number of RO points. According to the Fourier shift theorem, and similarly described in Bernstein et al. (23), an image measured with SS SE-EPI can be described as:

$$I_{meas}(x,y) = I_0(x,y)\cos\left(\frac{\pi\kappa x}{N_x} + \phi\right) + iI_0'(x,y)\sin\left(\frac{\pi\kappa x}{N_x} + \phi\right) + \epsilon(x,y) \qquad [4.11]$$

where $I_0(x,y)$ is the ideal, ghost-free image in the RO and PE directions, respectively and $\epsilon(x,y)$ is random thermal noise. The prime operator, $'$, indicates a circular shift in the image domain such that $I_0'(x,y) = I_0\left(x, y \pm \frac{FOV}{2}\right)$. In the case of multi-shot or PE-undersampled acquisitions, Equation 4.11 becomes less straightforward; the

reconstructed image will contain multiple replicas of the object (ghosts) at locations given by:

$$I_0'(x,y) = \sum_{j=0}^{N_{seg}R-1} I_0\left(x, y \pm \frac{(2j+1)FOV}{2N_{seg}R}\right) \quad [4.12]$$

where N_{seg} is the number of segments and R is the PE-undersampling factor. The ghosts will have an additional spatially dependent signal modulation that varies with N_{seg} and sensitivity profiles.

Nyquist ghosts are commonly corrected using a three-line navigator (Method A) through $k_y = 0$ with polarity RO+/RO-/RO+. The linear phase difference between the positive and negative lines (δ) is fit in hybrid space to determine the correction parameters κ and ϕ (23,105,118). In this work, the referenceless methods were also applied as a first order correction by estimating κ and ϕ solutions that minimize the cost function $f_{cost}(\phi, \kappa)$. The cost functions were defined as follows: "Entropy" (Method B) refers to the image entropy in the spatial domain, measured using MATLAB's (MathWorks, Natick, MA) "entropy" function (100,101,116). For "SVD" (Method C), single-channel k-space was reorganized into GRAPPA-like kernels before performing singular value decomposition and summing over the tail of the singular values (102). For Method D, we propose a ghost correction called "Ghost/Object minimization" (G/O), which is described in the following section. Finally, the "Median" solution (Method E) was defined as the median of the (ϕ, κ) values from the other three referenceless methods (B, C, and D).

Ghost/Object minimization theory

The cost function for the newly proposed Ghost/Object minimization (G/O, Method D) is calculated by taking the ratio of the magnitude of the measured image over one or more shifted copies, applying a 2D median filter, and *summing over the entire ratio image* in the image domain:

$${f_{cost}}^{-1} = \sum_{x,y} F_{med\ 2D}\left(\frac{|I_{meas}(x,y)|}{|I'_{meas}(x,y)|}\right) \quad [4.13]$$

where $I'_{meas}(x,y)$ is the sum of copies of the measured image, shifted to the expected location(s) of the ghost(s) as described above. The summation is taken over the entire image and does not require selection of the object or ghost regions, however, any pixels in $I'_{meas}(x,y)$ with very low noise values may bias the cost function by adding an overly large value to the summation. Thus, a 2D median filter, $F_{med\ 2D}$, is applied to remove these outlier values. For simplicity, the summation in our implementation includes only the two ghosts ($j = 0$ and $j = R - 1$) that are located closest to the object, which tend to have the largest intensity.

While the exact value of the cost function will depend on the image, it can be shown numerically that the region of the image containing the object without any overlapping Nyquist ghost dominates the cost function when κ and ϕ are near the correct solution. Because of the sine and cosine modulation of the signal intensity in the ghost and object (Equation 4.11), the inverse cost function can be approximated as:

$$f_{cost}{}^{-1} \approx \sum_{x,y_{object}} \left|\cot\left(\frac{2\pi\kappa}{N_x} + \phi\right)\right| \qquad [4.14]$$

where the sum is taken over the region of the measured image that contains only pure object and the noise is considered negligible. Put another way, it is clear that $f_{cost}{}^{-1}$ approaches ∞ when $\phi = \kappa = 0$. Therefore, f_{cost} is minimized in the ghost-free image.

Simulation

To simulate the effect of varying noise, a synthetic image was generated in MATLAB (modified Shepp-Logan (119)) and modified with a linear ghost artifact prior to adding noise. One hundred different phase values were randomly selected, with parameters in practical ranges ($[-1.5 < \kappa < 1.5]$ and $[-0.3 < \phi < 0.3]$), and Gaussian, complex noise was added to linearly sample 25 different SNR levels for each set of ghost parameters, where $SNR = \frac{\langle S_{max}\rangle}{0.66*\sigma_{noise}}$, $\langle S_{max}\rangle$ is the mean image intensity in the region of maximum signal (the phantom rim), and σ_{noise} is the standard deviation of the noise magnitude (120). The cost functions were calculated on the noisy data for Entropy, SVD, and G/O over a multi-resolution discrete search space. The solutions for each

minimization were used to correct the simulated ghost on the noise-free data and the RMS error was measured between the ideal and ghost-corrected images and averaged over all 100 trials for each noise level.

Data acquisition

Single-shot 2D SE-EPI DWI was acquired under IRB-approved protocols from 41 female subjects including 15 clinical patients undergoing breast cancer screening (age min/med/max = 40/52/68), 13 patients with biopsy-proven cancer receiving MRI for treatment monitoring (28/47/72), and 13 healthy volunteers (18/21/66). Four subjects undergoing screening had silicone implants in one or both breasts. All subjects were positioned headfirst prone in a Siemens Prisma^{fit} 3T scanner using a 16-channel Sentinelle breast coil. Diffusion images were acquired following the protocol used in the clinical trial ACRIN 6698, with TR = 8000 ms and TE 51 ms for monopolar diffusion (12 participants) or 74 ms for bipolar diffusion (29 participants), 36-50 4 mm axial slices with 320 x 320 mm in-plane FOV at 1.7 x 1.7 mm resolution, right-left phase encoding, in-plane undersampling of R = 3, 6/8 partial Fourier, SPAIR fat suppression, and total acquisition time ~5 minutes (121). One of the following three diffusion schemes was used to sample three orthogonal diffusion directions for each subject: b = 0, 100, 600, and 800 s/mm^2 (5, 9, 9, 9 averages = 32 volumes) [21 participants]; b = 0, 100, 600, and 800 s/mm^2 (4, 6, 6, 6 averages = 22 volumes) [5 participants]; b = 0, 100, and 800 s/mm^2 (5, 9, 9 averages = 23 volumes) [15 participants]. A 3-line navigator was acquired with phase encoding disabled for each coil, slice, and b-value/diffusion direction and for both the autocalibration scan (ACS lines) and undersampled data.

T_1-weighted anatomical images were acquired using a 3D VIBE sequence (RF-spoiled, 3D gradient echo) with fat suppression.

Image reconstruction and ghost correction

Both ACS lines and undersampled data were reconstructed off-line with per-acquisition, per-coil, and per-slice ghost correction, followed by GRAPPA unaliasing (30). For the 3-line navigator correction (Method A), the phase difference between the center line and average of the 1st and 3rd lines of each navigator was smoothed with a Savitzkey-Golay

filter (sgolay, MATLAB), weighted by the signal intensity to the fourth power, and fit to a first-order polynomial in x-k_y hybrid space.

The referenceless methods were first applied to the low-resolution ACS lines using a multi-resolution discrete search centered at $\phi = 0$ and $\kappa = 0.6$ in MATALB to determine ϕ_{ACS} and κ_{ACS}. The corrected ACS lines were used to calculate the GRAPPA weights. ϕ_{ACS} and κ_{ACS} were also applied as an initial correction for the undersampled diffusion-weighted data; to refine ϕ and κ a second iteration was performed using a non-linear minimization (fminsearch) including GRAPPA unaliasing in each step: i.e. a candidate(ϕ, κ) correction was performed on each channel of the undersampled data before GRAPPA unaliasing so the cost function could be evaluated on the unaliased reconstructed image.

Method D (Median) consisted of a combination of the four referenceless methods by taking the median of ϕ and κ from each method to reconstruct both ACS and undersampled data.

Assuming a monoexponential decay diffusion model, ADC maps were generated using a pixel-by-pixel linear fit of the natural log of the signal intensity across b-values.

Analysis

Due to the N/2 nature of Nyquist ghosts, R = 3 undersampling, and symmetric anatomy of axial breasts images, a large portion of the residual ghosts falls along the midline between the right and left breasts (Figure 4.4). Thus, the signal level of the background region was used as a surrogate measurement of the ghost level in the full image. To measure the signal in the background region, the T_1-weighted anatomical image was resampled to match the DWI image matrix, thresholded, and dilated to automatically create a mask of object and background; all area posterior to the chest wall was automatically classified as object. We also measured the noise level for each case based on the average signal intensity of noise-only corner regions of the volume (Figure 4.4). We defined the ghost intensity for each method, acquisition, and subject over the whole volume as the average signal in the background region compared to the average noise level.

Figure 4.4 – Measurement of ghost levels
Nyquist ghosts in a b = 0 s/mm^2 image (A) can be seen in the background region between the breasts. The T_1-weigthed anatomical image (B) is used to create an object mask, which is applied to the b = 0 s/mm^2 image (C). The signal in the background region (D) reflects the intensity of the residual ghost. Red boxes indicate the regions used to measure the average noise level in root sum of squares images.

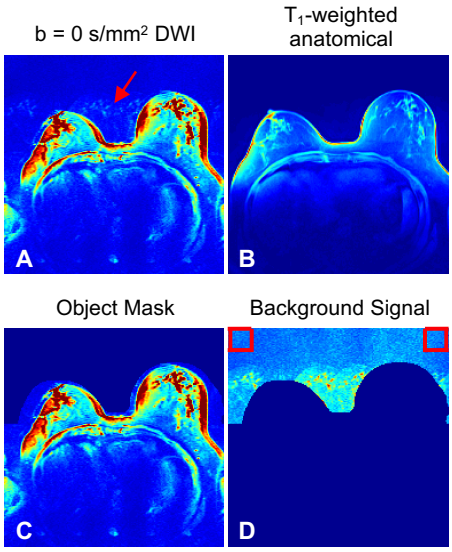

To compare the ghost correction performance, the whole-volume ghost measurements were averaged for each subject across averages at each b-value, and then a linear mixed model was applied with ghost correction method, b-value, and their interaction as covariates, adjusting for body mass index (BMI). A pairwise comparison was made between each correction method based on the model-estimated ghost intensity. To control type I error for multiple comparisons, Bonferroni correction was applied, and a two-sided p-value < 0.005 (0.05/10) was considered statistically significant for pairwise comparisons among five methods. The ghost intensity estimates were also compared between methods on a per-b-value basis in a pairwise way; statistical significance was set to $P < 0.00125$ (0.05/40) based on Bonferroni correction. SAS system (version 9.4; SAS Institute, Cary, North Carolina) was used in all statistical analyses.

4.2.3 Results

Figure 4.5 demonstrates the performance of the referenceless methods with increasing levels of SNR. While the error increases at lower levels of SNR for all four methods, all four referenceless methods are tolerant to noise down to an SNR levels of about 3–5;

entropy is most sensitive to noise, followed by SVD, Median, and finally G/O. This sensitivity is reflected in the shape of the cost functions (example in Figure 4.5 inset). As SNR decreases, the minimum regions spread out and additional local minima develop that do not correspond to the ghost-free image, especially for Entropy and SVD. While all three referenceless cost functions have clear global minima at low noise levels, the cost functions vary in shape, especially as the noise level increases, suggesting that they each contain some unique information.

Figure 4.5. Simulation of noise effect on cost functions
This plot shows the accuracy of each method, averaged over 100 trials, for increasing SNR levels. Example images are shown for 4 (of 25 tested) sample SNR values. The inset plots show the cost functions for a single trial at two SNR levels, indicated on the x-axis by * and °. With decreasing SNR, additional local minima develop, and minimum regions spread out. White and red circles indicate the correct and estimated ghost parameters, respectively.

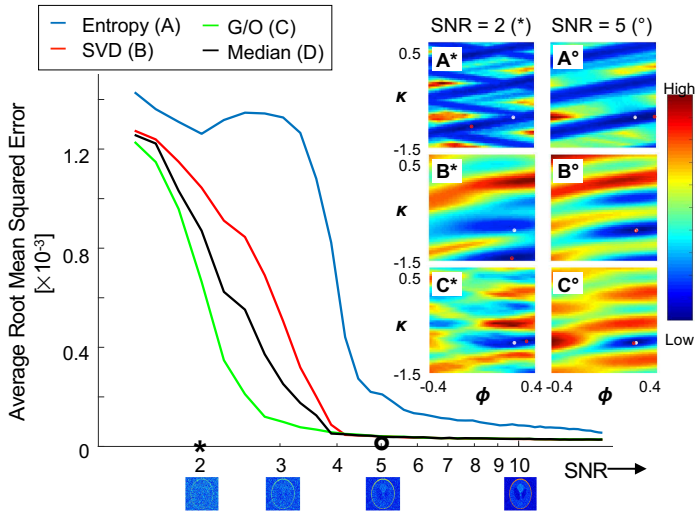

The performance of all five ghost correction methods varied across cases and slices. The 3-line navigator tended to fail more frequently than the referenceless methods in the 41 breast cases tested. An example is shown in Figure 4.6 that represents a typical case where the 3-line navigator failed and the referenceless methods significantly reduced the ghost at both b = 0 and b = 800 s/mm^2, as well as the resulting ADC map.

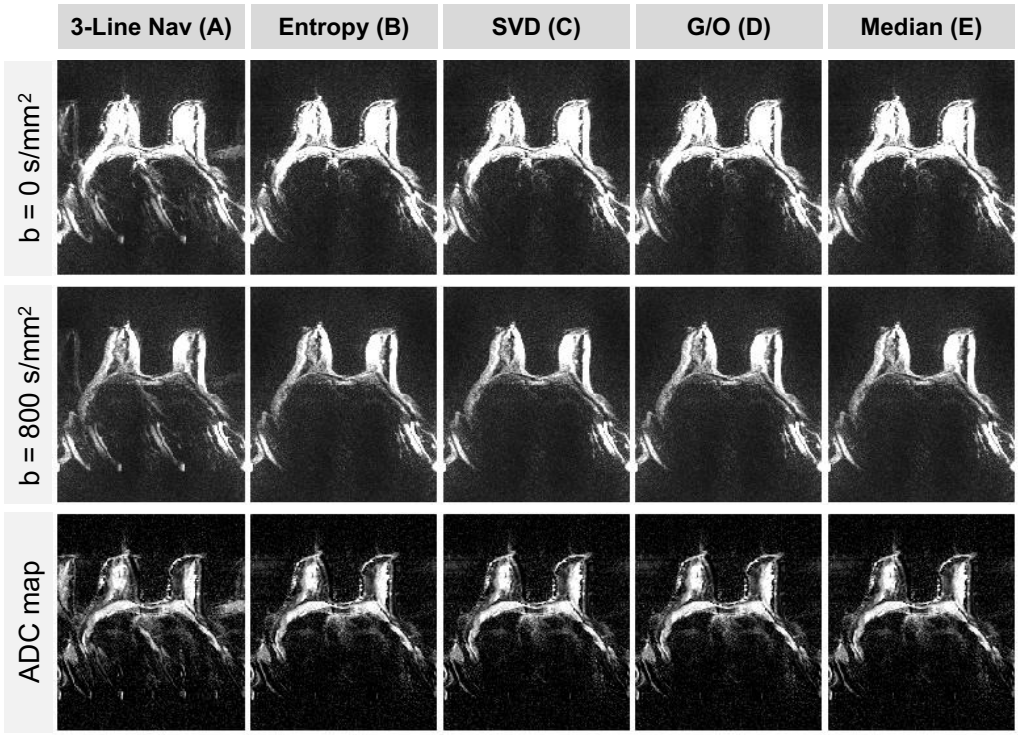

Figure 4.6. Single-slice DWI from two example cases
A single acquisition of b = 0 and 800 s/mm² images and an ADC map are shown. The example is chosen as a representative case in which the referenceless methods outperform the 3-line navigator. Scaled to highlight Nyquist ghosts.

The overall effects of ghost correction method are shown in Figure 4.7, which plots the ghost intensities measured over the whole volume for each subject and acquisition. The mean ghost levels estimated according to the adjusted linear mixed model are overlaid including 95% confidence intervals. All four referenceless methods generally reduce ghost levels compared to the standard approach. According to the adjusted linear mixed model, the performance of all four referenceless methods (B-E) is statistically superior ($p \leq 0.0002$) to the standard linear correction (A). While there is no statistical difference between the performance of the entropy, SVD, and G/O referenceless methods (B-D), the median combination of referenceless methods (E) is estimated to significantly outperform any single referenceless method alone ($p < 0.0001$).

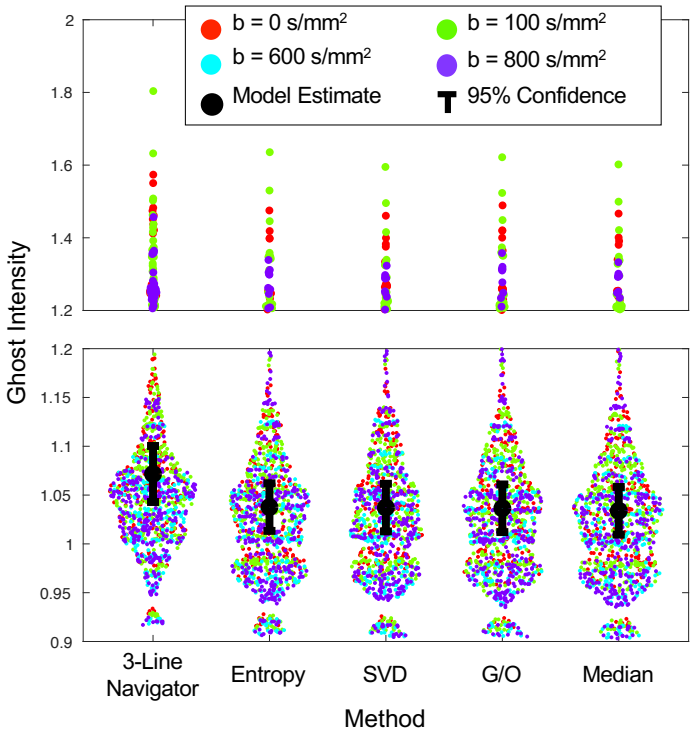

Figure 4.7 – Whole-volume ghost intensity plotted over method
Colored points indicate ghost intensity measured over the volume of each subject and acquisition; color indicates b-value. The black circles indicate the ghost intensities estimated according to the adjusted linear mixed model with 95% confidence intervals. Plotted over two y-scales for detail.

The mean ghost intensities for each method separated by b-value according to the full linear mixed model are plotted in Figure 4.8; *p*-values less than 0.00125 are indicated. The mean ghost intensity of all referenceless methods (B-E) is lower than that of the standard 3-line navigator at all four b-values ($P < 0.001$). The differences between entropy, SVD, and G/O referenceless methods are not statistically significant regardless of b-value. The median method (E) yields the lowest ghost intensity value at all four b-values, however, E only outperforms B-C with statistical significance compared to Entropy and SVD at b = 0 s/mm^2 and to Entropy at b = 100 and 800 s/mm^2.

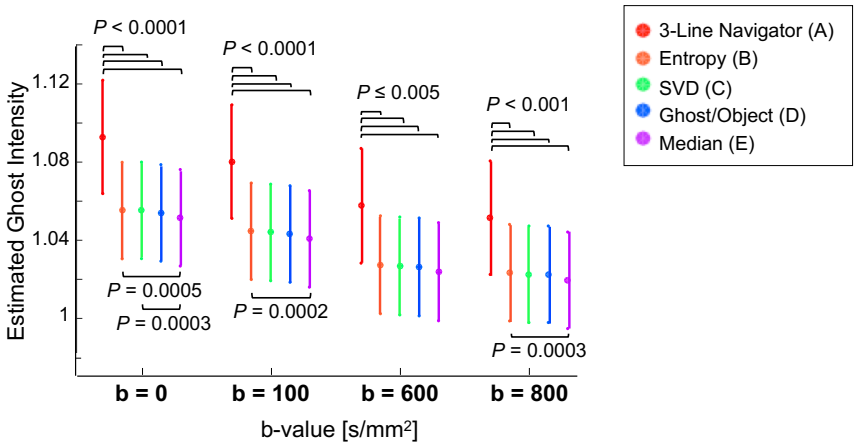

Figure 4.8 – Ghost intensity by method and b-value
Ghost intensity and its 95% confidence interval estimated by the linear mixed model given b-value and ghost correction method. Threshold for statistical significance is set to $P < 0.00125$ based on Bonferroni's method for multiple comparisons.

4.2.4 Discussion

One potential source of Nyquist ghosts is eddy currents induced by the diffusion gradients. The 3-line navigator is independent of b-value because it is acquired before diffusion weighting is applied and cannot correct for eddy currents caused by the diffusion gradients. The referenceless methods depend on the diffusion-weighted data and do include effects from the diffusion gradients, but they may be more sensitive to the signal loss at high b-values. We have shown here, however, that all four referenceless methods perform well in low SNR down to ~3-5 in simulated phantom data and outperform the 3-line navigator at all four b-values up to b = 800 s/mm^2. If used for images with even lower SNR (e.g. very high resolution or large b-values), adding additional denoising filters could improve the performance of all the referenceless methods.

All five ghost correction methods estimated and applied two linear parameters on a per-coil, per-slice, and per-acquisition basis. In a small number of cases none of the ghost correction methods fully suppress the ghost, suggesting that it may be necessary to use higher-order correction. The referenceless methods may be extended to include higher-order parameters or correction that varies over the RO train if the necessary

correction can be modeled by a small number of parameters. However, the computational time will quickly grow as the model increases in complexity.

The referenceless methods represent a data-driven approach to correct Nyquist ghosts. They can be applied retrospectively to a wide variety of data acquisitions without the need for any additional reference scan as methods like phase labeling for additional coordinate encoding (PLACE) and phase mapping require (92–95,113–115). Ghost correction by referenceless methods also does not rely on coil-sensitivity profiles, as methods like phase array ghost elimination (PAGE) do (96,98,99), and therefore preserve all information about coil-sensitivity for the purpose of maximizing acceleration. Additionally, by removing the three-line navigator, it may be possible to shorten the TE. However, one limitation of the referenceless methods is the increased computational requirement for optimization of the nonlinear cost functions. In our implementation, SVD is the slowest referenceless method; a full static SVD reconstruction takes about 1.3 times longer than the three-line navigator correction and further increases to about 100 (G/O) to 300 (SVD) times when the iterative approach, which includes GRAPPA unaliasing in the cost function minimization, is used to determine dynamic corrections. It should be possible to reduce computation requirements to clinically practical times with further optimization of the processing.

While the summation in Equation 4.13 is performed over the entire image, the cost function is dominated by the object-only region due to the sine and cosine signal modulation. While the method does not explicitly select regions of interest, it could be limited by the amount of object/ghost overlap if the object lacks signal variation in the PE direction, which would flatten the shape of $f_{cost}(\phi, \kappa)$. Additionally, G/O requires the removal of outlier values prior to taking the summation, which is not necessary for Entropy or SVD. In this implementation we removed these outliers by applying a 2D median filter, which also produces some denoising in $f_{cost}(\phi, \kappa)$. While this filtering does add a small bias to the comparison of the referenceless methods, median filtering did not improve the entropy metric in our data and cannot be used with SVD as it requires complex data. However, all of the methods used, including the linear navigator,

may be further optimized using other denoising techniques (e.g. Gaussian) and additional tuning.

Previous reports have claimed that referenceless methods performed in the image domain were limited by the amount of overlap and aliasing that arise when acceleration techniques or multi-shot acquisition are used (100,102). In this work, we overcome the limitation of PE undersampling by incorporating the GRAPPA reconstruction in the optimization; this strategy may be useful in combination with other acceleration methods as well.

Nyquist ghost artifacts can modulate the true image signal and lead to errors in ADC estimation via two distinct mechanisms. The first is simple overlap – if any portion of a Nyquist ghost overlaps the object it can increase or decrease the object signal. Secondly, an incorrect phase produces a spatially varying cosine modulation of the object signal (Equation 4.11). In this work we used the ghost signal in the image background as an estimate of the overall ghost level. Although ghost signal in the image background does not directly produce ADC errors, it is an objective measure of the overall ghost level.

In this study, we used the 3-line navigator as the reference standard ghost correction method. Our implementation of this method gives somewhat different results than the vendor's proprietary implementation, but the average performance of the two implementations is similar.

4.2.5 Conclusions

Referenceless methods provide a data-based alternative to the three-line navigator for 1st-order ghost correction, which often fails in breast DWI. We proposed an additional referenceless method, Ghost/Object (G/O) minimization, which defines a cost function in the image domain that exploits the cosine and sine modulation in the ghosted image and the N/2 nature of the ghost. All four referenceless methods show low sensitivity to noise levels, especially G/O and SVD in a simulation at increasing noise levels and perform well at b-values up to 800 s/mm^2. In this work, all three referenceless methods were successfully combined with accelerated imaging of R = 3 and outperformed the 3-line

navigator correction at all four b-values. Additionally, because each of the three cost functions employed contain some unique information, combining the referenceless methods with the median of 1st-order parameters showed a trend of improved ghost correction performance.

4.3 Nyquist Ghost Correction of SMS Imaging using Referenceless Methods

While developing and assessing ghost correction in SB data, we simultaneously worked to improve resolution using simultaneous multislice (SMS), described in more detail in Chapter 5. Thus, as a natural extension of Section 4.2, the referenceless methods were assessed in SMS data in this work. The following was previously presented as part of an electronic poster entitled *Nyquist Ghost Correction of High-Resolution SMS Breast DWI with Ghost/Object Minimization* at ISMRM 27th Annual Meeting and Exhibition. Montreal, Quebec; May 2019. Abstract #3354.

Jessica A McKay, Steen Moeller, Sudhir Ramanna, An L Church, Michael T Nelson, Edward J Auerbach, Kamil Ugurbil, and Patrick J Bolan

4.3.1 Introduction

Diffusion weighted imaging (DWI) is increasingly used in breast cancer imaging because low apparent diffusion coefficients (ADCs) indicate malignancy. However, the ability to detect lesions is extremely limited by the low resolution of typical single-shot spin-echo (SS SE) EPI. We recently developed a simultaneous multi-slice (SMS) (33) approach to SS SE-EPI for breast DWI that was derived from the Human Connectome Project's (HCP) (122) high-resolution protocol.

In EPI, eddy currents and timing errors cause inconsistencies between the positive and negative readout lines (RO+/RO-) that manifest as Nyquist ghosts in the phase encoding (PE) direction of the image. These ghosts can obstruct the visualization of the DW images and bias ADC values. Ghosts are typically corrected using a 3-line navigator, which generally works reliably in HCP brain imaging, but often fails in high-resolution SMS breast DWI due to insufficient SNR, fat suppression, and B_0 homogeneity.

Moreover, ghost correction failure in autocalibration scans (ACS) propagates in the SMS and GRAPPA reconstructions that are often employed in high resolution imaging.

One class of alternative ghost correction strategies are referenceless. which are conveniently applied without the need for additional data (100–102). Ghost/Object minimization (G/O) (108) is one such referenceless method, that minimizes a cost function in the image domain. *The purpose of this work is to apply reduce residual ghosts in high-resolution breast DWI acquired with SMS SE-EPI using G/O to correct 1st order ghosts.*

4.3.2 Methods

Acquisition

Sixteen breast cancer patients were scanned prone on a Siemens 3 T Prisma^{fit} with a 16-channel breast coil (Sentinelle) under an IRB-approved protocol. DWI was acquired using 2D SE-EPI with 256 sagittal slices of 1.25 mm with SMS MB = 4, which are reformatted to axial images for clinical viewing. The following parameters were used: TR/TE = 6500/60.80 ms, 1.25 mm x 2.5 mm nominal in-plane resolution, head/foot PE direction, GRAPPA R = 2, and monopolar diffusion (4 at b = 0, 4 at b = 800 s/mm^2). Standard T_1-weighted anatomical images were also acquired.

Ghost correction

Two first-order ghost correction methods were applied offline to both the ACS data and each undersampled acquisition on a per-channel and per-slice basis. The 3-line navigator, which represents typical online correction, acquires a navigator through $k_y = 0$ (RO+/RO-/RO+) to measure the phase difference. G/O minimization was performed directly on ACS and undersampled data, starting with a wide discrete search and refined with a simplex search. After SMS unaliasing, the ghost correction was adjusted in a slice-specific way, statically for the 3-line navigator (based on the difference between ACS and MB navigators) and dynamically for G/O (based on a second iteration of the minimization problem). To improve GRAPPA unaliasing performance, original ACS

data was combined with RO-reversed ACS data to reduce ghosts before calculating weights.

Analysis

The residual ghost levels were measured based on the signal in the background region. T_1-weighted images were automatically masked and resampled onto the DWI to define the object region (Figure 4.9). The ghost signal was measured as the whole-volume background signal compared to the average signal in a noise-only volume (Figure 4.9).

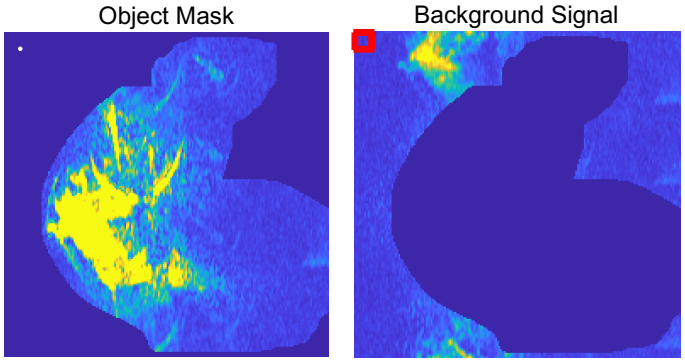

Figure 4.9 – Object mask and background ghost in SMS
Example of object mask overlaid on b = 0 s/mm^2 image corrected by the 3-line navigator. The ghost intensity is defined as the total background signal compared to the signal in a noise-only region (red box).

4.3.3 Results

Two examples of *in vivo* b = 0 and 800 s/mm^2 images are shown in Figures 4.10 and 4.11. In Figure 4.10, the 3-line navigator clearly fails, causing Nyquist ghosts and poor GRAPPA unaliasing performance. Small levels of GRAPPA errors are also present in G/O images. Figure 4.11 demonstrate how the artifacts in the PE direction influence the SMS unaliasing performance and overall axial image quality. Several artifacts are present in the slice dimension after correction by 3-line navigator, which are greatly reduced by G/O.

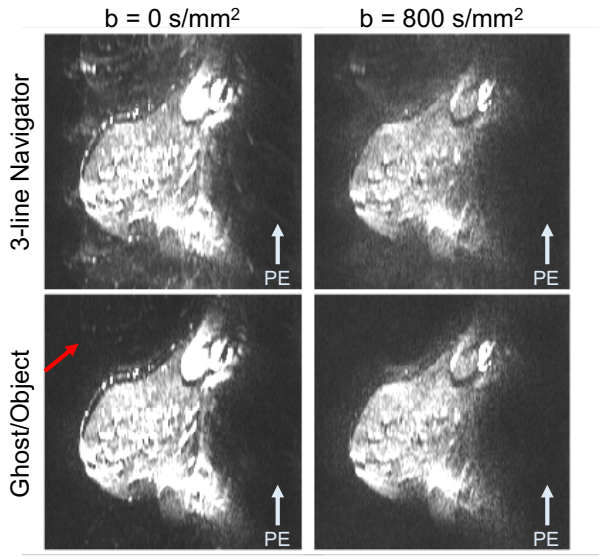

Figure 4.10 – Ghost correction in SMS example case
b = 0 and 800 s/mm^2 images from an example case with moderate 3-line navigator failure. Nyquist ghosts and GRAPPA aliasing are present in 3-line navigator case, where only slight GRAPPA artifacts are present in G/O.

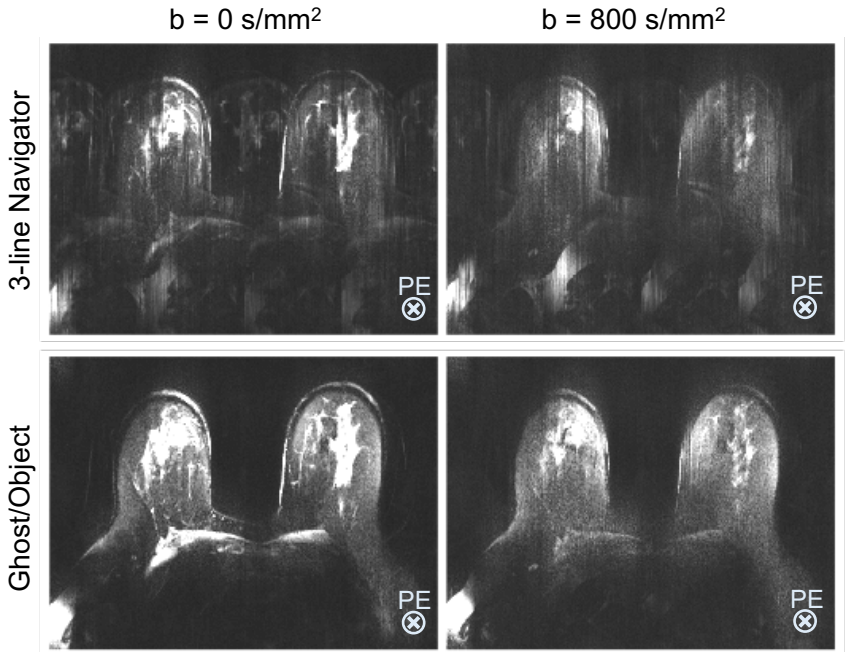

Figure 4.11 – Ghost correction in SMS example case 2
b = 0 and 800 s/mm^2 images (4 averages each) from a center axial slice. Note that the PE direction is through plane, however poor Nyquist ghost correction affects the overall axial image quality and the performance of SMS unaliasing.

The ghost intensity of G/O is plotted versus the 3-line navigator in Figure 4.12 for each acquisition. For all cases, G/O either performs equivalently (on the line) or outperforms (to the right of the line) the standard 3-line navigator.

Figure 4.12 – Ghost comparison in SMS
Ghost intensity comparison between Ghost/Object and 3-line navigator. Points on the line indicate similar ghost correction performance. Points to the right of the line indicate cases where G/O outperformed the standard 3-line navigator.

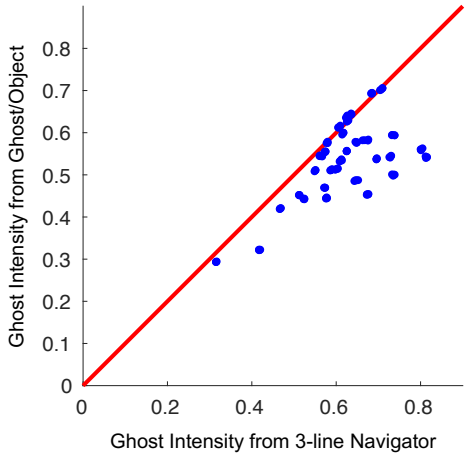

The ghost intensities are plotted separated by b-value in Figure 4.13. According to a paired t-test (N = 16) there is a significant difference between the performance of G/O and the 3-line navigator at both b = 0 and b = 800 s/mm^2.

4.3.4 Discussion

The G/O method does not rely on any reference data and was applied directly to both R = 2 undersampled data and SMS data after unaliasing, allowing for a completely dynamic and slice-specific correction.

In this work the background signal acts as a surrogate for ghost intensity. The background includes both Nyquist ghosts and GRAPPA unaliasing artifacts, which are often caused by the poor ghost correction of ACS lines. Some unaliasing artifacts were present in both G/O and 3-line navigator reconstruction. Importantly, Nyquist ghosts in the background region imply a signal change in the object and ghost that may overlap the

object, biasing the ADC values. Moreover, severe ghost failures make image interpretation difficult.

Figure 4.13 – Ghost intensities by b-value
P-values indicate statistical significance from paired t-test (N = 16) at each b-value. Overall, Ghost/Object yields lower ghost values than the 3-line navigator with statistical significance at both b-values.

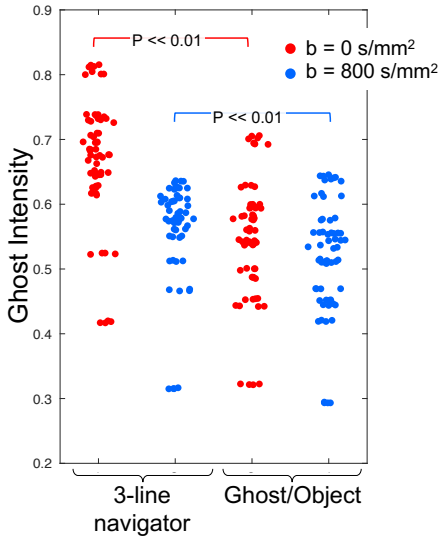

4.3.5 Conclusions

The standard 3-line navigator is insufficient for ghost correction of high resolution, breast SE-EPI DWI with SMS. The alternative G/O referenceless method provides more reliable 1st-order ghost correction in a dynamic and slice-specific way, which improves image quality and reduces bias in ADC values compared to the standard correction.

Chapter 5: Use of SMS for High Resolution Breast DWI

5.1 The AR-SMS Approach

Typical breast DWI is acquired axially as most radiologists prefer to view bilateral axial images. Usually, PE is in the Right/Left direction to avoid aliasing from the chest wall and abdomen where there is cardiac and respiratory motion. However, phase encoding provides the lowest quality encoding in EPI (see Section 2.1). Thus, it is advantageous to acquire sagittal slices and reformat to axial images such that the PE direction is through plane in the resulting axial images where it will be least disruptive to the reading, as shown in Figure 5.1. This approach is referred to as axially reformatted (AR). Similarly, T_2-weighted and contrast enhanced T_1-weighted anatomical images are typically acquired with thick axial slices and/or slice gaps, prioritizing higher in-plane resolution in a given scan time.

Figure 5.1 – Axially-reformatted SMS approach
b = 0 s/mm^2 images are shown to explain the acquisition strategy. Sagittal images are acquired with MB = 4 and reformatted to axial images for viewing.

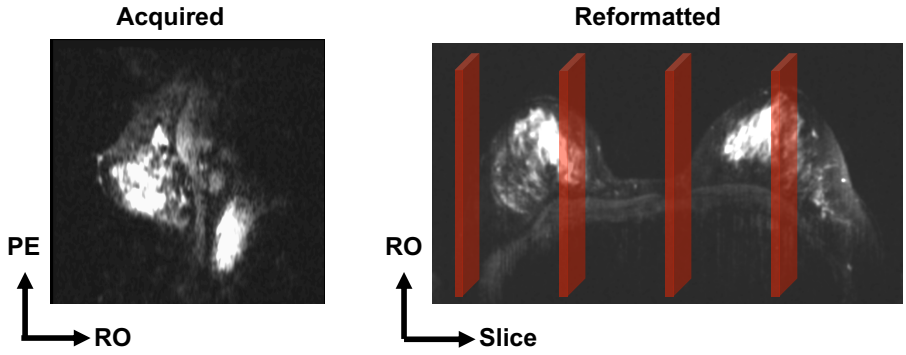

To acquire sagittal slices, however, with high axial resolution requires very thin slices and thus a very high number of slices to cover the whole Right/Left direction. Fortunately, SMS imaging has seen significant advancements in the recent past, including the Human Connectome Project (HCP) and many other efforts. In this work we adapted the HCP methods, developed for brain imaging, for breast DWI. With SMS it is possible to acquire a large number of very thin slices in a reasonable scan time.

In this approach, an SMS acceleration of 4x is used to achieve 1.25 mm (RO and Anterior/Posterior) x 1.25 mm (slice and Right/Left) x 2.5 mm (PE and Head/Foot) resolution. Four averages at b = 0 s/mm^2 and 24 at b = 800 s/mm^2 in three directions are acquired within a 5-minute scan time. An example of the improved resolution is shown in Figure 5.2, which highlights the improved lesion conspicuity achieved in this case.

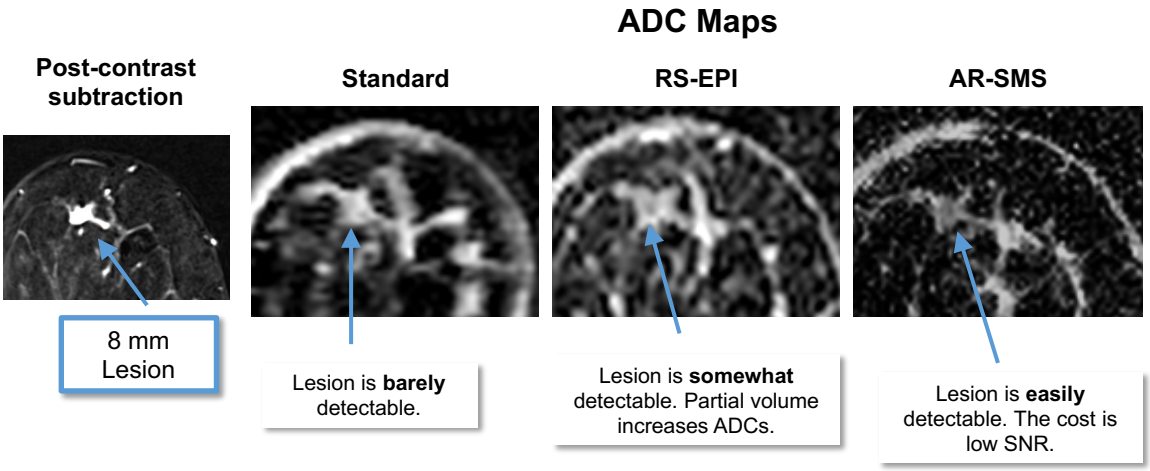

Figure 5.2 – Lesion conspicuity example
ADC maps zoomed into lesion and compared with post-contrast. Higher resolution increases the ability to detect and measure the lesion on the ADC map.

5.1.1 Topup distortion correction

While AR-SMS efficiently achieves full coverage and high resolution, one disadvantage is that SMS acceleration does not reduce geometric distortion as in-plane undersampling and segmentation do. Thus, we employed FSL's topup distortion correction (24). For the topup correction, the acquisition of fully sampled reference data (b = 0 s/mm^2) is repeated with reversed phase encoding, which produces equal and opposite distortion used to estimate the inhomogeneity of B_0. The distortion map is then applied to each subsequent acquisition, including those that are diffusion weighted.

Examples of phantom and *in vivo* topup distortion correction are presented in Figures 5.3 and 5.4. While the distortion is significantly reduced, there is still noticeable residual distortion. Topup relies on a few assumptions that are violated in breast imaging. For one, the correction is static and does not account for any B_0 changes throughout the

scan caused by respiratory motion or unintentional movement of the participant. Second, the B_0 field is considered to be slowly and smoothly varying, which is often violated in breast imaging, especially at interfaces between skin and air. Moreover, the topup model does not account for the presence of fat, which can add large discontinuities in the resonance frequency measured.

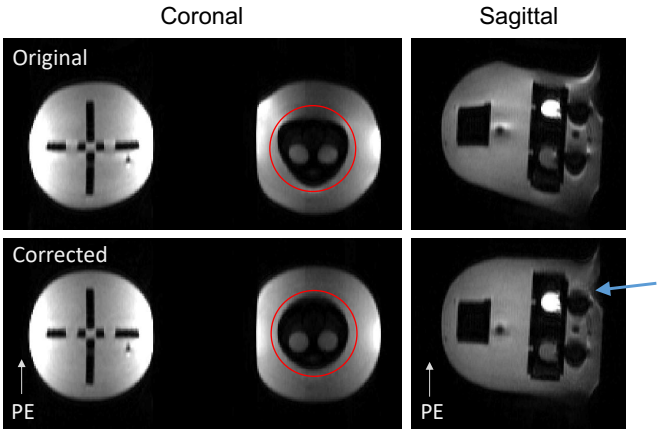

Figure 5.3 – Topup example in phantom
b = 0 s/mm^2 images of breast phantom before and after topup correction. PE distortion is clearly seen in the PE direction, highlighted by the red circle. While topup greatly reduces the distortion, there is some residual distortion (blue arrow)

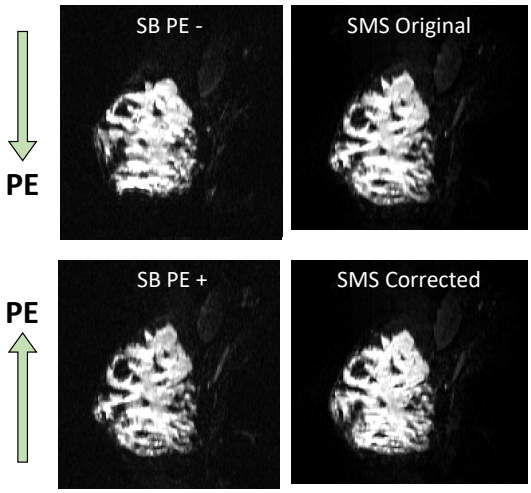

Figure 5.4 – Topup example *in vivo*
Sagittal b = 0 s/mm^2 images of reference data and SMS data with and without correction. The distortion map is calculated from the SB reference data, acquired twice with reversed PE, and applied to the SMS data. The distortion is reduced, especially near the nipple (blue arrow)

5.2 A Comparison of Methods for High Spatial Resolution DWI in Breast MRI

After combining SMS, referenceless Nyquist ghost correction, and topup distortion correction, the image quality was assessed in the clinically setting in the following. This work was submitted with revisions on May 14, 2020 to *Radiology* and is on an acceptance track. Jessica A McKay, An L Church, Nathan Rubin, Tim H Emory, Noelle F Hoven, Jessica E Kuehn-Hajder, Michael T Nelson, Sudhir Ramanna, Edward J Auerbach, Steen Moeller, and Patrick J Bolan

5.2.1 Introduction

Diffusion-weighted imaging (DWI) measures the apparent diffusion coefficient (ADC) of tissue, which is often lower due to cancer. There is growing interest in using DWI for breast cancer imaging for screening, disease characterization, and monitoring treatment response (67). DWI is typically acquired using single-shot spin-echo echo planar imaging (SE-EPI), which faces several challenges often exacerbated in breast imaging due to the large field of view, adipose signal, and respiratory motion that alters the B_0 field. Standard breast DWI suffers from very low spatial resolution, large geometric distortions, chemical shift artifacts, and Nyquist ghost artifacts, which can limit its clinical value. Higher resolution may also enable the use of DWI for additional analyses, including minimum ADC, DWI radiomics, histogram analysis, rim sign etc. (123,124).

Several strategies to improve the image quality of SE-EPI in breast DWI have been explored, including readout-segmentation (RS) (47–50), reduced field of view (52,53), and multiband encoding in the phase encoding direction (125). A proposed strategy uses simultaneous multislice (SMS) imaging (33,36,104) to improve image quality in breast DWI (110,126,127). Because the SMS potential is greater in the right/left direction based on the coil geometry, this approach acquires sagittal images with aggressive SMS to cover a large volume with many thin slices. The images are axially reformatted (AR) for interpretation, according to standard clinical practice. Thus, the axial images are encoded by the readout and slice directions, which provides high in-

plane resolution whereas the blurred and artifact-prone phase encoding direction is rotated through-plane.

In this study, we compared the image quality and resolution of standard SE-EPI breast DWI with two high-resolution imaging protocols based on RS-EPI and AR-SMS, with each optimized to provide full bilateral coverage in a clinically acceptable (<5 minute) scan time. The three protocols were characterized with phantom resolution measurements and *in vivo* performance was assessed using a multireader study.

5.2.2 Materials and methods

Study participants

In this prospective, IRB-approved and HIPPA-compliant study, women undergoing clinical breast MRI at our imaging center were offered additional diffusion scanning to be acquired after their clinical scan between December 2016 and December 2018. Participants were receiving breast MRI either as part of a treatment response clinical trial (Investigation of Serial Studies to Predict Your Therapeutic Response with Imaging And moLecular analysis 2 (I-SPY 2 Trial)) or clinical MRI for screening or suspected cancer and provided written informed consent. Data from I-SPY 2 may be included in other studies (clinicaltrials.gov NCT01042379, NCT02058758), excluding RS-EPI and AR-SMS.

Phantom acquisition for resolution assessment

A commercial breast phantom (Model 131, CaliberMRI, Boulder, CO) based on [Ref (128)] with a resolution test grid was scanned with all DWI protocols. The phantom was rotated to assess the resolution in each plane. Feature detection was subjectively assessed by two MR physicists (JM and PB).

MRI acquisition

All images were acquired on 3 T Siemens Prisma^{fit} scanners (Siemens Healthcare/Healthineers, Erlangen, Germany) using a 16-channel Sentinelle breast coil (Philips Medical Systems, Hamburg, Germany). For every participant, standard MRI

were acquired, including T_2-weighted and a contrast-enhanced (CE) T_1-weighted series with an intravenous injection of gadolinium-based contrast agent (gadobutrol, 0.1 mM/kg). RS-EPI and AR-SMS were acquired after clinical imaging was completed. See Supplemental Materials for details.

Three different SE-EPI strategies were used to acquire bilateral breast DWI. While not fixed in resolution or volumetric coverage, each protocol was individually optimized for a 5-minute scan time. The first, *Standard-A*, represented the standard clinically available breast MRI, using single-shot SE-EPI, compliant with the ACRIN 6698 clinical trial (11,121) with nominal resolution 1.7 mm x 1.7 mm x 4 mm. Due to time restrictions of clinical scanning, a shorter version, *Standard-B*, with fewer b-values was used for participants undergoing clinical breast MRI (non-trial). The vendor's implementation was used for RS-EPI with protocol parameters based on Wisner et al. (48), chosen for its high and nearly isotropic resolution, with 5 readout segments and 1.8 mm x 1.8 mm x 2.4 mm nominal resolution. AR-SMS was implemented by modifying the custom SMS EPI acquisition and reconstruction pipeline developed for the Human Connectome Project (129). The AR-SMS acquisition used 4x slice acceleration for 1.25 mm isotropic axial resolution and 2.5 mm through plane (phase encoding) interpolated to 1.25 mm, and included an additional reference scan with opposite phase encoding for geometric distortion correction (130). See Table 5.1 for protocol details.

Preparing data set for reader analysis

Digital Imaging and Communications in Medicine (DICOM) images were generated online for clinical scans, and standard SE-EPI and RS-EPI DWI. AR-SMS reconstruction was performed offline in MATLAB R2017b (MathWorks, Natick, MA) using in-house reconstruction; see Supplemental Materials for details. All images were transferred to a clinical PACS system (iSite, Philips Healthcare, Andover, MA) for analysis.

For each participant, a single study was chosen with preference for pre-treatment scans when available. Using T_2-weighted and CE-subtraction images, all enhancing, mass-like lesions within each DWI field of view were identified and measured in length.

The largest lesion from every woman was included, and secondary lesions from distant slices were included from two women.

Table 5.1 – Acquisition parameters
Standard-A was used for participants of I-SPY 2 clinical trial; Standard-B, with fewer b-values, was used for clinical participants not enrolled in I-SPY 2 to reduce total scan time. All participants were additionally scanned with RS-EPI and AR-SMS.

Protocol	DWI				Clinical		
	Standard SE-EPI		RS-EPI	AR-SMS	T_2-weighted	Contrast-enhanced T_1-weighted	
	Standard-A	Standard-B				I-SPY 2 (Standard-A)	Clinical (Standard-B)
Type	Single shot SE-EPI		SE-EPI with 5 RO segments	Single shot SE-EPI	SE	3D gradient echo	
TR / TE [ms]	8000 / 74.0		7800 / 64.0	6500 / 60.80	4500 / 72	4.72/1.82	
PE / orientation	R/L / Axial		A/P / Axial	H/F / Sagittal	R/L / Axial	R/L / Axial	
Echo spacing	0.74 ms		0.32 ms	0.93 ms	N/A	N/A	
Number of echoes acquired	48		43	38	N/A	N/A	
b-values [s/mm^2] (directions/ averages)	0 (5) 100 (9) 600 (9) 800 (9)	0 (5) 100 (9) 800 (9)	0 (3) 800 (6)	0 (4) 800 (24)	-- (1 avg)	-- (1 avg)	
Diffusion scheme	Bipolar		Bipolar	Monopolar	--	--	
Nominal resolution (RO x PE)	1.7 mm x 1.7 mm		1.8 mm x 1.8 mm	1.25 mm x 2.5 mm	0.8 mm x 0.8 mm	0.6 mm x 0.6 mm	
FOV/Coverage [mm] (R/L, A/P, H/F)	320 (PE) x 320 (RO) x 144-176 (slice)		350 (RO) x 156 (PE) x 134.4 (slice)	320 (slice) x 240 (RO) x 240 (PE)	320 (PE) x 320 (RO) x 198 (slice)	300-340 (PE) x 300-340 (RO) x 208 (slice)	
Slice number Slice thickness Slice gap	36-44 slices 4 mm 0 mm	44 slices 4 mm 0 mm	56 slices 2.4 mm 0 mm	256 slices 1.25 mm 0 mm	60 slices 3.0 mm 0.3 mm	160 slices (1 slab) 1.3 mm --	
GRAPPA	R = 3		R = 2	R = 2	R = 2	R = 3	
SMS	--		--	MB = 4 (R/L)	--	--	
Partial Fourier	6/8 phase		none	6/8 phase	--	6/8 phase, 6/8 slice	
Acquisition Time [min:sec]	4:58		4:58	4:52	4:59	7 timepoints, 1:32 each	4 timepoints, 1:58 each

Reader analysis

Two lesions of different sizes were used for training the breast radiologists. The remaining lesions were independently presented to three radiologists (TE, NH, and JKH with 19, 3, and 14 years of breast MRI experience, respectively) in random order in one or two (separated by <7 days) sessions. The radiologists were blinded to the participant and the DWI method. For each lesion, the radiologists were provided with clinical images, b = 800 s/mm^2 images, and ADC maps from all three DWI methods, presented axially in random order. The lesion was indicated on the CE-subtraction, as shown in Figure 5.5.

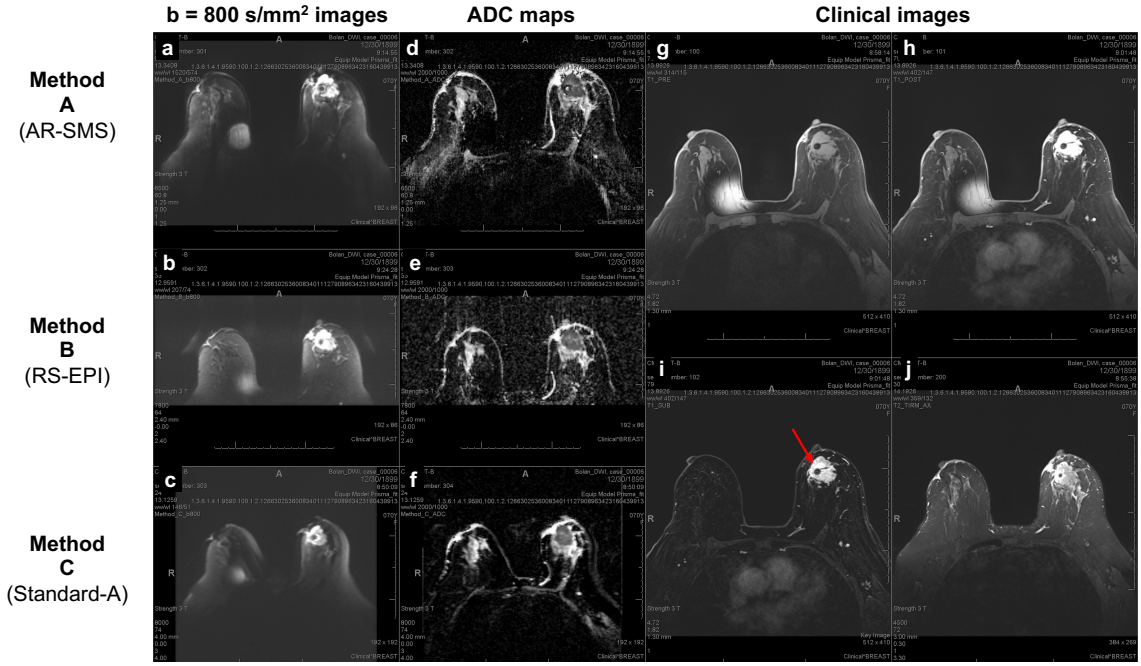

Figure 5.5 – Screenshot of PACS setup for case with biopsy-proven cancer
Readers were provided with clinical images, including pre-CE (g), a single post-CE (h), and CE-subtraction (i) T_1-weighted images and T_2-weighted (j), with the lesion indicated by a red arrow. Diffusion data included axial b = 800 s/mm^2 images (a-c) and ADC maps (d-f) for all three methods, randomly ordered as Methods A, B, and C, which are labeled here for illustration purposes. The metal needle of the contrast injection port caused the artifact on the right breast.

The readers measured the longest dimension on the CE-subtraction and b = 800 s/mm^2 images and lesion-average ADC using a freehand 2D ROI on a representative slice. Readers reported their confidence of these measurements using a 5-point Likert

scale from no confidence (1) to very high confidence (5). Readers reported their impression of overall image quality using a scale of one (unusable) to five (excellent/equivalent to CE-MRI) and ranked the methods (1^{st}-3^{rd}).

Statistical analysis

Scores were fit to a linear mixed effects model including random intercepts for reader and participant to account for repeated measurements. The model was used to measure differences in the overall image quality, method rank, and confidence in length and ADC measurements on DWI. A second model was used, adding the effect of lesion size. Intraclass correlation (two-way random effects of type consistency and single) was used to determine the inter-reader consistency.

While primary analysis was performed combining Standard-A and Standard-B for larger data size, a sub-analysis separately considered the image quality to confirm that the quality was comparable despite fewer b-values used in Standard-B, as shown in the Supplemental Material.

R (V3.6.0, R Core Team, Vienna, Austria) was used for this analysis. Results were considered significant for $p < 0.05$ after a Tukey adjustment for the three pairwise comparisons ("emmeans" package in R).

5.2.3 Results

Participant characteristics

40 women (ages 27-78, mean 51 ± 13) consented to and completed additional DWI scans; 30 of these (ages 27-78, mean 50 ± 14) presented with enhancing lesions on CE-subtraction. Of 32 lesions identified for inclusion, two were used for training radiologists, leaving 30 for analysis (from 28 participants). See Table 5.2.

Table 5.2 – Inclusion and Demographics of Participants

Age indicates age at enrollment in the study. Breast density was recorded according to the patient's medical records on the BI-RADS scale where 1 = BI-RADS A (mostly fatty), 2 = BI-RADS B (scattered density), 3 = BI-RADS C (heterogeneous density), and 4 = BI-RADS D (extremely dense). Any participant included twice was included for two unique lesions. Lesion length was measured on CE-subtraction images based on the average over three readers (lesions included in analysis) or measured by an MR physicist (training cases).

Description	Number of participants	Breakdown	Age (range, mean ± SD)	BI-RADS Breast density (range, mean ± SD)	Lesion length (range, mean ± SD)
Women offered research add-on for at least one time point	52	Screening: 18 I-SPY 2: 34	27-78 49±14	1-4 2.8±0.8	N/A
Women who did not consent to research scans at any timepoint	4	Screening: 0 I-SPY 2: 4	47-55 51±4	2-3 2.5±0.6	N/A
Women that consented to additional DWI scanning for at least one timepoint	48	Screening: 18 I-SPY 2: 30	27-78 49±13	1-4 2.9±0.8	N/A
Women who consented for additional DWI but did not complete the scan for any timepoint	8	Screening: 2, I-SPY 2: 6 Withdrew for discomfort: 7 Technical difficulties: 1	34-46 41±3	2-4 3.1±0.6	N/A
Women that completed additional DWI scanning for at least one timepoint	40	Screening: 16 I-SPY 2: 24	27-78 51±13	1-4 2.8±0.8	N/A
Excluded for missing data	2	Screening: 1 I-SPY 2: 1	47-60 54±9	1-3 2.0±1.4	N/A
Excluded for no qualifying lesion	8	Screening: 7 I-SPY 2: 1	44-70 55±9	2-4 3.1±0.8	N/A
Women with enhancing lesions on CE-subtraction included in study	30 (32 lesions)	--	27-78 50±14	1-4 2.8±0.8	3.1-51.2 19.6±13.3
Enrolled in I-SPY 2 with biopsy-proven cancer, Pre-treatment	12 (13 lesions)	Received Standard-A DWI Analysis: 11, Training: 1	36-78 55±14	2-4 2.8±0.8	12.7-51.2 30.6±9.6
Enrolled in I-SPY 2 with biopsy-proven cancer, Post-treatment	10 (11 lesions)	Received Standard-A DWI Analysis: 9, Training: 1	27-71 43±16	1-4 2.8±1.0	3.1-46.3 15.7±13.7
Undergoing MRI screening	8 (8 lesions)	Received Standard-B DWI Analysis: 8, Training: 0	39-59 50±6	2-3 2.8±0.5	4.1-16.9 8.5±5.3

Phantom

In the resolution phantom (Figure 5.6), the 1 mm feature was only considered detectable in the axial plane on AR-SMS and T_2-weighted. The 2 mm feature was detectable in the axial plane for all methods but was nearly undetectable in the sagittal plane of Standard-A.

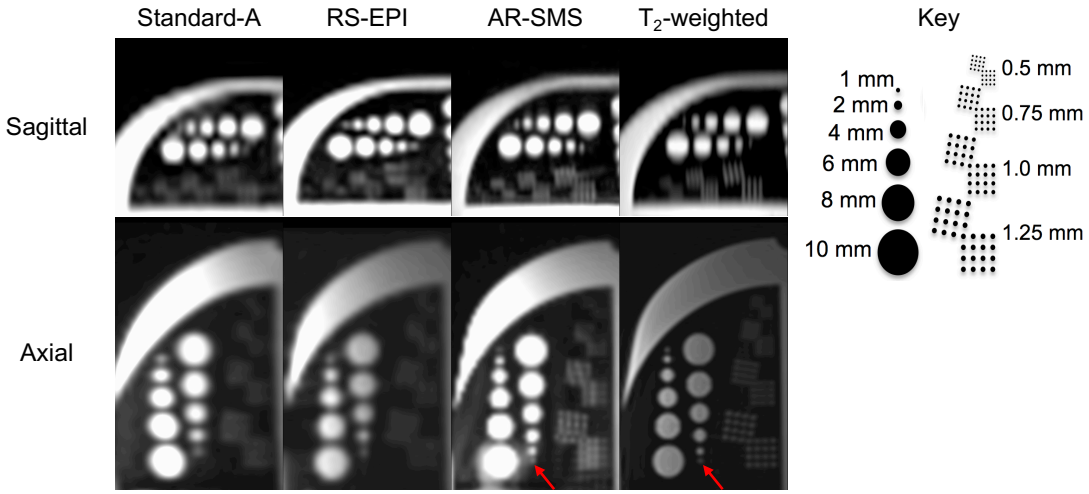

Figure 5.6 – Resolution phantom
Comparing feature detection on b = 0 s/mm^2 images in resolution grid. Key indicates feature sizes. The smallest feature (1 mm), indicated by an arrow, was only considered visible on the AR-SMS and T_2-weighted axial images. 1 mm and 1.25 mm dots in the resolution grids are differentiable on AR-SMS and T_2-weighted image.

Reader analysis

Representative examples of large and small lesions are shown in Figures 5.7 and 5.8. All three readers rated AR-SMS with the highest image quality and ranked AR-SMS higher than both RS-EPI and standard SE-EPI, as shown in Figure 5.9.

The intraclass correlation for overall image quality was poor to fair, indicating that each reader calibrated a unique internal scale. However, the linear mixed effects model accounted for the reader and participant effects. The model found that AR-SMS outperformed RS-EPI, followed by standard SE-EPI in both image quality and rank (Figure 5.9). On the 5-point Likert scale for image quality, RS-EPI rated an average of 0.57 points higher than standard SE-EPI ($p < 0.001$), and AR-SMS scored 1.31 points higher than standard SE-EPI and 0.74 points higher than RS-EPI ($p < 0.001$). Similarly,

on a scale of 1st to 3rd place, AR-SMS ranked highest, followed by RS-EPI and standard SE-EPI as shown in Figure 5.9.

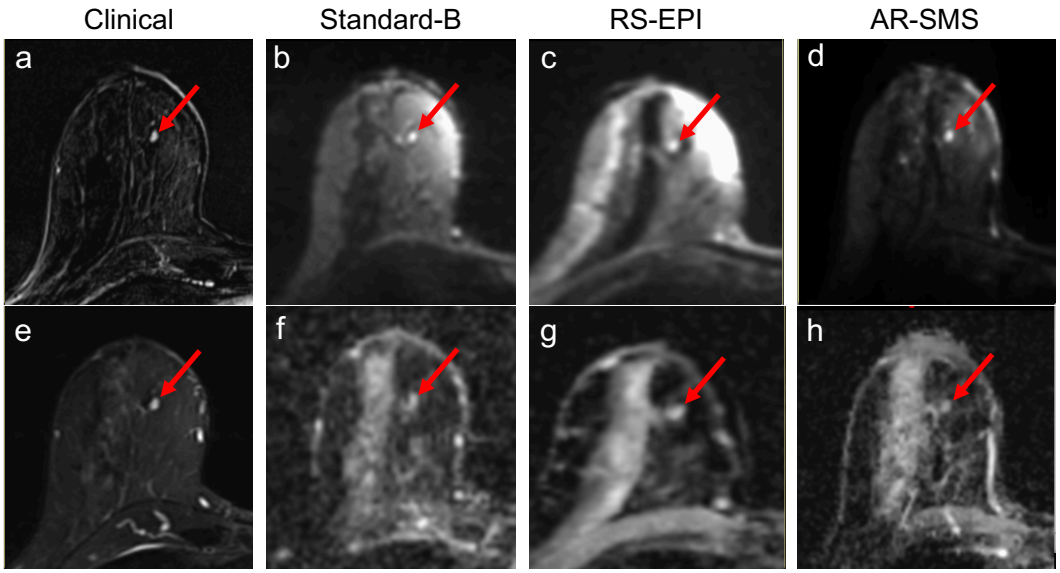

Figure 5.7. Small lesion example
CE-subtraction (a), T_2-weighted image (e), b = 800 s/mm^2 images (b-d), and ADC maps (f-h) are shown, focused on an example of a small enhancing lesion (red arrow). Radiologists were asked to measure the longest dimension on b = 800 s/mm^2 images (b-d) and a lesion-average ADC by drawing a freehand 2-dimensional ROI on each ADC map (f-h). The lesion longest diameter was 4.7 mm, measured on the CE-subtraction (a) and averaged across all readers. Average measurements on b = 800 s/mm^2 images were: (b) Standard = 5.8 mm, (c) RS-EPI = 4.6 mm, (d) AR-SMS = 5.5 mm. Average ADC measurements were: (f) Standard = 1450, (g) RS-EPI = 1590, (h) AR-SMS = 1340 mm^2/s. The average quality scores were: Standard = 2.3, RS-EPI = 2.7, AR-SMS = 3.7.

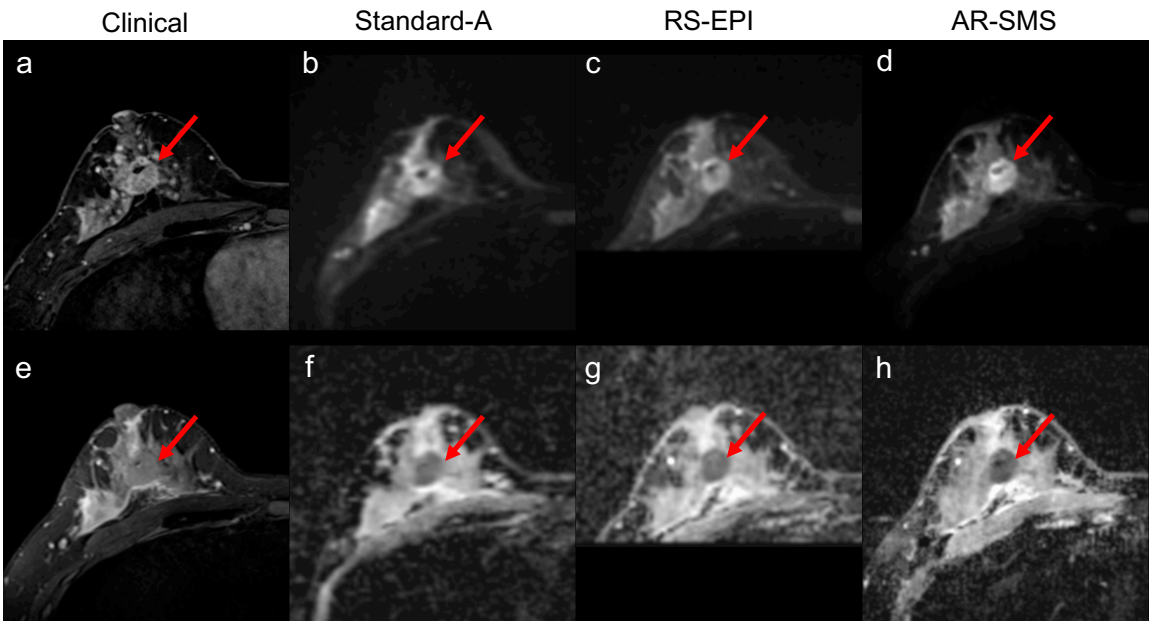

Figure 5.8. Large lesion example
Post-CE (a), T2-weighted image (e), b = 800 s/mm2 images (b-d), and ADC maps (f-h) are shown, focused on an example of a large enhancing lesion (red arrow). Radiologists were asked to measure the longest dimension on b = 800 s/mm^2 images (b-d) and a lesion-average ADC by drawing a freehand 2-dimensional ROI on each ADC map (f-h). The lesion longest diameter was 28.8 mm, measured on the CE-subtraction and averaged across all readers. Average measurements on b = 800 s/mm^2 images were: (b) Standard = 26 mm, (c) RS-EPI = 25.6 mm, (d) AR-SMS = 26 mm. Average ADC measurements were: (f) Standard = 880, (g) RS-EPI = 930, (h) AR-SMS = 840 mm^2/s. The average quality scores were: Standard = 2.3, RS-EPI = 3.0, AR-SMS = 4.0.

Figure 5.9 – Summary of reader study results
Mean overall quality scores on a per-reader basis (a) and method comparison according to linear mixed effects model accounting for participant and reader (b). Error bars indicate standard error. Readers consistently scored AR-SMS higher than RS-EPI and standard SE-EPI. Histogram of relative rank across all three readers and all lesions (c) and comparison of ranks according to linear mixed effects model (d) including significance levels. AR-SMS was most frequently rated 1st, followed by RS-EPI at 2nd. Asterix indicate statistical significance based on Tukey-adjusted p-values.

a)

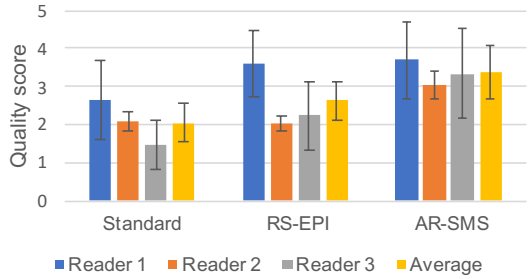

b) **Quality Comparison by Linear Mixed Model**

Method Comparison	Effect (95% CI)	p-value
RS-EPI vs. Standard	0.57 (0.36, 0.77)	<0.001*
AR-SMS vs. Standard	1.31 (1.10, 1.52)	<0.001*
AR-SMS vs. RS-EPI	0.74 (0.54, 0.95)	<0.001*

c)

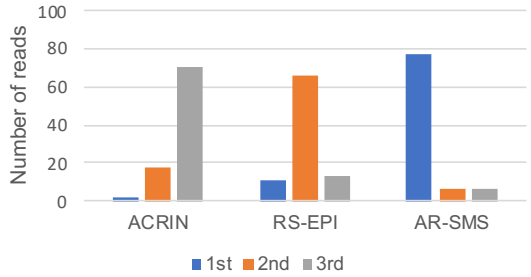

d) **Rank Comparison by Linear Mixed Model**

Method Comparison	Effect (95% CI)	p-value
RS-EPI vs. Standard	-0.73 (-0.89, -0.58)	<0.001*
AR-SMS vs. Standard	-1.53 (-1.69, -1.40)	<0.001*
AR-SMS vs. RS-EPI	-0.80 (-0.95, -0.65)	<0.001*

Histograms in Figure 5.10 indicate the number of reads rated with each confidence level for lesion size and ADC measurements, which reflects lesion measurability. There was higher confidence in the measurement of lesion size using AR-SMS and RS-EPI compared with standard SE-EPI ($p < 0.001$ and $p = 0.002$, respectively); the comparison between AR-SMS and RS-EPI did not reach significance. The method had no effect on the confidence in the measurement of lesion-average ADC ($p \geq 0.296$). See Figure 5.10 for details.

The statistical model indicated that lesion size played a role in the overall image quality scores ($p = 0.01$) independent of method ($p = 0.18$), indicating that the lesion size

did not predict what method would be superior. Multiplicity was 9 for 26 participants (1 lesion, 3 readers, 3 methods) and 18 for 2 participants (2 lesions, 3 readers, 3 methods).

Figure 5.10 – Confidence of lesion size and ADC measurements
Histograms of confidence ratings in measurement of lesion size (a) and ADC (c) on DWI across all readers and lesions. Method comparison (b, d) represents the linear mixed effects model accounting for participant and reader. AR-SMS was rated with the highest confidence in lesion size measurements on b = 800 s/mm^2, followed by RS-EPI, and then standard SE-EPI, with statistical significance (b). The ADC confidence did not depend on the DWI method (d). Asterix indicate statistical significance based on Tukey-adjusted p-values.

a) Confidence in measurement of lesion size

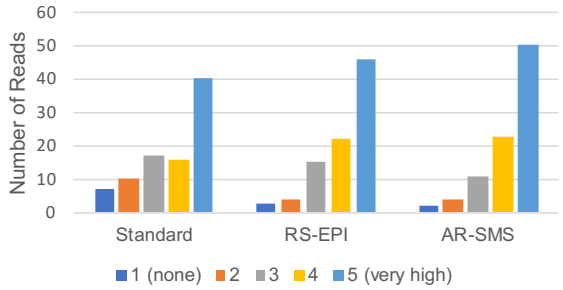

b) **Size Confidence Comparison by Linear Mixed Model**

Method Comparison	Effect (95% CI)	p-value
RS-EPI vs. Standard	0.36 (0.15, 0.56)	0.002*
AR-SMS vs. Standard	0.48 (0.28, 0.68)	<0.001*
AR-SMS vs. RS-EPI	0.12 (-0.08, 0.32)	0.460

c) Confidence in ADC measurement

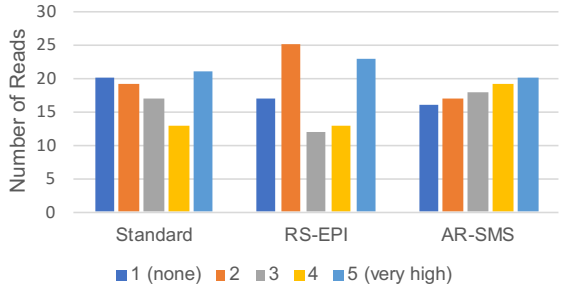

d) **ADC Confidence Comparison by Linear Mixed Model**

Method Comparison	Effect (95% CI)	p-value
RS-EPI vs. Standard	0.04 (-0.16, 0.25)	0.908
AR-SMS vs. Standard	0.16 (-0.05, 0.36)	0.309
AR-SMS vs. RS-EPI	0.11 (-0.10, 0.32)	0.296

5.2.4 Discussion

With growing interest in DWI for breast cancer, it is vital to improve the image quality and resolution of DWI methods. In this study, we compared three five-minute protocols, standard SE-EPI, readout-segmented (RS) EPI, and axially reformatted simultaneous multislice (AR-SMS). In both phantom and *in vivo* measurements, AR-SMS outperformed RS-EPI and standard SE-EPI. While both advanced methods have promise

for improving clinical imaging, AR-SMS achieved larger anatomic coverage and better image quality than RS-EPI (0.74 points, $p < 0.001$).

Both RS-EPI and AR-SMS have unique advantages and challenges. Practically, RS-EPI is more commonly available on clinical scanners, and while general SMS methods are becoming more widespread, AR-SMS is not commercially available currently. By increasing the number of segments, RS-EPI achieves images with reduced geometric distortion at the cost of scan time. However, the RS-EPI protocol was limited in the anterior-posterior coverage, which prevented the inclusion of most lymph nodes. In contrast, AR-SMS encoded a large imaging volume quickly, which allowed for full coverage and a large number of averages/directions but requires robust distortion correction . Combining the encoding speed of AR-SMS with the reduced distortion of RS-EPI may be a promising strategy for future work (131).

Limitations

Our study used a subjective rating of image quality with expert readers because there is no objective reference standard for defining image quality. Although each reader interpreted the 5-point Likert scale differently, the differences between the imaging methods were consistent. Furthermore, we did not control all protocol parameters (i.e. resolution, averages, volume coverage, diffusion scheme) but rather optimized each method independently within a time constraint, as done clinically. All three methods could potentially be improved with further optimization, which limits the ability to generalize the study results.

The PACS software used did not support co-localization of ROIs across ADC maps and diffusion-weighted source images. Although readers rated the high-resolution methods with higher image quality and confidence in size measurements, the confidence in measuring ADCs did not change. With co-localization, we would expect the confidence in ADC measurement to increase similarly to that of lesion size measurement, which significantly improved for RS-EPI and AR-SMS. The confidence in both lesion size and lesion-average ADC is likely to increase with additional experience with DWI in a clinical setting, especially for methods with higher spatial resolution.

In conclusion, the proposed axially reformatted simultaneous multislice imaging protocol provided higher spatial resolution and image quality than both the standard spin-echo EPI breast DWI and a high-resolution readout-segmented EPI approach, based on phantom measurements and a reader study of *in vivo* imaging. Future work is needed to further compare specific protocols and compare the clinical performance of these techniques.

5.2.5 Supplemental materials

Additional methods details

Table 5.3 includes the acquisition details, including scan order and acquisition times.

Data acquired with the axially reformatted simultaneous multislice imaging (AR-SMS) protocol were reconstructed offline in MATLAB 2017b (MathWorks, Natick, MA) using an in-house pipeline. Across five random cases, on a single server (quad AMD Opteron 6140, 256 GB RAM), the average total reconstruction time, excluding data transfer, was 6 hours 36 minutes per case of 28 acquisitions each; approximate times for each step are listed. The reconstruction was developed for high image quality and was not optimized for efficient reconstruction. Future work would be necessary to speed up the reconstruction for clinical use.

First, each acquisition of undersampled data and reference lines was independently corrected for Nyquist ghosts with a slice- and coil-specific, first-order correction estimated by ghost/object minimization (110) (40 minutes). Single band and fully sampled reference data were used to calculate weights for phase encoding unaliasing using GRAPPA (30) and SMS separation using Slice-GRAPPA (36) (10 minutes). SMS unaliasing was performed on each acquisition (35 minutes), followed by a second iteration of slice-specific Nyquist ghost correction on each unaliased slice using ghost/object minimization (63 minutes). GRAPPA weights were applied for phase encoding unaliasing (39 minutes). The partial Fourier edge was filtered with a $\sin^2$ window (7 seconds). Coil combination was performed using a root sum-of-square (16 minutes). The magnitude images were then corrected for geometric distortion using topup

(130) based on fully sampled reference data with reversed phase encoding (3 hours 8 minutes). Averaging was performed to combine equal b-values, and then the ADC map was calculated using a log-linear fit with masking of negative values (0.5 seconds). Finally, the separate axial b-value images and ADC maps were written in Digital Imaging and Communications in Medicine (DICOM) format for viewing.

Table 5.3 – Acquisition details
All clinical scans were completed before the advanced DWI, which were performed for research only. Acquisition times are listed in min:sec.

Clinical Protocol		I-SPY 2 Protocol	
Localizer	0:17	Localizer	0:17
T_1-weighted 3D GRE (without fat suppression)	1:24	T_1-weighted 3D GRE (without fat suppression)	1:24
Interactive shimming	~2:00	Interactive shimming	~2:00
T_1-weighted 3D GRE (with fat suppression)	0:32	T_1-weighted 3D GRE (with fat suppression)	0:40
DWI (Standard-B)	3:46	DWI (Standard-A)	4:48
T_1-weighted CE (1 pre-contrast, 3 post-contrast)	7:52	T_1-weighted CE (1 pre-contrast, 6 post-contrast)	10:44
T_2-weighted TIRM	4:59	T_2-weighted TIRM	4:59
Spoiled 3D GRE (VIBE)	2:45	Spoiled 3D GRE (VIBE)	2:45
Axially reformatted SMS (scan 1)	4:54**	Axially reformatted SMS (scan 1)	4:54**
Axially reformatted SMS (scan 2)	1:13**	Axially reformatted SMS (scan 2)	1:13**
RS-EPI	4:58	RS-EPI	4:58
TOTAL	34:40	TOTAL	38:52
**Note: AR-SMS was acquired with two additional reference scans because the optimal reconstruction was not known *a priori*. However, the data used for image reconstruction (including SMS, GRAPPA, and topup reference scans) were acquired in 4:52.			

Sub-analysis comparing Standard-A and Standard-B

The standard SE-EPI protocol used was determined by the clinical indication; I-SPY 2 patients received Standard-A, while clinical, non-trial patients received the shorter Standard-B. In order to have a larger number of lesions, the main analysis treated both variations of standard SE-EPI (A and B) as a single group, expecting negligible

differences between the scans. To confirm this choice, a linear mixed model was retrospectively performed in a sub-analysis to fit the image quality ratings after separating Standard-A and Standard-B. The quality of Standard-A and Standard-B were not statistically different, modeled as 2.11 and 1.92, respectively ($p > 0.354$). Moreover, Table 5.4 shows that both Standard-A and Standard-B were rated significantly lower than RS-EPI and AR-SMS. This confirms that the previous interpretation of method comparison is consistent for both Standard-A and Standard-B.

Table 5.4 – Sub-analysis separating Standard-A and Standard-B
Data was separated into two categories based on what standard SE-EPI protocol was used (Standard-A or Standard-B). The overall image quality was fit to a linear mixed model, including effects from reader and participant, for each group. Results confirm that the comparison of image quality is consistent across both Standard-A and Standard-B. Asterix indicate statistical significance after Tukey adjustment.

Model	Method Comparison	Effect (95% CI)	p-value
Model 1 – including Standard-A N = 22 lesions	RS-EPI vs. Standard-A	0.56 (0.32, 0.80)	<0.001*
	AR-SMS vs. Standard-A	1.33 (1.09, 1.58)	<0.001*
	AR-SMS vs. RS-EPI	0.77 (0.53, 1.02)	<0.001*
Model 2 – including Standard-B N = 8 lesions	RS-EPI vs. Standard-B	0.58 (0.18, 0.98)	0.017
	AR-SMS vs. Standard-B	1.25 (0.85, 1.65)	<0.001*
	AR-SMS vs. RS-EPI	0.67 (0.27, 1.07)	0.005*

Phantom ADC quantification

The breast phantom (CaliberMRI) contains twelve compartments of varying polyvinylpyrrolidone (0 to 40%) and water to imitate *in vivo* tissue with various ADC values. The manufacturer reported nominal b-values for these compartments between 533 and 1456 mm^2/s measured at 18.2°C ± 0.4°C. The breast phantom was scanned in the 16-channel breast coil (i.e. outside of isocenter) using each method, repeated four times in one scan session. The experiment was not temperature controlled and did not include gradient non-linearity correction. The temperature of the scan room was approximately 70°F (21.1°C). The nominal true ADC values reported by the manufacturer were adjusted

by 2.4%/°C following [Ref (132)]. Standard and RS-EPI ADC maps were generated online such that details on fitting, filtering, masking etc. are unknown to the authors. AR-SMS was reconstructed by an inhouse pipeline, including a log-linear fit to produce ADC maps. Regions of interest were manually drawn (initials) on Digital Imaging and Communications in Medicine (DICOM) images, in a center slice of each compartment to measure the mean ADC.

The mean ADC values from each compartment, averaged across four measurements is plotted in Figure 5.11 against the adjusted nominal ADC, where the dotted line represents concordance. Despite using varying methods, b-values, averages, and resolutions, all three methods measure similar ADC values, which correspond closely to the nominal ADC values estimated at 70°F (dotted line). Standard and RS-EPI measure ADC values that are slightly higher than those measured by AR-SMS.

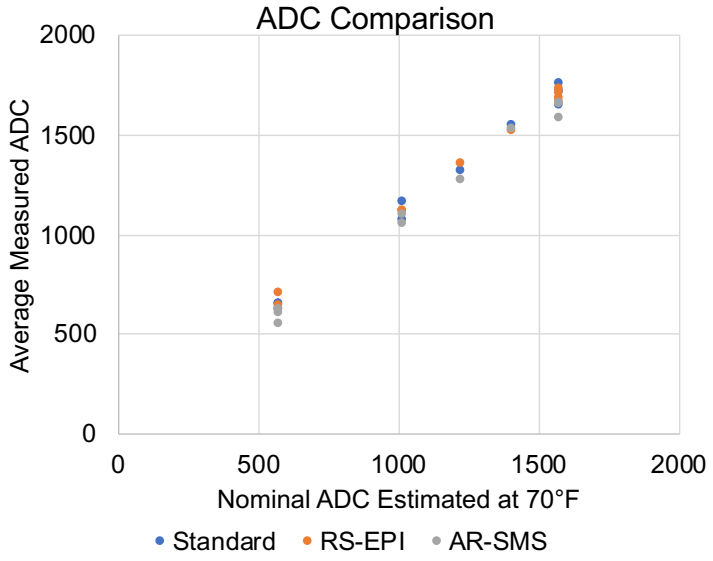

Figure 5.11 – ADC Comparison
Average ADC values measured in manual ROIs of 12 compartments with varying ADCs (5), averaged over four repetitions. Measured values are plotted against nominal ADC values estimated based on the manufacturer's reported values and the scan room temperature of about 70°F. Color indicates DWI method and dotted line indicates concordance with estimated nominal values. All three methods measure reasonable ADC values despite experimental limitations.

This ADC comparison is limited by the lack of temperature control, potential differences in ADC fitting algorithms, and uncorrected gradient non-linearities, especially outside of iso-center. However, the results suggest that both advanced DWI methods measure reasonable ADC values without substantial bias. Future work is needed to define ADC thresholds and explore the diagnostic value of AR-SMS.

Lesion size comparison

In the reader study, radiologists were asked to measure the longest diameter (LD) of the lesion on a CE-subtraction image, followed by b = 800 s/mm^2 images from each DWI method in random order. The radiologist was free to pick a representative slice of their choosing or decline to answer based on their perceived inability to measure. The root-mean-square error (RMSE) was measured between LDs measured on CE-MRI and b = 800 s/mm^2 images from each method. Lesions for which no measurement was recorded were excluded.

The RMSE for each DWI method is listed in Figure 5.12. The lesion LD measured on AR-SMS was closest to that measured on the CE-subtraction image, followed by RS-EPI. The lesion was considered “unmeasurable” on 5 reads for Standard SE-EPI and 2 for each RS-EPI and AR-SMS.

The comparison of lesion length measurements between CE-MRI and high b-value images gives us some valuable insight as to how fully DWI captures the story of a lesion with respect to the gold standard. This comparison may be especially important in the context of contrast-free screening. As anatomical images are acquired with high spatial resolution, one would expect that the longest diameter measurements would increase in agreement as DWI resolution improves, which is reflected in these results. However, this analysis is inherently limited as the contrast of CE-subtraction images is not always consistent with that of b = 800 s/mm^2 images. Furthermore, the slice positions did not match exactly across DWI methods as the radiologists were each free to choose a representative slice. Thus, the measurements may not reflect the same region of the lesion.

a)

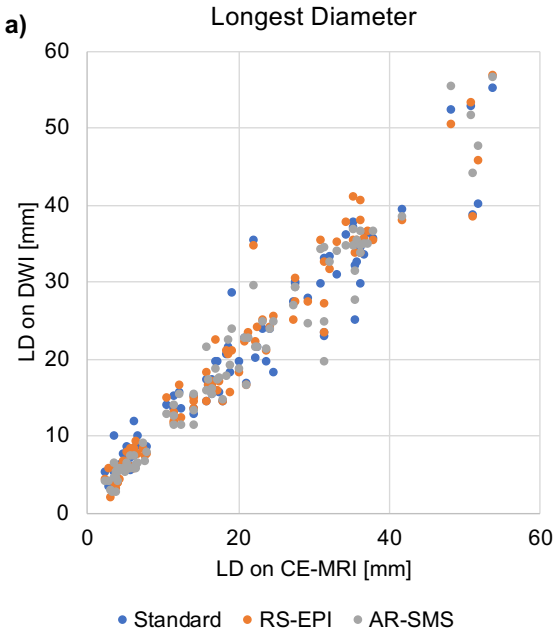

b) **Difference between LD on CE-MRI and DWI**

DWI Method	RMSE (mm)	Number of reads considered 'unmeasurable'
Standard SE-EPI	3.88	5 (4 lesions by 2 readers)
RS-EPI	3.03	2 (1 lesion by 2 readers)
AR-SMS	2.88	2 (1 lesion by 2 readers)

Figure 5.12 – Longest diameter comparison
The longest diameter (LD) measured on the b = 800 s/mm^2 images compared to that measured on the CE-subtraction is plotted for each reader and lesion (a). The root-mean-square error between the LD measured on CE-subtraction and b = 800 s/mm^2 images, in mm, is listed (b) for each DWI method. Standard SE-EPI was unmeasurable for 5 reads (4 lesions), RS-EPI for 2 reads (2 lesions), and AR-SMS for 2 reads (2 lesions).

Chapter 6: Future Directions

In any scientific research, with every small step of progress comes several new questions begging to be answered. Here I will list a few open questions and ideas for where to take this project next that, if given infinite time, I would explore. Some preliminary data is provided where available. These next steps fall into two main areas: applications, like clinical applications and extending to other organs, and further technical development.

6.1 Assess Clinical Value of High Resolution DWI

In this work, we have shown that axially reformatted (AR) SMS, combined with Ghost/Object minimization for ghost correction and topup distortion correction, can achieve high resolution breast DWI in a clinically reasonable scan time. Three breast radiologists consistently rated AR-SMS higher than and preferred it to both the standard SE-EPI and a RS-EPI approach. However, gains in image quality are inconsequential unless it simultaneously improves clinical practice and outcomes.

I hypothesized that a major factor in the slow clinical adaptation of breast DWI is the poor quality and resolution of current methods. Thus, the question is, "does better resolution really lead to better diagnostic value?". To answer, a crucial next step for AR-SMS is to assess its clinical performance. First, the ADC values should be compared to those measured with standard and other advanced techniques, *in vivo*, to ensure no systematic bias based on these methods. These ADC values should additionally be assessed to determine the ability to differentiate benign and malignant lesions. Secondly, it would be interesting to measure the sensitivity of these methods in a non-contrast screening setting, in comparison to both other DWI methods, as well as contrast enhanced scans or abbreviated screening protocols.

6.2 Translation of Techniques Beyond Breast

MRI of other body regions faces many of the same challenges as breast imaging does, especially in the abdomen, including respiratory and cardiac motion, large fat signals, and severe B_0 inhomogeneities caused by wide FOVs and greater variation in magnetic susceptibility. Thus, a reasonable next step would be to apply AR-SMS in other

challenging organs, like liver and pelvic imaging. Similarly, the ghost correction methods applied here may be useful for other applications, including a wide range of EPI acquisitions. The referenceless methods were applied to liver and prostate imaging in the following section.

6.2.1 Referenceless Nyquist Ghost Correction for DWI Outside of the Breast

This work was previously presented as part of an electronic poster entitled *Novel Image-based Nyquist Ghost Correction of Diffusion-Weighted Echo Planar Imaging with Ghost Ratio Minimization (GRM)* at ISMRM 26th Annual Meeting and Exhibition. Paris, France; June 2018. Abstract #5339.

Jessica A McKay, Steen Moeller, Sudhir Ramanna, Edward J Auerbach, Gregory Metzger, Michael T Nelson, Kamil Ugurbil, Essa Yacoub, Patrick J Bolan

Introduction

DWI is used in medicine and research for several pathologies and in a wide variety of organs, each of which faces unique challenges and considerations. While the linear navigator often works reliably to remove Nyquist Ghosts in diffusion imaging in the brain, it can be insufficient in some cases. Likewise, the three-line navigator occasionally fails in prostate DWI and leaves residual ghost in liver data. This less than ideal navigator correction is caused by mechanisms that may be unique to the particular organ, acquisition strategy, or even the MR system. These mechanisms may include eddy currents that cause time varying phase or spatial dependencies that required higher order correction. If, however, the residual ghost is fully or in part caused poor fitting of the 3-line navigator, referenceless methods may be a valuable tool for a wide variety of data, providing a robust correction that can be applied retrospectively to complex raw data. These methods work by defining a cost function $f_{cost}(\kappa,\varphi)$ which is minimized when the image is ghost-free. Examples include the entropy method (100,101), which minimizes the entropy in the image domain, the SVD method (102), which operates on k-space, and Ghost/Object minimization (G/O), proposed in Chapter 4. The performance of these methods is generally good, but it can vary with geometry, signal to noise ratio (SNR), and

amount of ghost-object overlap. In this work these referenceless methods, including G/O, will be extended to test their performance in brain, prostate, and liver DWI.

Methods

To demonstrate *in vivo* feasibility, each referenceless method was retrospectively applied to DWI acquired in several body regions. Corrections were estimated independently for each channel, slice, and acquisition (b-value and average) for 1) brain DWI with simultaneous multislice (SMS, MB = 4), 2) fully sampled prostate DWI, and 3) liver DWI with R = 3 and segmented ACS lines. For parallel imaging cases, the initial ghost correction was estimated using the auto calibration scans (ACS) and applied to the undersampled data. Ghost correction was then refined on a per-channel and per-repetition basis after GRAPPA reconstruction. Apparent diffusion coefficient (ADC) maps were generated using a pixel-by-pixel log-linear fit.

Results

Brain data acquired with SMS (MB = 4) b = 0 s/mm^2 images are shown in Figure 6.1 as a montage across all slices and a close-up of a subset, scaled to highlight residual ghosts. The online reconstruction fails to fully correct the ghosts in this case, while all four referenceless methods achieve almost complete ghost suppression.

Fully reconstructed axial ADC maps are shown in Figure 6.2 that roughly represent the ghost levels in from the prostate and liver DWI. SVD performed poorly in all slices of this prostate case, while both entropy and G/O fully suppressed the ghost. In the given selected slice of liver DWI, SVD performs best, which is consistent for most but not all of the other slices.

Figure 6.1 – Brain ADC maps
ADC maps for an example brain case acquired at 3 T with R = 2, scaled to highlight Nyquist ghosts. The montage on the left contains all slices, showing that the 3-linle navigator consistently leaves residual ghosts. A few slices (red box) are highlighted on the right, which shows reduced ghosts using Entropy, SVD, and Ghost/Object.

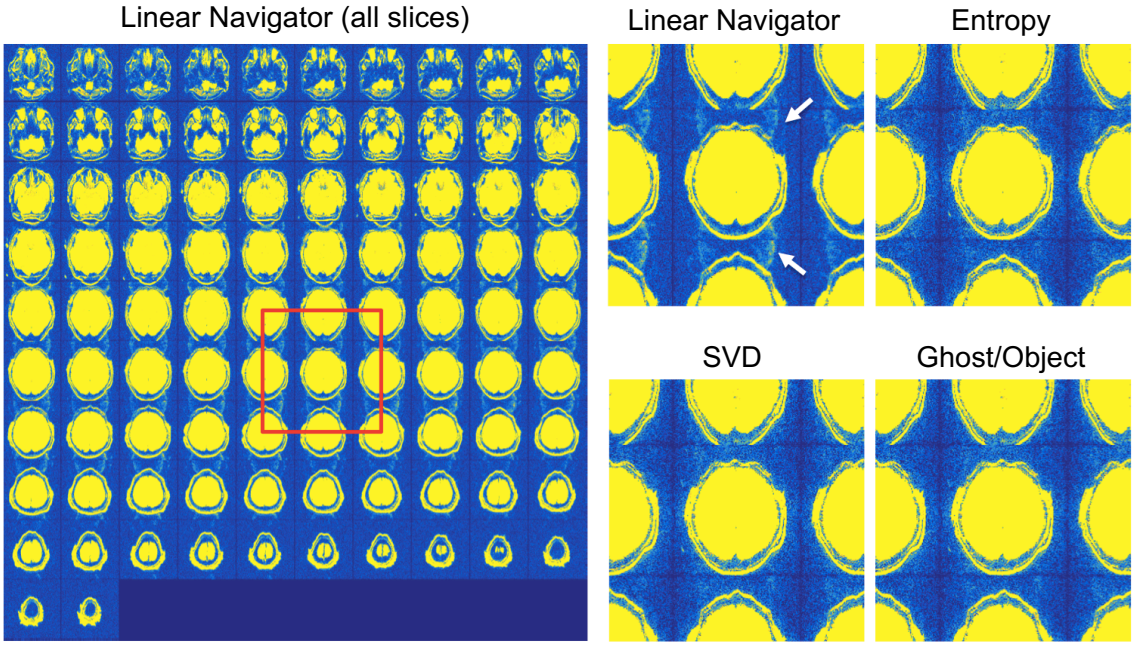

Figure 6.2 – Prostate and liver ADC maps
a) Fully sampled prostate data acquired at 7 T shows a large ghost after navigator correction. Entropy and Ghost/Object fully reduce the ghost. SVD leaves some residual ghost. b) liver data acquired at 3 T with R = 3 undersampling and segmented ACS lines. The slice shown is representative. However, the performance was variable across slices for all methods.

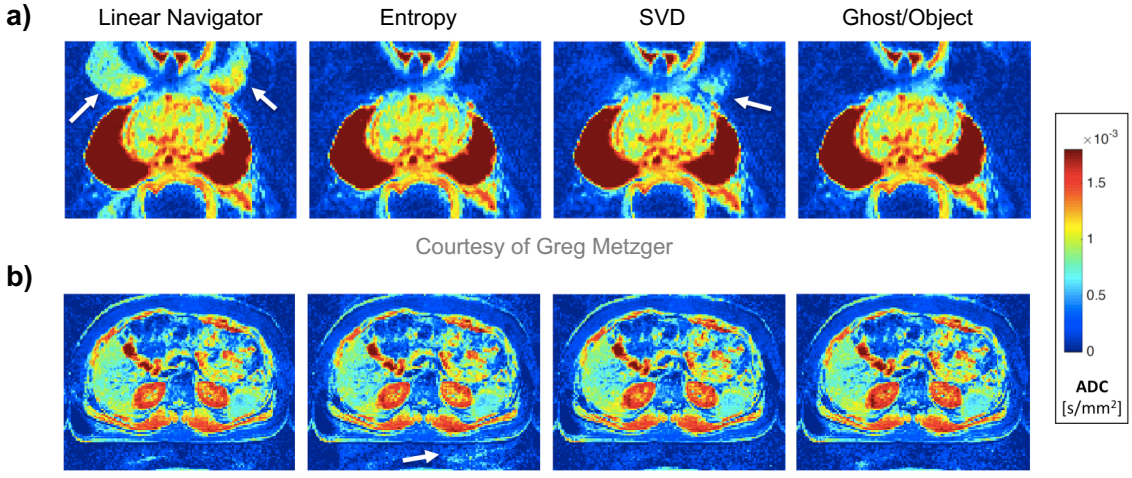

Discussion and conclusion

We have demonstrated the feasibility of ghost correction with ghost/object minimization in a variety of DWI data. A careful comparison of G/O with the linear navigator and other referenceless methods was performed in breast R = 3 data (106), but further work is needed to compare in prostate, liver, and brain imaging. Although background regions were assessed visually as a surrogate for ghost correction performance, even inconspicuous residual ghosts can bias diffusion parameters in the tissue.

In general, entropy and SVD methods work well, but in some cases, one performs noticeably worse. The addition of G/O provides a third independent option, which can be combined with entropy and SVD for increased robustness.

Ghost correction by G/O is feasible in DWI of both brain and body applications. The cost function of G/O has different characteristics than the other referenceless methods and may be less sensitive to noise.

6.3 Additional Technical Developments

6.3.1 Address distortion and/or resolution with segmentation

There are two disadvantages of AR-SMS. First, despite the efficient encoding, it still requires a long echo spacing, which causes substantial geometric distortion. Distortion correction requires a fully sampled reference scan and very long reconstruction time. Moreover, even with the correction there is still residual distortion that can complicate reading and disrupt colocalization with other images. For example, if one wants to measure the ADC in a contrast enhancing lesion, the lesion may have a different geometry and might even be hiding a few slices away. The long echo spacing also adds to blurring in the PE direction. As seen in Section 5.2, RS-EPI successfully reduces geometric distortion by using 5 segments at the cost of a longer acquisition time for a single average. Therefore, it may be advantageous to combine the efficiency of AR-SMS with the short echo spacing of RS-EPI.

A second disadvantage is that with SMS acceleration of 4x, the in-plane undersampling is limited. Another way to reduce the effective echo spacing is with

multishot (MS) EPI using interleaved segments in the PE direction. While MS-EPI works similarly to in-plane undersampling, reconstruction only requires the estimation (directly or indirectly) of smooth phase differences between shots compared to filling in every point as undersampling requires. Thus, MS-EPI could reduce the effective echo spacing beyond that achieved with R = 2. Furthermore, MS-EPI can potentially be implemented by replacing some of the averages to improve the distortion without increasing scan time.

6.3.2 Address Nyquist ghosts

Referenceless methods performed well for the 1st order phase errors in both standard SE-EPI and AR-SMS in this work. However, this minimization is time consuming and only includes a 0th and 1st order parameter. This ghost correction problem is a good candidate for machine learning (133,134). Ghost artifacts can be simulated with complicated parameters (e.g. time-varying, higher order, or 2-dimensional) to create a large set to train a neural network. In this way, the correction could be more universal and applied to ghosts of many types. Furthermore, machine learning could greatly reduce the reconstruction time, circumventing the minimization problem.

6.3.3 Develop objective methods for assessing image quality

One fundamental limitation of this work is the subjective nature of the method comparisons. Here, I present a preliminary exploration of a metric adapted from computer vision to objectively measure the resolution of AR-SMS DWI. This work was previously presented as part of an electronic poster entitled *Adaptation of a Computer Vision Blur Metric to Objectively Compare High Resolution DWI Strategies in in vivo Breast Imaging* at ISMRM 27th Annual Meeting and Exhibition. Montreal, Quebec; May 2019. Abstract #4116.

Jessica A McKay, Gregory J Metzger, Steen Moeller, An Church, Michael T Nelson, and Patrick J Bolan

Introduction

While diffusion weighted imaging (DWI) has shown promise for detecting and characterizing breast cancers (135), the low spatial resolution of the standard technique

(spin-echo echo planar imaging, SE-EPI) limits lesion detection and biases apparent diffusion coefficients (ADCs) due to partial volume effects.

Several strategies have been proposed to generate high resolution DWI, including reduced field-of view (136), steady-state imaging (137), readout-segmented EPI (138), and simultaneous multi-slice imaging (SMS) (139,140). It is of important to objectively compare techniques throughout development to guide protocol optimization for various applications.

However, comparing resolution can be difficult for several reasons: the nominal resolution does not reliably reflect the true image resolution due to blurring effects from off-resonance, T_2 decay, and respiration, especially in EPI; subjective assessment is laborious and prone to bias (141); and phantom assessments cannot fully replicate all *in vivo* sources of image blurring.

This work adapts an objective measurement from the computer vision field, the Crété-Roffet metric (142), to objectively assess the resolution of several DWI strategies. The Crété-Roffet metric quantitatively measures blurring from 0 (sharp) to 1 (blurry) and has previously been validated against subjective blur assessment. *The purpose of this work is to use the blur metric as an objective way to compare standard breast DWI with two high resolution strategies, including RO-segmented EPI and SMS-EPI and to validate the metric using a resolution phantom.*

Methods

Fifteen breast cancer patients undergoing MRI for monitoring chemotherapy response were scanned under an IRB-approved protocol. All measurements were performed on a Siemens 3 T Prisma^{Fit} scanner using a 16-channel Sentinelle breast coil. DWI was acquired with 3 protocols, each constrained to a 5-minute acquisition: standard single-shot SE-EPI (**Std**) following the ACRIN 6698 protocol, readout-segmented EPI (**RS-EPI**) with 5 segments based on Wisner et al.'s protocol (136), and a simultaneous multi-slice (**SMS**) acquisition acquired sagittally and reformatted axially (140). A standard anatomical T_2-weighted image (**T_2w**) was included for comparison. All protocols were repeated on a quantitative breast phantom (CaliberMRI, Boulder, CO)

(128) that includes a resolution grid and tissue mimics. Sequence details are provided in Table 6.1.

Image processing was performed in MATLAB using DICOM (magnitude) images. Because each protocol was acquired with different nominal resolutions, all images were resampled onto a common 0.5 mm isotropic grid (smaller than any nominal resolution). The blur metric was calculated independently for each direction.

Table 6.1 – Protocol parameters
All DWI acquired within 5-minute scan time.

Parameter	Standard	RS-EPI	AR-SMS	T_2-weighted
Sequence	Single-shot SE-EPI	SE-EPI, 5 RO segments	Single-shot SE-EPI	Turbo spin echo
TR / TE [ms]	8000 / 74	7800 / 64	6500 / 60.80	4500 / 72
Nominal Resolution [mm] (RO x PE)	1.7 x 1.7	1.8 x 1.8	1.25 x 2.5	0.8 x 0.8
Slice thickness	4 mm	2.4 mm	1.25 mm	3 mm
PE	R → L	A → P	H → F	R → L
RO x PE FOV [mm]	320 x 320	350 x 156.8	240 x 240	320 x 320
# of Slices	36	56	256	60
Acceleration	R = 3	R = 2	R = 2 MB = 4	R = 2

Results

Figure 6.3 shows axial b = 0 s/mm^2 DWI and T_2w anatomical images of the resolution grids of the breast phantom. The 2 mm feature (red) is barely detectible in the Std approach and readily visible with RS-EPI. Only the AR-SMS DWI approach can detect the smallest 1 mm feature (blue) and 1.25 mm grid (yellow), which are sharpest in the anatomical T_2w image. Figure 6.4 shows the three DWI methods and the T_2w anatomical image from an example *in vivo* case after resampling to a 0.5 mm common grid. The increase in effective resolution from left to right can be readily observed. Figure 6.5 shows the blur metric measured in the axial plane (average of right-left and anterior-posterior) for the three DWI methods at both b = 0 and 800 s/mm^2, and also for the T_2w image. Consistent with Figures 6.3 and 6.4, T_2w shows the least blurring, followed by

SMS-EPI, RS-EPI, and finally the standard SE-EPI technique. Note that the b = 800 s/mm^2 image is blurrier than the b = 0 s/mm^2 measurement for all DWI methods due to increased relative fat signal, eddy currents, and averaging over respiratory cycles.

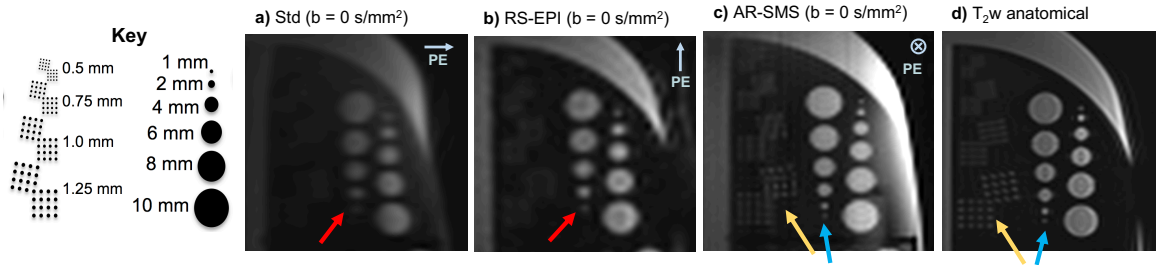

Figure 6.3 – Feature detection in breast phantom
Examples of feature detection in breast phantom imaging in b = 0 s/mm^2 DWI acquired by a) standard SE-EPI, b) RS- EPI, and c) axially reformatted SMS, and a T_2w anatomical image (d), all resampled to 0.5 mm isotropic. Arrows indicate the smallest features detected (red: 2 mm feature, yellow: 1.25 mm grid, blue: 1 mm feature). PE directions are indicated.

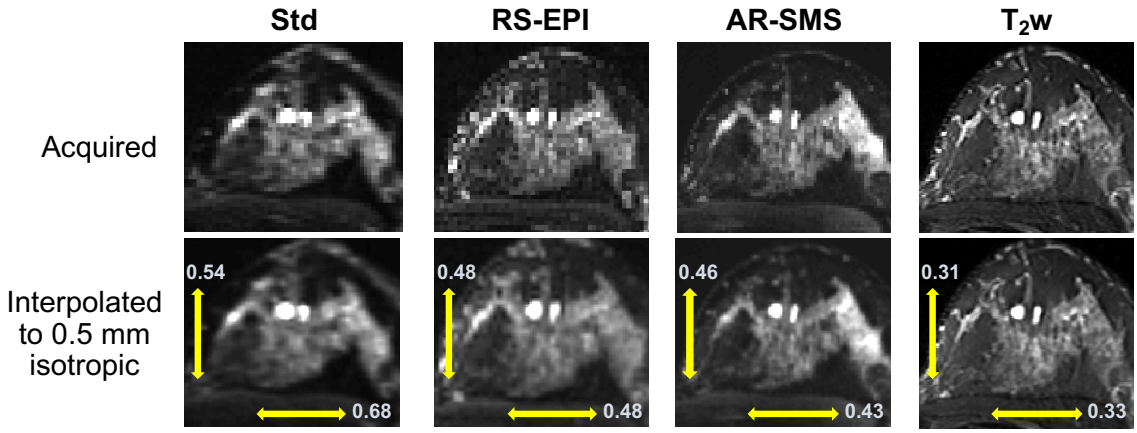

Figure 6.4 – Example CR metric
Examples of standard SE-EPI, readout-segmented EPI, and axially reformatted SMS EPI b = 0 s/mm^2 images, and d) T_2w anatomical image, all resampled to 0.5 mm isotropic to measure the CR metric independently in each direction.

In Figure 6.5 the standard method shows more in-plane blurring than the readout-segmented method even though its nominal pixel size is smaller. Figure 6.6 explores this further by plotting the blur metric as a function of nominal pixel size for all images in all

3 directions. There is a general trend for greater sharpness with smaller pixel sizes (green line), but this does not hold for phase encoding in single-shot EPI.

Figure 6.5 – Axial CR metric

Plot of in-plane axial blur metric for different DWI images and T_2w anatomical image over all 15 patients. Note the close inter-subject consistency. The higher b-value shows increased blurring, as expected due to higher eddy currents that contribute to blurring and many averages at b = 800 s/mm^2.

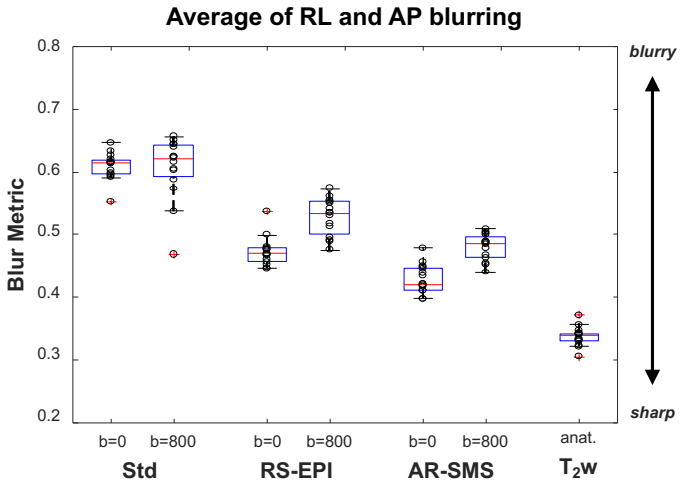

Figure 6.6 – CR metric vs nominal resolution

The measured blur metric, after interpolation to 0.5 mm isotropic, is plotted for all three directions against the nominal resolution. The green line indicates an approximate calibration between the blur metric and the acquired pixel size, based on the T_2w resolution, which is close to nominal.

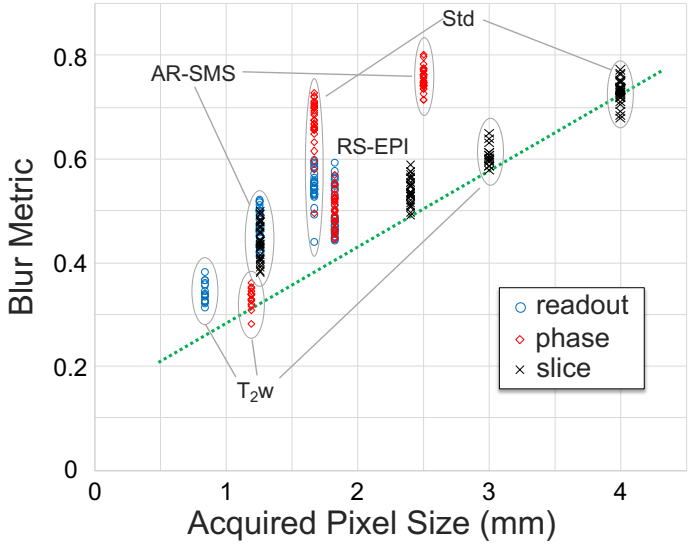

Discussion

This technique can be used to objectively assess *in vivo* performance and guide sequence optimization. However, because the metric may be noise- and contrast-dependent, further work is needed to fully calibrate the blur metric as a tool to measure the true resolution. We propose that the green line in Figure 6.6 roughly estimates the relationship between the blur metric and the effective resolution. For example, the in-plane blurring observed in the standard DWI (1.7 x 1.7 mm) is comparable with a non-EPI encoded image with resolution of ~3 x 3 mm, which is consistent with Figure 6.3a where the 2 mm feature is blurry, and the 1.25 mm grid is undetectable. Similarly, the true resolution of the T_2w anatomical image approaches nominal in-plane resolution of 1.2 x 0.8 mm, and the 1 mm feature is most sharply detected in the T_2w image (Figure 6.3d).

Conclusions

While nominal resolution was found to be a poor predictor of image blurriness in single-shot EPI, the proposed use of the Crété-Roffet blur metric on consistently resampled images appears to be a robust and objective means of comparing effective resolution on *in vivo* data. In this comparison, both high-resolution DWI methods showed an improvement in in-plane resolution over the standard DWI technique but were inferior to the T_2w image.

Chapter 7: Final Thoughts

Breast DWI has long been known to provide information about the malignancy of breast lesions and has been proposed as a tool for breast screening, monitoring treatment response, and staging breast cancer. However, its clinical use is greatly limited due to lack of consensus and poor image quality and resolution available, especially outside of research institutions. The goal of this work was to improve the image quality and resolution of breast DWI, which will improve lesion detection, increase the measurability of ADC maps, and improve colocalization with anatomical images, thus improving the value of breast DWI. To that aim, Ghost/Object (G/O) minimization and axially reformatted simultaneous multislice (AR-SMS) breast DWI were developed through this work.

AR-SMS uses the standard single shot spin-echo (SE) EPI along with major advancements in SMS to acquire full coverage bilateral breast DWI. Within a 5-minute scan time, AR-SMS can achieve 1.25 x 1.25 x 2.5 mm nominal resolution, which approaches that of typical T_2-weighted anatomical images. The major advantages of AR-SMS are its efficient encoding, which allows for a large number of averages and diffusion weights, and its high and nearly true axial resolution. AR-SMS can still suffer from Nyquist ghosts, as the 3-line navigator often fails in breast DWI. In this work I characterized the ghost artifact and carefully considered the failure of the 3-line navigator. While the navigator can account for static B_0 inhomogeneity, it is extremely sensitive to fat signal and changes throughout the acquisition, like eddy currents. I addressed Nyquist ghost correction by developing G/O minimization, which proves to be simple, reliable, and insensitive to low SNR and undersampling. I showed that G/O minimization reduces ghosts in standard SE-EPI data and the advanced AR-SMS approach. Additionally, in AR-SMS data, G/O can be applied iteratively with MB slice separation to achieve a slice-specific correction.

Finally, the AR-SMS performance, combined with G/O ghost correction and topup distortion correction, was evaluated in a reader study. Three breast radiologists consistently preferred AR-SMS, to standard SE-EPI and readout-segmented (RS) EPI

with 5 segments. Unfortunately, AR-SMS still suffers from geometric distortion, which may be improved using segmentation in future work (RS-EPI or MS-EPI).

These technical developments improved the spatial resolution of breast DWI and reduced the imaging artifacts. A critical next step is to evaluate the diagnostic performance of AR-SMS against other DWI techniques and CE-MRI. With continued improvements, high quality breast DWI can become widely available in clinical and research settings. It is my sincere hope that these technological gains, along with numerous other efforts in the field, improve our understanding of breast cancer and advance breast cancer treatment, reducing overtreatment and unnecessary biopsies, while reliably detecting aggressive cancers in their earliest stages.

References

1. Street W. Cancer Facts & Figures 2020. 1930:76.

2. Street W. Breast Cancer Facts & Figures 2019-2020. :44.

3. Mann RM, Kuhl CK, Moy L. Contrast-enhanced MRI for breast cancer screening: Breast MRI for Screening. J. Magn. Reson. Imaging 2019;50:377–390 doi: 10.1002/jmri.26654.

4. Morrow M, Waters J, Morris E. MRI for breast cancer screening, diagnosis, and treatment. The Lancet 2011;378:1804–1811 doi: 10.1016/S0140-6736(11)61350-0.

5. Siu AL, on behalf of the U.S. Preventive Services Task Force. Screening for Breast Cancer: U.S. Preventive Services Task Force Recommendation Statement. Ann. Intern. Med. 2016;164:279 doi: 10.7326/M15-2886.

6. Saslow D, Boetes C, Burke W, et al. American Cancer Society Guidelines for Breast Screening with MRI as an Adjunct to Mammography. CA. Cancer J. Clin. 2007;57:75–89 doi: 10.3322/canjclin.57.2.75.

7. Oeffinger KC, Fontham EH, Etzioni R, et al. Breast cancer screening for women at average risk: 2015 guideline update from the american cancer society. JAMA 2015;314:1599–1614 doi: 10.1001/jama.2015.12783.

8. Rao AA, Feneis J, Lalonde C, Ojeda-Fournier H. A Pictorial Review of Changes in the BI-RADS Fifth Edition. RadioGraphics 2016;36:623–639 doi: 10.1148/rg.2016150178.

9. Idowu MO. Diagnosis and management of breast tumors: a practical handbook and multidisciplinary approach. New York, NY: Springer Science+Business Media; 2017.

10. Das S, Lo AW. Re-inventing drug development: A case study of the I-SPY 2 breast cancer clinical trials program. Contemp. Clin. Trials 2017;62:168–174 doi: 10.1016/j.cct.2017.09.002.

11. Partridge SC, Zhang Z, Newitt DC, et al. Diffusion-weighted MRI Findings Predict Pathologic Response in Neoadjuvant Treatment of Breast Cancer: The ACRIN 6698 Multicenter Trial. Radiology 2018:180273 doi: 10.1148/radiol.2018180273.

12. Partridge SC, Zhang Z, Newitt DC, et al. Diffusion-weighted MRI Findings Predict Pathologic Response in Neoadjuvant Treatment of Breast Cancer: The ACRIN 6698 Multicenter Trial. Radiology 2018;289:618–627 doi: 10.1148/radiol.2018180273.

13. Li W, Newitt DC, Wilmes LJ, et al. Additive value of diffusion-weighted MRI in the I-SPY 2 TRIAL. J. Magn. Reson. Imaging 2019;50:1742–1753 doi: 10.1002/jmri.26770.

14. Kopans DB. The 2009 U.S. Preventive Services Task Force Guidelines Ignore Important Scientific Evidence and Should Be Revised or Withdrawn. Radiology 2010;256:15–20 doi: 10.1148/radiol.10100057.

15. Herman C. Clinical Pearl What Makes a Screening Exam “Good”? Ethics J. Am. Med. Assoc. 2006;8:34–37.

16. Grady D. Call to Increase M.R.I. Use for Breast Exam. N. Y. Times 2007.

17. Houssami N, Hayes DF. Review of Preoperative Magnetic Resonance Imaging (MRI) in Breast Cancer: Should MRI Be Performed on All Women with Newly Diagnosed, Early Stage Breast Cancer? CA. Cancer J. Clin. 2009;59:290–302 doi: 10.3322/caac.20028.

18. Evans A, Vinnicombe S. Overdiagnosis in breast imaging. The Breast 2017;31:270–273 doi: 10.1016/j.breast.2016.10.011.

19. Houssami N, Turner R, Morrow M. Preoperative Magnetic Resonance Imaging in Breast Cancer: Meta-Analysis of Surgical Outcomes. Ann. Surg. 2013;257:249–255 doi: 10.1097/SLA.0b013e31827a8d17.

20. Saadatmand S, Geuzinge HA, Rutgers EJT, et al. MRI versus mammography for breast cancer screening in women with familial risk (FaMRIsc): a multicentre, randomised, controlled trial. Lancet Oncol. 2019;20:1136–1147 doi: 10.1016/S1470-2045(19)30275-X.

21. Hwang ES, Hyslop T, Lynch T, et al. The COMET (Comparison of Operative versus Monitoring and Endocrine Therapy) trial: a phase III randomised controlled clinical trial for low-risk ductal carcinoma in situ (DCIS). BMJ Open 2019;9:e026797 doi: 10.1136/bmjopen-2018-026797.

22. Elshof LE, Tryfonidis K, Slaets L, et al. Feasibility of a prospective, randomised, open-label, international multicentre, phase III, non-inferiority trial to assess the safety of active surveillance for low risk ductal carcinoma in situ – The LORD study. Eur. J. Cancer 2015;51:1497–1510 doi: 10.1016/j.ejca.2015.05.008.

23. Bernstein MA, King KF, Zhou XJ. Handbook of MRI pulse sequences. Amsterdam ; Boston: Academic Press; 2004.

24. Andersson JLR, Skare S, Ashburner J. How to correct susceptibility distortions in spin-echo echo-planar images: application to diffusion tensor imaging. NeuroImage 2003;20:870–888 doi: 10.1016/S1053-8119(03)00336-7.

25. Smith SM, Jenkinson M, Woolrich MW, et al. Advances in functional and structural MR image analysis and implementation as FSL. NeuroImage 2004;23, Supplement 1:S208–S219 doi: 10.1016/j.neuroimage.2004.07.051.

26. TOPUP. FSL. http://fsl.fmrib.ox.ac.uk/fsl/fslwiki/TOPUP.

27. Gomori JM, Holland GA, Grossman RI, Gefter WB, Lenkinski RE. Fat suppression by section-select gradient reversal on spin-echo MR imaging. Work in progress. Radiology 1988;168:493–495 doi: 10.1148/radiology.168.2.3393670.

28. Sodickson DK, Manning WJ. Simultaneous acquisition of spatial harmonics (SMASH): Fast imaging with radiofrequency coil arrays. Magn. Reson. Med. 1997;38:591–603 doi: 10.1002/mrm.1910380414.

29. Pruessmann KP, Weiger M, Scheidegger MB, Boesiger P. SENSE: Sensitivity encoding for fast MRI. Magn. Reson. Med. 1999;42:952–962 doi: 10.1002/(SICI)1522-2594(199911)42:5<952::AID-MRM16>3.0.CO;2-S.

30. Griswold MA, Jakob PM, Heidemann RM, et al. Generalized autocalibrating partially parallel acquisitions (GRAPPA). Magn. Reson. Med. 2002;47:1202–1210 doi: 10.1002/mrm.10171.

31. Nishimura DG. Principles of Magnetic Resonance Imaging. Stanford Univ; 2010.

32. Müller S. Multifrequency selective rf pulses for multislice MR imaging. Magn. Reson. Med. 1988;6:364–371 doi: 10.1002/mrm.1910060315.

33. Larkman DJ, Hajnal JV, Herlihy AH, Coutts GA, Young IR, Ehnholm G. Use of multicoil arrays for separation of signal from multiple slices simultaneously excited. J. Magn. Reson. Imaging 2001;13:313–317.

34. Barth M, Breuer F, Koopmans PJ, Norris DG, Poser BA. Simultaneous multislice (SMS) imaging techniques: SMS Imaging. Magn. Reson. Med. 2016;75:63–81 doi: 10.1002/mrm.25897.

35. Breuer FA, Blaimer M, Heidemann RM, Mueller MF, Griswold MA, Jakob PM. Controlled aliasing in parallel imaging results in higher acceleration (CAIPIRINHA) for multi-slice imaging. Magn. Reson. Med. 2005;53:684–691 doi: 10.1002/mrm.20401.

36. Setsompop K, Gagoski BA, Polimeni JR, Witzel T, Wedeen VJ, Wald LL. Blipped-controlled aliasing in parallel imaging for simultaneous multislice echo planar imaging with reduced g-factor penalty. Magn. Reson. Med. 2012;67:1210–1224 doi: 10.1002/mrm.23097.

37. Reese TG, Heid O, Weisskoff RM, Wedeen VJ. Reduction of eddy-current-induced distortion in diffusion MRI using a twice-refocused spin echo. Magn. Reson. Med. 2003;49:177–182 doi: 10.1002/mrm.10308.

38. Mani M, Jacob M, Kelley D, Magnotta V. Multi-shot sensitivity-encoded diffusion data recovery using structured low-rank matrix completion (MUSSELS): Annihilating

Filter K-Space Formulation for Multi-Shot DWI Recovery. Magn. Reson. Med. 2017;78:494–507 doi: 10.1002/mrm.26382.

39. Chen N, Guidon A, Chang H-C, Song AW. A robust multi-shot scan strategy for high-resolution diffusion weighted MRI enabled by multiplexed sensitivity-encoding (MUSE). NeuroImage 2013;72:41–47 doi: 10.1016/j.neuroimage.2013.01.038.

40. Lee J, Jin KH, Ye JC. Reference-free single-pass EPI Nyquist ghost correction using annihilating filter-based low rank Hankel matrix (ALOHA): Reference-Free Single-Pass EPI Nyquist Ghost Correction using ALOHA. Magn. Reson. Med. 2016:n/a-n/a doi: 10.1002/mrm.26077.

41. Lustig M, Pauly JM. SPIRiT: Iterative self-consistent parallel imaging reconstruction from arbitrary k-space. Magn. Reson. Med. 2010:n/a-n/a doi: 10.1002/mrm.22428.

42. Uecker M, Lai P, Murphy MJ, et al. ESPIRiT-an eigenvalue approach to autocalibrating parallel MRI: Where SENSE meets GRAPPA. Magn. Reson. Med. 2014;71:990–1001 doi: 10.1002/mrm.24751.

43. Hu Y. Multi-shot DWI with multiplexed sensitivity encoding (MUSE) versus single-shot DWI in the breast. https://index.mirasmart.com/ISMRM2019/PDFfiles/0604.html. Accessed February 6, 2020.

44. Hu Y, Levine EG, Tian Q, et al. Motion-robust reconstruction of multishot diffusion-weighted images without phase estimation through locally low-rank regularization. Magn. Reson. Med. 2019;81:1181–1190 doi: 10.1002/mrm.27488.

45. Porter DA, Heidemann RM. High resolution diffusion-weighted imaging using readout-segmented echo-planar imaging, parallel imaging and a two-dimensional navigator-based reacquisition. Magn. Reson. Med. 2009;62:468–475 doi: 10.1002/mrm.22024.

46. Wu W, Miller KL. Image formation in diffusion MRI: A review of recent technical developments: Review of Image Formation in dMRI. J. Magn. Reson. Imaging 2017;46:646–662 doi: 10.1002/jmri.25664.

47. Bogner W, Pinker-Domenig K, Bickel H, et al. Readout-segmented echo-planar imaging improves the diagnostic performance of diffusion-weighted MR breast examinations at 3.0 T. Radiology 2012;263:64–76.

48. Wisner DJ, Rogers N, Deshpande VS, et al. High-resolution diffusion-weighted imaging for the separation of benign from malignant BI-RADS 4/5 lesions found on breast MRI at 3T. J. Magn. Reson. Imaging 2014;40:674–681 doi: 10.1002/jmri.24416.

49. Kim YJ, Kim SH, Kang BJ, et al. Readout-Segmented Echo-Planar Imaging in Diffusion-Weighted MR Imaging in Breast Cancer: Comparison with Single-Shot Echo-

Planar Imaging in Image Quality. Korean J. Radiol. 2014;15:403 doi: 10.3348/kjr.2014.15.4.403.

50. Kanao S, Kataoka M, Iima M, et al. High-resolution diffusion-weighted MRI of the breast using readout-segmented EPI and single-shot EPI. Imaging Med 2017;9:185–190.

51. Baltzer PAT, Bickel H, Spick C, et al. Potential of Noncontrast Magnetic Resonance Imaging With Diffusion-Weighted Imaging in Characterization of Breast Lesions: Intraindividual Comparison With Dynamic Contrast-Enhanced Magnetic Resonance Imaging. Invest. Radiol. 2018;53:229–235 doi: 10.1097/RLI.0000000000000433.

52. Wilmes LJ, McLaughlin RL, Newitt DC, et al. High-Resolution Diffusion-Weighted Imaging for Monitoring Breast Cancer Treatment Response. Acad. Radiol. 2013;20:581–589 doi: 10.1016/j.acra.2013.01.009.

53. Singer L, Wilmes LJ, Saritas EU, et al. High-resolution Diffusion-weighted Magnetic Resonance Imaging in Patients with Locally Advanced Breast Cancer. Acad. Radiol. 2012;19:526–534 doi: 10.1016/j.acra.2011.11.003.

54. Barentsz MW, Taviani V, Chang JM, et al. Assessment of tumor morphology on diffusion-weighted (DWI) breast MRI: Diagnostic value of reduced field of view DWI: Diagnostic Value of Reduced-FOV DWI. J. Magn. Reson. Imaging 2015;42:1656–1665 doi: 10.1002/jmri.24929.

55. Feinberg DA, Oshio K. GRASE (gradient-and spin-echo) MR imaging: a new fast clinical imaging technique. Radiology 1991;181:597–602.

56. Pipe JG. Motion correction with PROPELLER MRI: Application to head motion and free-breathing cardiac imaging. Magn. Reson. Med. 1999:963–969.

57. McNab JA, Miller KL. Steady-state diffusion-weighted imaging: theory, acquisition and analysis. NMR Biomed. 2010;23:781–793 doi: 10.1002/nbm.1509.

58. Granlund KL, Staroswiecki E, Alley MT, Daniel BL, Hargreaves BA. High-resolution, three-dimensional diffusion-weighted breast imaging using DESS. Magn. Reson. Imaging 2014;32:330–341 doi: 10.1016/j.mri.2013.12.014.

59. Solomon E, Shemesh N, Frydman L. Diffusion weighted MRI by spatiotemporal encoding: Analytical description and in vivo validations. J. Magn. Reson. 2013;232:76–86 doi: 10.1016/j.jmr.2013.02.014.

60. Solomon E, Nissan N, Furman-Haran E, et al. Overcoming limitations in diffusion-weighted MRI of breast by spatio-temporal encoding. Magn. Reson. Med. 2015;73:2163–2173 doi: 10.1002/mrm.25344.

61. Le Bihan D, Breton E, Lallemand D, Grenier P, Cabanis E, Laval-Jeantet M. MR imaging of intravoxel incoherent motions: application to diffusion and perfusion in neurologic disorders. Radiology 1986;161:401–407.

62. Stejskal EO, Tanner JE. Spin Diffusion Measurements: Spin Echoes in the Presence of a Time-Dependent Field Gradient. J. Chem. Phys. 1965;42:288–292 doi: 10.1063/1.1695690.

63. Partridge SC, Mcdonald ES. Diffusion Weighted Magnetic Resonance Imaging of the Breast:Protocol Optimization, Interpretation, and Clinical Applications: Protocol Optimization, Interpretation, and Clinical Applications. Magn. Reson. Imaging Clin. N. Am. 2013;21:601–624 doi: 10.1016/j.mric.2013.04.007.

64. Basser PJ, Mattiello J, LeBihan D. MR diffusion tensor spectroscopy and imaging. Biophys. J. 1994;66:259–267 doi: 10.1016/S0006-3495(94)80775-1.

65. Basser PJ. Inferring microstructural features and the physiological state of tissues from diffusion-weighted images. NMR Biomed. 1995;8:333–344 doi: 10.1002/nbm.1940080707.

66. Lerner A, Mogensen MA, Kim PE, Shiroishi MS, Hwang DH, Law M. Clinical Applications of Diffusion Tensor Imaging. World Neurosurg. 2014;82:96–109 doi: 10.1016/j.wneu.2013.07.083.

67. Iima M, Honda M, Sigmund EE, Ohno Kishimoto A, Kataoka M, Togashi K. Diffusion MRI of the breast: Current status and future directions. J. Magn. Reson. Imaging 2019 doi: 10.1002/jmri.26908.

68. Partridge SC, Ziadloo A, Murthy R, et al. Diffusion tensor MRI: Preliminary anisotropy measures and mapping of breast tumors. J. Magn. Reson. Imaging 2010;31:339–347 doi: 10.1002/jmri.22045.

69. Furman-Haran E, Grobgeld D, Nissan N, Shapiro-Feinberg M, Degani H. Can diffusion tensor anisotropy indices assist in breast cancer detection? J. Magn. Reson. Imaging 2016:n/a-n/a doi: 10.1002/jmri.25292.

70. Le Bihan D. Apparent Diffusion Coefficient and Beyond: What Diffusion MR Imaging Can Tell Us about Tissue Structure. Radiology 2013;268:318–322 doi: 10.1148/radiol.13130420.

71. Jensen JH, Helpern JA, Ramani A, Lu H, Kaczynski K. Diffusional kurtosis imaging: the quantification of non-gaussian water diffusion by means of magnetic resonance imaging. Magn. Reson. Med. 2005;53:1432–1440 doi: 10.1002/mrm.20508.

72. Jensen JH, Helpern JA. MRI quantification of non-Gaussian water diffusion by kurtosis analysis. NMR Biomed. 2010;23:698–710 doi: 10.1002/nbm.1518.

73. Le Bihan D, Breton E, Lallemand D, Aubin ML, Vignaud J, Laval-Jeantet M. Separation of diffusion and perfusion in intravoxel incoherent motion MR imaging. Radiology 1988;168:497–505.

74. Le Bihan D. What can we see with IVIM MRI? NeuroImage 2019;187:56–67 doi: 10.1016/j.neuroimage.2017.12.062.

75. Guo Y, Cai Y-Q, Cai Z-L, et al. Differentiation of clinically benign and malignant breast lesions using diffusion-weighted imaging. J. Magn. Reson. Imaging 2002;16:172–178 doi: 10.1002/jmri.10140.

76. Chen X, Li W, Zhang Y, Wu Q, Guo Y, Bai Z. Meta-analysis of quantitative diffusion-weighted MR imaging in the differential diagnosis of breast lesions. BMC Cancer 2010;10:693 doi: 10.1186/1471-2407-10-693.

77. EI Khouli RH, Jacobs MA, Mezban SD, et al. Diffusion-weighted Imaging Improves the Diagnostic Accuracy of Conventional 3.0-T Breast MR Imaging 1. Radiology 2010;256:64–73.

78. Partridge SC, Nissan N, Rahbar H, Kitsch AE, Sigmund EE. Diffusion-weighted breast MRI: Clinical applications and emerging techniques: Diffusion-Weighted Breast MRI. J. Magn. Reson. Imaging 2017;45:337–355 doi: 10.1002/jmri.25479.

79. Zhang L, Tang M, Min Z, Lu J, Lei X, Zhang X. Accuracy of Combined Dynamic Contrast-Enhanced Magnetic Resonance Imaging and Diffusion-Weighted Imaging for Breast Cancer Detection: A Meta-Analysis. Acta Radiol. 2016;57:651–660 doi: 10.1177/0284185115597265.

80. Rahbar H, Zhang Z, Chenevert TL, et al. Utility of Diffusion-weighted Imaging to Decrease Unnecessary Biopsies Prompted by Breast MRI: A Trial of the ECOG-ACRIN Cancer Research Group (A6702). Clin. Cancer Res. 2019;25:1756–1765 doi: 10.1158/1078-0432.CCR-18-2967.

81. Avendano D, Marino MA, Leithner D, et al. Limited role of DWI with apparent diffusion coefficient mapping in breast lesions presenting as non-mass enhancement on dynamic contrast-enhanced MRI. Breast Cancer Res. 2019;21:136 doi: 10.1186/s13058-019-1208-y.

82. Choi SY, Chang Y-W, Park HJ, Kim HJ, Hong SS, Seo DY. Correlation of the apparent diffusion coefficiency values on diffusion-weighted imaging with prognostic factors for breast cancer. Br. J. Radiol. 2012;85:e474–e479 doi: 10.1259/bjr/79381464.

83. Mori N, Ota H, Mugikura S, et al. Luminal-Type Breast Cancer: Correlation of Apparent Diffusion Coefficients with the Ki-67 Labeling Index. Radiology 2015;274:66–73 doi: 10.1148/radiol.14140283.

84. Kitajima K, Yamano T, Fukushima K, et al. Correlation of the SUVmax of FDG-PET and ADC values of diffusion-weighted MR imaging with pathologic prognostic factors in breast carcinoma. Eur. J. Radiol. 2016;85:943–949 doi: 10.1016/j.ejrad.2016.02.015.

85. Kim EJ, Kim SH, Park GE, et al. Histogram analysis of apparent diffusion coefficient at 3.0t: Correlation with prognostic factors and subtypes of invasive ductal carcinoma: Histogram Analysis of ADC Values in IDC. J. Magn. Reson. Imaging 2015;42:1666–1678 doi: 10.1002/jmri.24934.

86. Rahbar H, Partridge SC, Eby PR, et al. Characterization of ductal carcinoma in situ on diffusion weighted breast MRI. Eur. Radiol. 2011;21:2011–2019 doi: 10.1007/s00330-011-2140-4.

87. Xing H, Song C, Li W. Meta analysis of lymph node metastasis of breast cancer patients: Clinical value of DWI and ADC value. Eur. J. Radiol. 2016;85:1132–1137 doi: 10.1016/j.ejrad.2016.03.019.

88. Cortazar P, Zhang L, Untch M, et al. Pathological complete response and long-term clinical benefit in breast cancer: the CTNeoBC pooled analysis. The Lancet 2014;384:164–172 doi: 10.1016/S0140-6736(13)62422-8.

89. Malyarenko DI, Ross BD, Chenevert TL. Analysis and correction of gradient nonlinearity bias in apparent diffusion coefficient measurements: ADC Spatial Bias Correction. Magn. Reson. Med. 2014;71:1312–1323 doi: 10.1002/mrm.24773.

90. On behalf of the EUSOBI international Breast Diffusion-Weighted Imaging working group, Baltzer P, Mann RM, et al. Diffusion-weighted imaging of the breast—a consensus and mission statement from the EUSOBI International Breast Diffusion-Weighted Imaging working group. Eur. Radiol. 2020;30:1436–1450 doi: 10.1007/s00330-019-06510-3.

91. Chenevert TL, Galbán CJ, Ivancevic MK, et al. Diffusion coefficient measurement using a temperature-controlled fluid for quality control in multicenter studies. J. Magn. Reson. Imaging JMRI 2011;34:983–987 doi: 10.1002/jmri.22363.

92. Chen N, Wyrwicz AM. Removal of EPI Nyquist ghost artifacts with two-dimensional phase correction. Magn. Reson. Med. 2004;51:1247–1253.

93. Zur Y. Method and apparatus of MR imaging with two dimensional phase and magnitude correction. Google Patents; 2010.

94. Xu D, King KF, Zur Y, Hinks RS. Robust 2D phase correction for echo planar imaging under a tight field-of-view. Magn. Reson. Med. 2010;64:1800–1813 doi: 10.1002/mrm.22577.

95. Xiang Q-S, Ye FQ. Correction for geometric distortion and N/2 ghosting in EPI by phase labeling for additional coordinate encoding (PLACE). Magn. Reson. Med. 2007;57:731–741 doi: 10.1002/mrm.21187.

96. Kellman P, McVeigh ER. Phased array ghost elimination. NMR Biomed. 2006;19:352–361 doi: 10.1002/nbm.1044.

97. Kim Y-C, Nielsen J-F, Nayak KS. Automatic correction of echo-planar imaging (EPI) ghosting artifacts in real-time interactive cardiac MRI using sensitivity encoding. J. Magn. Reson. Imaging 2008;27:239–245 doi: 10.1002/jmri.21214.

98. Hoge WS, Tan H, Kraft RA. Robust EPI Nyquist ghost elimination via spatial and temporal encoding. Magn. Reson. Med. 2010;64:1781–1791 doi: 10.1002/mrm.22564.

99. Hoge WS, Polimeni JR. Dual-polarity GRAPPA for simultaneous reconstruction and ghost correction of echo planar imaging data: Dual-Polarity GRAPPA for EPI. Magn. Reson. Med. 2016;76:32–44 doi: 10.1002/mrm.25839.

100. Skare S, Clayton DB, Newbould R, Moseley M, Bammer R. A fast and robust minimum entropy based non-interactive Nyquist ghost correction algorithm. In: Proc. Intl. Soc. Mag. Reson. Med. Vol. 14. Seattle, Washington; 2006. p. 2349.

101. Clare S. Iterative Nyquist ghost correction for single and multi-shot EPI using an entropy measure. In: Proceedings of the 16th annual meeting of ISMRM, Toronto, Canada. ; 2003. p. 1041.

102. Peterson E, Aksoy M, Maclaren J, Bammer R. Acquisition-free Nyquist ghost correction for parallel imaging accelerated EPI. In: Proc. Intl. Soc. Mag. Reson. Med. Vol. 23. Toronto, Ontario; 2015. p. 0075.

103. Foxall DL, Harvey PR, Huang J. Rapid iterative reconstruction for echo planar imaging. Magn. Reson. Med. 1999;42:541–547 doi: 10.1002/(SICI)1522-2594(199909)42:3<541::AID-MRM16>3.0.CO;2-F.

104. Moeller S, Yacoub E, Olman CA, et al. Multiband multislice GE-EPI at 7 tesla, with 16-fold acceleration using partial parallel imaging with application to high spatial and temporal whole-brain fMRI. Magn. Reson. Med. 2010;63:1144–1153 doi: 10.1002/mrm.22361.

105. Feinberg DA, Moeller S, Smith SM, et al. Multiplexed Echo Planar Imaging for Sub-Second Whole Brain FMRI and Fast Diffusion Imaging Valdes-Sosa PA, editor. PLoS ONE 2010;5:e15710 doi: 10.1371/journal.pone.0015710.

106. McKay JA, Moeller S, Zhang L, Auerbach EJ, Nelson MT, Bolan PJ. Nyquist ghost correction of breast diffusion weighted imaging using referenceless methods. Magn. Reson. Med. 2018 doi: 10.1002/mrm.27563.

107. McKay JA, Bolan PJ. System and Method for Nyquist Ghost Correction in Medical Imaging.

108. McKay J, Moeller S, Ramanna S, et al. Novel Image-based Nyquist Ghost Correction of Diffusion-Weighted Echo Planar Imaging using Ghost/Object Minimization. In: Paris, France; 2018. p. 5339.

109. McKay JA, Moeller S, Zhang L, Auerbach EJ, Nelson MT, Bolan PJ. Comparison of Referenceless Methods for EPI Ghost Correction in Breast Diffusion Weighted Imaging. In: Intl. Soc. Mag. Reson. Med. Paris, France; 2018. p. 4618.

110. McKay JA, Moeller S, Ramanna S, et al. Nyquist Ghost Correction of High-Resolution SMS Breast DWI with Ghost/Object Minimization. In: Proc. Intl. Soc. Mag. Reson. Med. Vol. 27. Montreal, Quebec; 2019. p. 3354.

111. McKay JA, Church AL, Rubin N, et al. A Reader Study Comparing the Quality of High-Resolution Diffusion Weighted Imaging Methods for Breast MRI. In: Intl. Soc. Mag. Reson. Med. ; 2020. p. 3199.

112. Maier JK, Vavrek RM, Glover GH. Correction of nmr data acquired by an echo-planar technique. Google Patents; 1992.

113. Zhang Y, Wehrli FW. Reference-scan-free method for automated correction of nyquist ghost artifacts in echoplanar brain images. Magn. Reson. Med. 2004;51:621–624 doi: 10.1002/mrm.10724.

114. Hu X, Le TH. Artifact reduction in EPI with phase-encoded reference scan. Magn. Reson. Med. Off. J. Soc. Magn. Reson. Med. Soc. Magn. Reson. Med. 1996;36:166–171.

115. Buonocore MH, Gao L. Ghost Artifact Reduction for Echo Planar Imaging Using Image Phase Correction. Magn. Reson. Med. 1997;38:89–100.

116. Chen Z, Hey S, Geerts-Ossevoort L, Koonen JJ, Van Den Brink JS. Magnetic resonance imaging system with ghost artifact reduction and method operation thereof. Google Patents; 2016.

117. Lee KJ, Barber DC, Paley MN, Wilkinson ID, Papadakis NG, Griffiths PD. Image-based EPI ghost correction using an algorithm based on projection onto convex sets (POCS). Magn. Reson. Med. 2002;47:812–817 doi: 10.1002/mrm.10101.

118. Heid O. Method for the phase correction of nuclear magnetic resonance signals. 2000.

119. Jain AK. Fundamentals of digital image processing. Englewood Cliffs, NJ: Prentice Hall; 1989.

120. NEMA Standards Publication MS 1-2008 (R2014). National Electrical Manufacturers Association; 2014.

121. Hylton N, Partridge SC. ACRIN 6698 Diffusion Weighted MR Imaging Biomarkers for Assessment of Breast Cancer Response to Neoadjuvant Treatment: A sub-study of the I-SPY 2 TRIAL. Am. Coll. Radiol. Imaging Netw. 2012.

122. Sotiropoulos SN, Jbabdi S, Xu J, et al. Advances in diffusion MRI acquisition and processing in the Human Connectome Project. NeuroImage 2013;80:125–143 doi: 10.1016/j.neuroimage.2013.05.057.

123. Hirano M, Satake H, Ishigaki S, Ikeda M, Kawai H, Naganawa S. Diffusion-Weighted Imaging of Breast Masses: Comparison of Diagnostic Performance Using Various Apparent Diffusion Coefficient Parameters. Am. J. Roentgenol. 2012;198:717–722 doi: 10.2214/AJR.11.7093.

124. Kang BJ, Lipson JA, Planey KR, et al. Rim sign in breast lesions on diffusion-weighted magnetic resonance imaging: Diagnostic accuracy and clinical usefulness: Rim Sign in Breast Lesions on DWI. J. Magn. Reson. Imaging 2015;41:616–623 doi: 10.1002/jmri.24617.

125. Taviani V, Alley MT, Banerjee S, et al. High-resolution diffusion-weighted imaging of the breast with multiband 2D radiofrequency pulses and a generalized parallel imaging reconstruction: Breast DWI with Multiband FC2DRF Pulses and Parallel Imaging. Magn. Reson. Med. 2017;77:209–220 doi: 10.1002/mrm.26110.

126. Bolan PJ, Moeller S, Metzger GJ, et al. Breast Diffusion Weighted Imaging with Reduced Artifacts using Multi-band Spin Echo EPI. In: Proc. Intl. Soc. Mag. Reson. Med. Vol. 23. Toronto, Ontario; 2015. p. 0884.

127. McKay JA, Moeller S, Ramanna S, et al. Comparison of methods for high spatial-resolution breast diffusion imaging. In: Proc. Intl. Soc. Mag. Reson. Med. Vol. 25. Honolulu, HI; 2017. p. 2115.

128. Keenan KE, Wilmes LJ, Aliu SO, et al. Design of a breast phantom for quantitative MRI: Design of a Breast Phantom. J. Magn. Reson. Imaging 2016;44:610–619 doi: 10.1002/jmri.25214.

129. Van Essen DC, Smith SM, Barch DM, Behrens TEJ, Yacoub E, Ugurbil K. The WU-Minn Human Connectome Project: An overview. NeuroImage 2013;80:62–79 doi: 10.1016/j.neuroimage.2013.05.041.

130. Andersson JLR, Skare S, Ashburner J. How to correct susceptibility distortions in spin-echo echo-planar images: application to diffusion tensor imaging. NeuroImage 2003;20:870–888 doi: 10.1016/S1053-8119(03)00336-7.

131. Filli L, Ghafoor S, Kenkel D, et al. Simultaneous multi-slice readout-segmented echo planar imaging for accelerated diffusion-weighted imaging of the breast. Eur. J. Radiol. 2016;85:274–278 doi: 10.1016/j.ejrad.2015.10.009.

132. Le Bihan D. Diffusion and perfusion magnetic resonance imaging: applications to functional MRI. New York, NY: Raven Press; 1995.

133. Lee J, Han Y, Ryu J-K, Park J-Y, Ye JC. k-Space Deep Learning for Reference-free EPI Ghost Correction. ArXiv180600153 Cs Eess Stat 2019.

134. Schülke C, Sommer K, Börnert P. EPI artifacts reduction using deep learning. :3.

135. Partridge SC, Nissan N, Rahbar H, Kitsch AE, Sigmund EE. Diffusion-weighted breast MRI: Clinical applications and emerging techniques. J. Magn. Reson. Imaging 2017;45:337–355 doi: 10.1002/jmri.25479.

136. Wilmes LJ, McLaughlin RL, Newitt DC, et al. High-Resolution Diffusion-Weighted Imaging for Monitoring Breast Cancer Treatment Response. Acad. Radiol. 2013;20:581–589 doi: 10.1016/j.acra.2013.01.009.

137. Granlund KL, Staroswiecki E, Alley MT, Daniel BL, Hargreaves BA. High-resolution, three-dimensional diffusion-weighted breast imaging using DESS. Magn. Reson. Imaging 2014;32:330–341 doi: 10.1016/j.mri.2013.12.014.

138. Bogner W, Pinker-Domenig K, Bickel H, et al. Readout-segmented Echo-planar Imaging Improves the Diagnostic Performance of Diffusion-weighted MR Breast Examinations at 3.0 T. Radiology 2012;263:64–76 doi: 10.1148/radiol.12111494.

139. Taviani V, Alley MT, Banerjee S, et al. High-resolution diffusion-weighted imaging of the breast with multiband 2D radiofrequency pulses and a generalized parallel imaging reconstruction. Magn. Reson. Med. 2017;77:209–220 doi: 10.1002/mrm.26110.

140. McKay JA, Ramanna S, Moeller S, et al. Comparison of methods for high spatial-resolution breast diffusion imaging. In: Proceedings 25th Scientific Meeting, ISMRM. Vol. 25. ; 2017. p. 2115.

141. Schweitzer ME. Guidelines for qualitative/subjective research image assessments. J. Magn. Reson. Imaging JMRI 2018;48:11–12 doi: 10.1002/jmri.26205.

142. Crete-Roffet F, Dolmiere T, Ladret P, Nicolas M. The blur effect: perception and estimation with a new no-reference perceptual blur metric. In: San Jose, CA, USA; 2007. p. 64920I. doi: 10.1117/12.702790.